Comparative study of polymorph nanosheet materials for emerging metal-ion batteries

by

Davi Marcelo Soares

B.S., Universidade Federal de Itajubá, Brazil, 2015

M.S., Universidade Estadual de Campinas, Brazil, 2018

AN ABSTRACT OF A DISSERTATION

submitted in partial fulfillment of the
requirements for the degree

DOCTOR OF PHILOSOPHY

Alan Levin Department of Mechanical and Nuclear Engineering
Carl R. Ice College of Engineering

KANSAS STATE UNIVERSITY
Manhattan, Kansas

2021

Abstract

Rechargeable batteries have attained strategic place in applications involving transportation, microelectronics, and electric power grid in the past 30 years. Yet in a society that strives to achieve both sustainability and economic growth the concern whether lithium and cobalt reserves may supply the future demand of multibillion-dollar industries and emerging markets has risen. To address this concern, research on novel rechargeable batteries composed by earth-abundant elements has re-gained traction recently. As potential candidates for beyond lithium-ion battery (LIB) technologies, both sodium and potassium present low cost, reserves more globally distributed, and redox potentials closer to that of lithium metal. Likewise, from the knowledge consolidated over decades on LIBs, certain lessons learnt can be applied in the study of these emerging alkali metal ion batteries. One of these lessons is that to enable the use of sodium- and potassium-ion battery technologies a comprehensive study of crystal structure and electrochemical processes happening in electrode materials is crucial. In this scenario, a class of materials known as transition metal dichalcogenides (TMDs), whose structure was first determined by Linus Pauling in 1923, has re-gained attention due to layered and wide variety of species and chemistries. To date, approximately 60 species of TMDs are known, in which two thirds present layered structure and polymorphism.

Conducted in the 1970s by the 2019 Nobel Prize in Chemistry, M. Stanley Whittingham, research on layered TMDs for electrochemical energy storage applications was shortly abandoned owing to poor stability of TMDs. Upon the increasing interest on layered materials in the 2000s, TMD nanosheets were found to have relatively higher uptake and faster diffusion of Li^+, Na^+, and K^+ in their host structure – leading to high theoretical capacity and rate capability, respectively. Nevertheless, along with the fascinating properties of TMDs – some yet to be unveiled – research challenges are also still present.

Molybdenum disulfide (MoS_2) is a layered TMD that presents polymorphism, high specific capacity towards sodium-ions and abundant availability on earth. However, MoS_2 as sodium-ion battery (SIB) electrode shows poor cycle stability and fast capacity degradation, due to low electronic conductivity, and low reversibility. To address the stability issue of MoS_2, this thesis explored synthesis of a novel composite material of 2H-MoS_2 functionalized with a thin layer of molecular precursor-derived silicon oxycarbide (SiOC) ceramic as electrode for sodium-ion battery (SIB). The functionalized MoS_2 electrode was able to overcome shortcomings of pristine 2H-MoS_2 electrodes in SIB. The improved stability was attributed to the SiOC, a ceramic material that safeguarded the active material (MoS_2) without compromising sodiation and de-sodiation processes. Moreover, SiOC provided free carbon domains that showed increased electronic conductivity of functionalized MoS_2, as evidenced by the rate capability test. Electrochemical results show that specific capacity of MoS_2-SiOC was 12 times higher than pristine MoS_2 at $200\,\mathrm{mA\,g^{-1}}$.

Later, in view of the larger interlayer spacing and unique electronic properties of some layered telluride-based TMDs, tungsten ditelluride (WTe_2) was selected as host material for studies involving potassium-ion storage. In addition to providing a detailed description of crystal phase of the thermodynamically stable Td phase of WTe_2 at room temperature, this thesis introduces a discussion regarding electrochemical impedance spectroscopy (EIS), a frequency domain analysis that can provide useful information for electrochemical systems. Findings shows that due to higher interlayer spacing and conversion type-reactions – confirmed by ex-situ post-cycling analysis – Td-WTe_2 showed first cycle specific charge capacity of 3.3 K^+ stored per WTe_2 molecule, stable capacity of $143\,\mathrm{mA\,h\,g^{-1}}$ at 10^{th} cycle number – outperforming WS_2 and graphite – reasonable cycling stability, and low charge transfer resistance. This is the first known work in the field to highlight the potential of Td-WTe_2 as potassium-ion battery (KIB) electrode.

Td-WTe_2 was also employed as electrode material in a study of diffusivity of Na^+ and K^+ in SIB and KIB half-cells, respectively. Although in the literature there are reports that suggest the larger ionic radius of K^+ (1.33 Å) – in comparison to Na^+ (0.97 Å) – lead to an inferior electrochemical performance of KIBs, in this work we demonstrated that KIB

outperforms the SIB cell in terms of rate capability and cycling stability. This behavior was explained by Stokes' radius concept of Na^+ and K^+ in propylene carbonate (PC) based electrolyte, which explains the higher mobility of K^+ in the electrolyte medium. These findings corroborate the potential of semimetal TMD electrode materials and highlight how electrolyte medium has implications on electrochemical performance of electrode materials.

In summary, the scientific contributions attained in this research work intend to support the current development and understanding of novel sulfide- and telluride-layered TMDs materials for sodium- and potassium-ion batteries, respectively.

Comparative study of polymorph nanosheet materials for emerging metal-ion batteries

by

Davi Marcelo Soares

B.S., Universidade Federal de Itajubá, Brazil, 2015

M.S., Universidade Estadual de Campinas, Brazil, 2018

A DISSERTATION

submitted in partial fulfillment of the
requirements for the degree

DOCTOR OF PHILOSOPHY

Alan Levin Department of Mechanical and Nuclear Engineering
Carl R. Ice College of Engineering

KANSAS STATE UNIVERSITY
Manhattan, Kansas

2021

Approved by:

Major Professor
Dr. Gurpreet Singh

Copyright

Abstract

Rechargeable batteries have attained strategic place in applications involving transportation, microelectronics, and electric power grid in the past 30 years. Yet in a society that strives to achieve both sustainability and economic growth the concern whether lithium and cobalt reserves may supply the future demand of multibillion-dollar industries and emerging markets has risen. To address this concern, research on novel rechargeable batteries composed by earth-abundant elements has re-gained traction recently. As potential candidates for beyond lithium-ion battery (LIB) technologies, both sodium and potassium present low cost, reserves more globally distributed, and redox potentials closer to that of lithium metal. Likewise, from the knowledge consolidated over decades on LIBs, certain lessons learnt can be applied in the study of these emerging alkali metal ion batteries. One of these lessons is that to enable the use of sodium- and potassium-ion battery technologies a comprehensive study of crystal structure and electrochemical processes happening in electrode materials is crucial. In this scenario, a class of materials known as transition metal dichalcogenides (TMDs), whose structure was first determined by Linus Pauling in 1923, has re-gained attention due to layered and wide variety of species and chemistries. To date, approximately 60 species of TMDs are known, in which two thirds present layered structure and polymorphism.

Conducted in the 1970s by the 2019 Nobel Prize in Chemistry, M. Stanley Whittingham, research on layered TMDs for electrochemical energy storage applications was shortly abandoned owing to poor stability of TMDs. Upon the increasing interest on layered materials in the 2000s, TMD nanosheets were found to have relatively higher uptake and faster diffusion of Li^+, Na^+, and K^+ in their host structure – leading to high theoretical capacity and rate capability, respectively. Nevertheless, along with the fascinating properties of TMDs – some yet to be unveiled – research challenges are also still present.

Molybdenum disulfide (MoS_2) is a layered TMD that presents polymorphism, high specific capacity towards sodium-ions and abundant availability on earth. However, MoS_2 as sodium-ion battery (SIB) electrode shows poor cycle stability and fast capacity degradation, due to low electronic conductivity, and low reversibility. To address the stability issue of MoS_2, this thesis explored synthesis of a novel composite material of 2H-MoS_2 functionalized with a thin layer of molecular precursor-derived silicon oxycarbide (SiOC) ceramic as electrode for sodium-ion battery (SIB). The functionalized MoS_2 electrode was able to overcome shortcomings of pristine 2H-MoS_2 electrodes in SIB. The improved stability was attributed to the SiOC, a ceramic material that safeguarded the active material (MoS_2) without compromising sodiation and de-sodiation processes. Moreover, SiOC provided free carbon domains that showed increased electronic conductivity of functionalized MoS_2, as evidenced by the rate capability test. Electrochemical results show that specific capacity of MoS_2-SiOC was 12 times higher than pristine MoS_2 at $200\,\mathrm{mA\,g^{-1}}$.

Later, in view of the larger interlayer spacing and unique electronic properties of some layered telluride-based TMDs, tungsten ditelluride (WTe_2) was selected as host material for studies involving potassium-ion storage. In addition to providing a detailed description of crystal phase of the thermodynamically stable Td phase of WTe_2 at room temperature, this thesis introduces a discussion regarding electrochemical impedance spectroscopy (EIS), a frequency domain analysis that can provide useful information for electrochemical systems. Findings shows that due to higher interlayer spacing and conversion type-reactions – confirmed by ex-situ post-cycling analysis – Td-WTe_2 showed first cycle specific charge capacity of 3.3 K^+ stored per WTe_2 molecule, stable capacity of $143\,\mathrm{mA\,h\,g^{-1}}$ at 10^{th} cycle number – outperforming WS_2 and graphite – reasonable cycling stability, and low charge transfer resistance. This is the first known work in the field to highlight the potential of Td-WTe_2 as potassium-ion battery (KIB) electrode.

Td-WTe_2 was also employed as electrode material in a study of diffusivity of Na^+ and K^+ in SIB and KIB half-cells, respectively. Although in the literature there are reports that suggest the larger ionic radius of K^+ (1.33 Å) – in comparison to Na^+ (0.97 Å) – lead to an inferior electrochemical performance of KIBs, in this work we demonstrated that KIB

outperforms the SIB cell in terms of rate capability and cycling stability. This behavior was explained by Stokes' radius concept of Na^+ and K^+ in propylene carbonate (PC) based electrolyte, which explains the higher mobility of K^+ in the electrolyte medium. These findings corroborate the potential of semimetal TMD electrode materials and highlight how electrolyte medium has implications on electrochemical performance of electrode materials.

In summary, the scientific contributions attained in this research work intend to support the current development and understanding of novel sulfide- and telluride-layered TMDs materials for sodium- and potassium-ion batteries, respectively.

Table of Contents

List of Figures

List of Tables

List of Abbreviations

AM additive manufacturing.

BEV battery electric vehicle.

BEVs battery electric vehicles.

CE Coulombic efficiency.

CEs Coulombic efficiencies.

CNFs carbon nanofibers.

CNTs carbon nano tubes.

CPE constant phase element.

CV cyclic voltammetry.

CVD chemical vapor deposition.

DEC diethyl carbonate.

DFT density-functional theory.

DIW direct ink writing.

DMC dimethyl carbonate.

DME dimethoxyethane.

EC ethylene carbonate.

EDX energy dispersive X-ray.

EES electrochemical energy storage.

EIS electrochemical impedance spectroscopy.

EMC ethyl methyl carbonate.

ESS energy storage systems.

FEC fluoroethylene carbonate.

GCD galvanostatic charge-discharge.

GITT galvanostatic intermittent titration technique.

GO graphene oxide.

HAADF High-angle annular dark-field imaging.

HRTEM high-resolution transmission electron microscopy.

ICE internal combustion engine.

KFSI bis(fluoro-slufonyl)imide.

KIB potassium-ion battery.

KIBs potassium-ion batteries.

LIB lithium-ion battery.

LIBs lithium-ion batteries.

LST generalized linear system theory.

NEMS nano-electrochemical systems.

NMP 1-methyl-2-pyrrolidone.

OCP open circuit potential.

PC propylene carbonate.

PDC polymer derived ceramic.

PDCs Polymer derived ceramics.

PEO poly-ethylene oxide.

PVA polyvinyl alcohol.

PVD physical vapor deposition.

rGO reduced graphene oxide.

SAED selected area electron diffraction.

SEI solid electrolyte interphase.

SEM scanning electron microscopy.

SHE standard hydrogen electrode.

SIB sodium-ion battery.

SIBs sodium-ion batteries.

STEM scanning transmission electron microscopy.

TEM transmission electron microscopy.

TMD transition metal dichalcogenide.

TMDs transition metal dichalcogenides.

XPS X-ray photoelectron spectroscopy.

XRD X-ray diffraction.

Acknowledgments

Firstly, I would like to thank my advisor, Dr. Gurpreet Singh, for the suggestions and guidance that helped me improve the quality of my work. I am grateful for his mentorship and inspiration during these years.

I also would like to express my gratitude to the following researchers for providing training on the following characterization instruments; from University of Nebraska–Lincoln: Dr. Xingzhong Li (HRTEM), Dr. Balamurugan Balasubramanian (XPS); from University of Kansas: Dr. Charles Ye (FTIR and Raman); and from Kansas State University: Dr. Dan Boyle (TEM).

I would like to acknowledge the Nebraska Nanoscale Facility: National Nanotechnology Coordinated Infrastructure and the Nebraska Center for Materials and Nanoscience (and/or NERCF), which are supported by the National Science Foundation under Award ECCS: 2025298, and the Nebraska Research Initiative. Also, the financial support from the National Science Foundation grant number 1454151 is gratefully acknowledged.

I am extremely thankful to my lab colleagues Zhongkan Ren and Shakir Bin Mujib for all their assistance during my Ph.D. Also, a big thanks to Dr. Lamuel David, my in-laws: Seu Romualdo Cintra and Dona Tita Cintra, and the great friends I have made in Manhattan, KS, in particular Barb and Tony Siebold.

Last and most importantly, I would like to thank Adriana and Pingo for loving & supporting me during all times.

Dedication

I dedicate this to my wife Adriana, who gives me the strength to reach beyond my limits, to our families, for their unconditional support. Also, to my niece Sarah and my nephew Théo for their contagious joy.

Chapter 1

Introduction and motivation

Nowadays, an increasing concern of governments and private institutions lies in providing conditions towards economic growth allied with environment-friendly initiatives to comply with international agreements that propose a decrease in greenhouse gas emissions, such as Kyoto Protocol and the Paris climate agreement. On the one hand, CO_2 emission reduction is seen as an effort that will benefit the whole world; on the other hand, the changing lifestyle and world population increase will require more energy. Aiming to supply this energy demand by 2050, energy equivalent to 10^{10} tons of oil, i.e. 130 000 TW h, must be produced yearly, leading to an increase in CO_2 emissions[1]. Therefore, keeping CO_2 emissions at a low level while producing more energy seems a complex problem to solve. First things first, less dependence on fossil fuels seems to be a good starting point, as according to figure 1.1 oil consumption can be directly related to emissions of this greenhouse gas.

Another point worthy of consideration is that exploitation of renewable energy sources – e.g., biomass, geothermal, solar, and wind – is one alternative to fulfill this energy demand. However, renewable energy sources are intermittent, and their energy generation is commonly not centralized. A solution to this intermittentness aspect of renewables is to store the excess of electricity when energy conversion is high and the demand is low, e.g., when solar panels are converting energy during a sunny day but people are not at home to use this energy. Subsequently, this stored energy can be released to the load when energy conversion is very

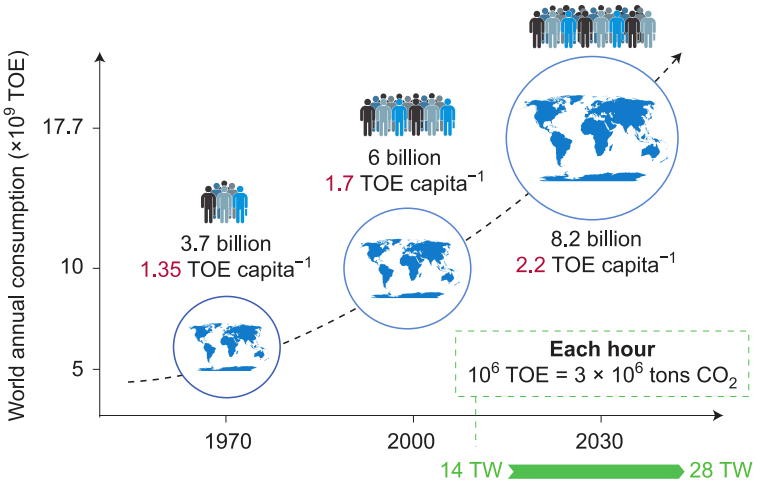

Figure 1.1: *Forecast of energy consumption and world population in the next decades. The energy demand is expect to double from 2010 (*14 TW*) to 2050 (*28 TW*). TOE = ton of oil equivalent. Copyright 2014, Nature Publishing Group, a division of Macmillan Publishers Limited. All Rights Reserved*[1].

low or negligible, e.g., at night when conversion from solar panels is negligible and people are at home[1]. Now, the question that arises is, how can one store this excess energy? Over the years, electrochemical energy storage (EES) has been a feasible form to store energy owing to high energy conversion efficiency, fast response to supply the load, and high power and high energy densities. As one example, in a battery electric vehicle (BEV), lithium-ion batteries (LIBs) present energy efficiency of 70%, i.e., 70% of the energy stored in LIBs in a BEV is effectively used to move the vehicle from point A to point B. On the other hand, in an internal combustion engine (ICE) only 15% of the total energy is effectively used to move the vehicle from point A to point B[2].

Furthermore, according to Gibb[2], approximately 55% of the population in cities sees that battery electric vehicles (BEVs) provide a substantial improvement in air quality. Thus, LIB is essential to the future of automobile industry because of higher energy efficiency and because consumers are sympathetic with LIBs technology due to environmental aspects.

Although LIBs are often in the news recently, they have been studied since the 1970s when Exxon Mobil Corporation hired Stanley Whittingham to develop a secondary (rechargeable) battery[3]. Due to the experience gathered and continuous development of materials, LIBs are currently the best performing devices in terms of energy density, due to Li reduction

potential ($-3.04\,\mathrm{V}$ *vs.* standard hydrogen electrode (SHE)) and long cycle life. As a safe technology available to the market since 1991, the energy density of LIB has been increasing on average 8% per year and is nowadays used not only in BEV but also in cell phones, portable electronic devices, and in grid energy storage.

Nevertheless, given the increasing demand for lithium precursor materials, the cost of these materials has also been following the same trend. Lithium metal presents meager availability on the earth's crust, and consequently concerns whether the worldwide estimated reserves of ≈ 14 million tons may meet the demand of a market that went from US$ 10 billion in 2010 to US$30 billion in 2020 (projected) are rising[4;5]. To quantify how lithium metal scarcity is an issue that companies and researchers should carefully look into, in 2008 the global consumption of lithium was 21,280 tons[6]. According to Wang et al.[7], from 2018 to 2019 the lithium consumption on earth increased $\approx 43\%$[7]. However, considering a modest growth rate of 10% per year on lithium use, the estimated lithium reserves could be exploited only for ≈ 55 years.

Arising from this concern, research on materials that can replace lithium – known as beyond LIB technologies – has received considerable attention recently. Examples of beyond LIB technologies are SIB and KIB. Figure 1.2(a,b) shows how research on KIB and SIB, respectively, has gained traction in the past few years.

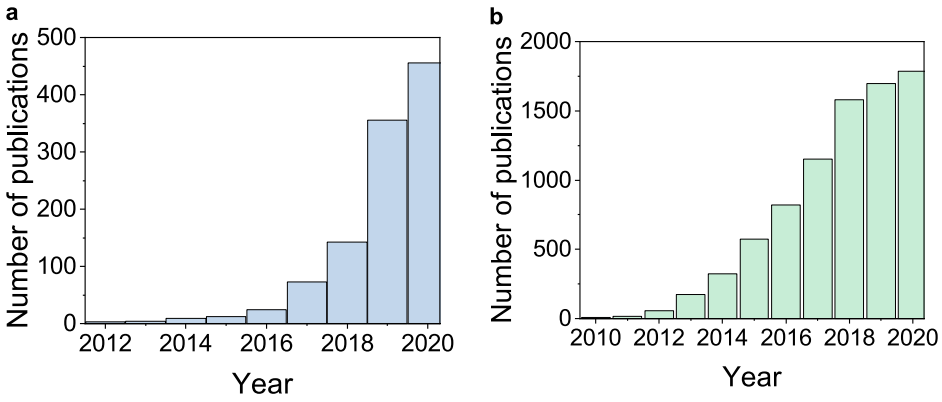

Figure 1.2: *Number of records in articles, books, and authentic open literature related to (a) potassium-ion batteries, and (b) sodium-ion batteries. Web of Science, April 25, 2021.*

Like lithium, sodium and potassium are also alkali metals. However, both sodium and

potassium present abundant availability on earth's crust. In the case of sodium, it can be obtained from abundant and low-cost salts – e.g., Na_2CO_3, Na_2SO_4, and NaCl[8]. Although SIB is deemed as a complementary technology to LIB, for applications such as energy grid storage SIBs are potential candidates due to reasonable energy density, long life cycle – mainly when solid electrolytes are used – and low cost. Hirsh and co-authors[9] have published a comprehensive discussion on this topic. Figure 1.3 shows a world map with reserves and soda ash (Na reserves) in 2020. Red circles depict Li reserves, and soda ash reserves are depicted by blue circles (the size of the circles represents the number of reserves in tons). Furthermore, as brine is a source of sodium, it is illustrated by the light blue color of the oceans; thus, corroborating the immense availability of Na in comparison to Li.

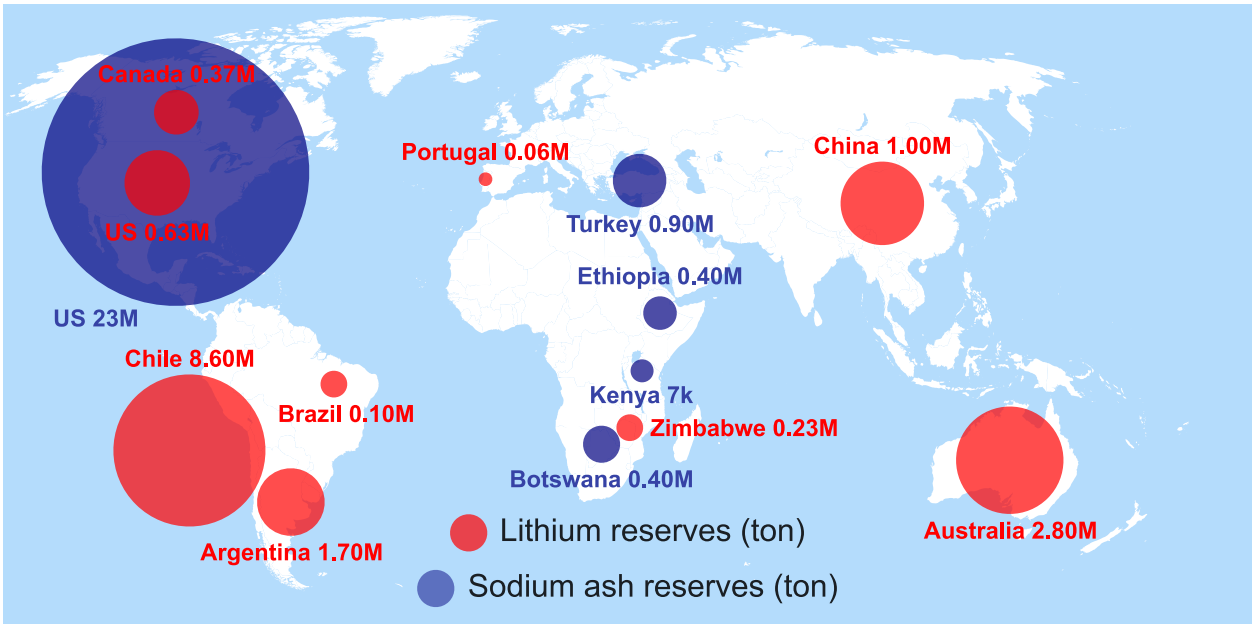

Figure 1.3: *World map showing the main Li and soda ash (Na reserves). It is worth noting that brine is also a source of sodium, which is highlighted in light blue color in the oceans*[9].

Likewise, potassium presents abundant availability on the earth's crust and oceans, with consequent low cost. This can be illustrated by the cost of potassium carbonate (≈ US$ 1,000 per ton), whereas lithium carbonate cost per ton is ≈ US$ 6,500 per ton[4]. Readers are reminded that technical aspects of sodium and potassium are discussed in detail in this thesis in sections 2.2 and 2.3, respectively.

Aware of the strategic importance of studying beyond LIB technologies, the task now is

to find and develop novel electrode materials that are safe and efficiently store energy, as well as to understand the chemistry and charge storage mechanism taking place in these materials as SIB and KIB electrodes. Such developments and a better understanding of the chemistry taking place in these systems can then assist in developing the next generation of batteries.

In summary, this Ph.D. thesis focuses on these aspects. Chapter 3 discusses and presents a mechanism to mitigate a stability issue recurrent of a particular material of interest with sulfur on its formula – sulfide-based – (for sodium-ion (Na^+ storage); therefore, as a SIB electrode material. Chapter 4 presents a contribution towards understanding potassium-ion (K^+) storage in another material of interest that has tellurium on its structure – telluride-based – as KIB. Lastly, chapter 5 presents a comparative work of Na^+ and K^+ storage in the telluride-based material reported in chapter 4, so certain assumptions in the battery community can be re-analyzed based on the presented discussion. The electrode materials studied in this thesis belong to the same family; section 2.6 presents a comprehensive discussion of this family of materials.

Chapter 2

Background & literature review

Batteries are devices with high energy density that can convert chemical energy obtained from a chemical reduction-oxidation reaction of active materials to electric energy. Concerning rechargeable batteries, the reduction-oxidation (redox) reaction is reversible; thus, through a reverse process, the battery can be charged to be re-used[10]. As the energy conversion process in batteries involves electrochemical energy, no combustion or heat laws are applied; thus, the conversion efficiency of batteries is much higher than for systems that obey the Carnot cycle, for instance[10]. Arising from these advantages, in the past century several battery technologies have been available to the market. As shown by figure 2.1, LIB have been leading the market due to high energy density.

2.1 Alkali-ion rechargeable battery technology [1]

Alkali-ion rechargeable battery technology – such as LIB – consists of a positive (cathode) and a negative (anode) electrodes separated by an electronic insulating separator (barrier). This separator intends to allow the metal-ion exchange in a medium but not electrons. The medium that provides ion movement is known as electrolyte, which for LIB usually consists of lithium salts dissolved in an organic solvent. Figure 2.2 shows a schematic of the first

[1] Reprinted from Soares, Davi Marcelo, et al. "Additive Manufacturing of Electrochemical Energy Storage Systems Electrodes." *Advanced Energy and Sustainability Research*: 2000111. Copyright, Advanced Energy and Sustainability Research published by Wiley-VCH GmbH.

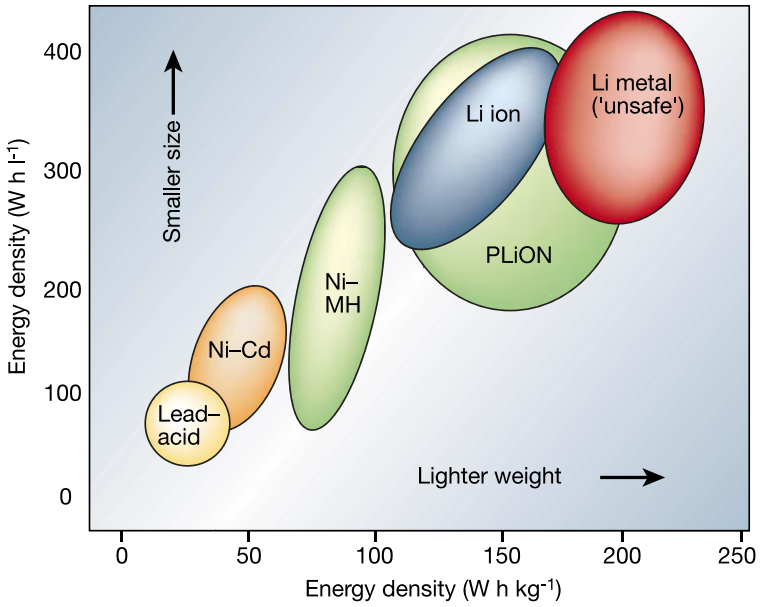

Figure 2.1: *Schematic of different rechargeable battery technologies. Except for Li metal batteries, lead-acid, nickel-cadmium (Ni-Cd), nickel metal-hydride (Ni-MH), LIB, and and plastic lithium-ion (PLiON) are commercially available. Copyright 2001, Nature Publishing Group*[11].

viable commercial LIB, developed by Akira Yoshino, one of the winners of the 2019 Nobel Prize in Chemistry.

When the LIB shown in figure 2.2 is charged, most lithium (working) ions are stored in the negative or anode electrode (petroleum coke). When the circuit is closed, and no external voltage is applied, the cell voltage will start to decrease (discharge) as lithium-ions will leave the anode electrode towards the positive electrode (cathode). Then, the anode material oxidation number increases, e.g., from $C^{1/6-}$ to C^{0}; whereas at the cathode the material oxidation number reduces. In other words, the anode loses an electron while the cathode gains an electron. Due to the high resistance of the electrolyte and separator, these electrons are forced to flow through an external circuit; therefore, powering the lamp (load) presented in figure 2.2. It is worth noting that during the discharge process in a LIB, lithium-ions move towards the cathode (layered cobalt oxide depicted by figure 2.2) in order to keep the charge neutrality. A reverse process can be obtained by forcing the lithium-ions to move back to the anode (negative) electrode; this is known as "*charging*" the battery.

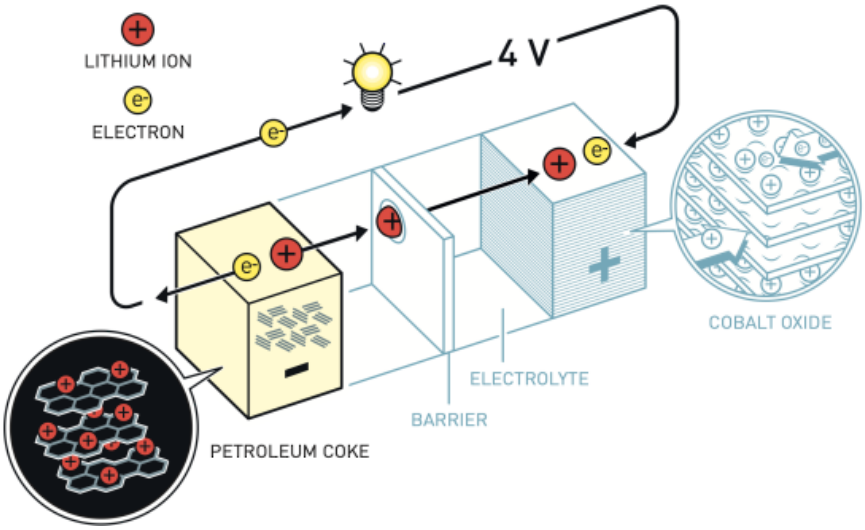

Figure 2.2: *Schematic of the first viable commercial LIB developed by Akira Yoshino. Illustration: Johan Jarnestad/The Royal Swedish Academy of Sciences.*

As the discharge is an spontaneous process, the open cell voltage can be determined by equation 2.1 [12].

$$voltage = -\frac{(\mu^c - \mu^a)}{z \cdot F} = -\frac{\Delta G_r}{z \cdot F} \tag{2.1}$$

Where in equation 2.1, μ^c and μ^a are the chemical potentials of cathode and anode electrodes, respectively, z is the valence of working ion (+1 for alkali-ions, e.g., Li^+, Na^+, or K^+), F corresponds to Faraday constant ($\approx 96\,485\,\mathrm{C\,mol^{-1}}$), and ΔG_r is the Gibbs free energy of reaction [13].

At this point, it is important to highlight that before the viable commercial LIB presented in figure 2.2 was developed, other layered materials were studied and some not very successfully commercialized.

In 1975 Whittingham and Gamble Jr. reported intercalation of lithium in titanium disulfide (TiS_2) [14]. In addition to reporting that TiS_2 could intercalate lithium-ions in van der Waals gap, authors also reported the same behavior for molybdenum disulfide (MoS_2) [14]. As shown by figure 2.3, in this work TiS_2 was used as cathode material along with a lithium-metal anode (negative electrode). This configuration led to the production of LIB with

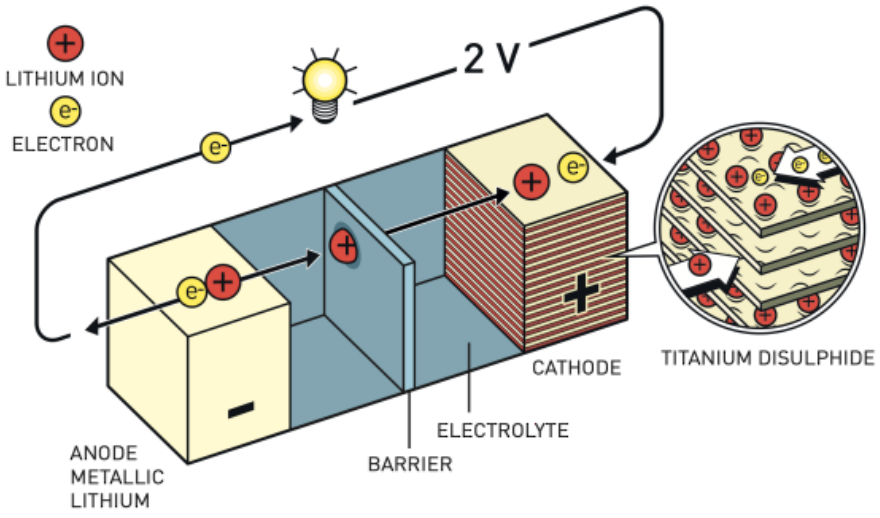

Figure 2.3: *Battery developed by M. Stanley Whittingham using TiS_2 as intercalation host for Li^+ [14]. Illustration: Johan Jarnestad/The Royal Swedish Academy of Sciences.*

metallic lithium anodes by companies, a configuration that later on was found to be unsafe.

In 1989, the Moli Energy Limited commercialized millions of LIB in "AA" cells size comprised of MoS_2 cathode and lithium-metal anode[15;16]. The cells released to the market ended up causing accidents and fires due to dendrite formation. These unfortunate events forced the company to recall all commercialized cells. Although these mentioned initiatives were not successful, they highlight a pioneering aspect of LIB as alkali-ion rechargeable battery technology, which is the use of layered sulfide-based electrode materials to store lithium-ions (e.g., TiS_2, MoS_2). A detailed discussion of one class of layered materials of interest for this thesis is presented in section 2.6.

The strategy of studying layered electrode materials has re-gained traction since 2004, when Geim and Novoselov reported the insulation of a monolayer of graphite – material known as graphene[17]. More than proving that a monolayer of graphite was stable under ambient conditions, these authors discovered a material with very high mobility and outstanding mechanical properties. As a result, this finding represented a gateway for research on materials that present stable mono- or few-layers forms, such as black phosphorus, layered perovskites, MXenes, hexagonal boron nitride, TMDs, and others that are yet to be discovered[18].

For energy storage applications, layered materials are of interest because such morphology allows ions to freely access the whole electrode material, unlike in bulk electrodes. Inherent during cycling in battery electrodes, phase transformations sometimes may lead to capacity drop and inactive sites for ions to access in the electrode. In addition, as presented in figure 2.4(a), in bulk (or 3D) electrodes expansion upon ion extraction may yield delamination or cracks on electrode materials due to mechanical stresses, again leading to an increase in internal resistance, higher losses, and consequent capacity decay (figure 2.4(b)). On the other hand, layered electrodes, as shown by figure 2.4(c), present negligible expansion because nanosheets are loosely stacked and may accommodate structural changes upon ion insertion and extraction. This feature may allow more storage of ions because the entire surface of the electrode is available; thus presenting optimal packing density[19]. As discussed in more detail in section 2.6, layered and 2D structures may also have their properties tuned, so a larger interlayer spacing can be obtained for storing larger ions[19].

Therefore, nowadays, what we have experienced in battery research is the pioneerism of M. S. Whittingham being re-ignited, as researchers are looking closely to layered materials as electrodes – similar to TiS_2 reported back in 1976 by Whittingham[20] – and methods to enable the safe use of alkali-metal anodes towards small devices with higher energy density[21].

2.2 Sodium-ion battery concepts[2]

SIBs are deemed as an alternative to LIBs for energy storage systems, owing to their similar chemical and physical properties, along with abundant sodium reserves in the earth's crust[22].

Although research on SIB dates back to 1980s, it was somewhat limited because sodium-ions (Na^+) have larger ionic radius (1.02 Å) when compared to Li^+ (0.76 Å), higher standard electrode potential (−2.71 V vs. SHE) than Li (−3.02 V vs. SHE) in aqueous media, and very low capacity toward conventional graphite ($< 35\,mA\,h\,g^{-1}$)[6;23]. Table 2.2 presents a comparative list of properties of some alkali-metal ions.

[2]Reprinted with permission from Soares, Davi Marcelo, Santanu Mukherjee, and Gurpreet Singh. "TMDs beyond MoS_2 for electrochemical energy storage." *Chemistry - A European Journal* (2020). Wiley-VCH Verlag GmbH & Co. KGaA, Weinheim.

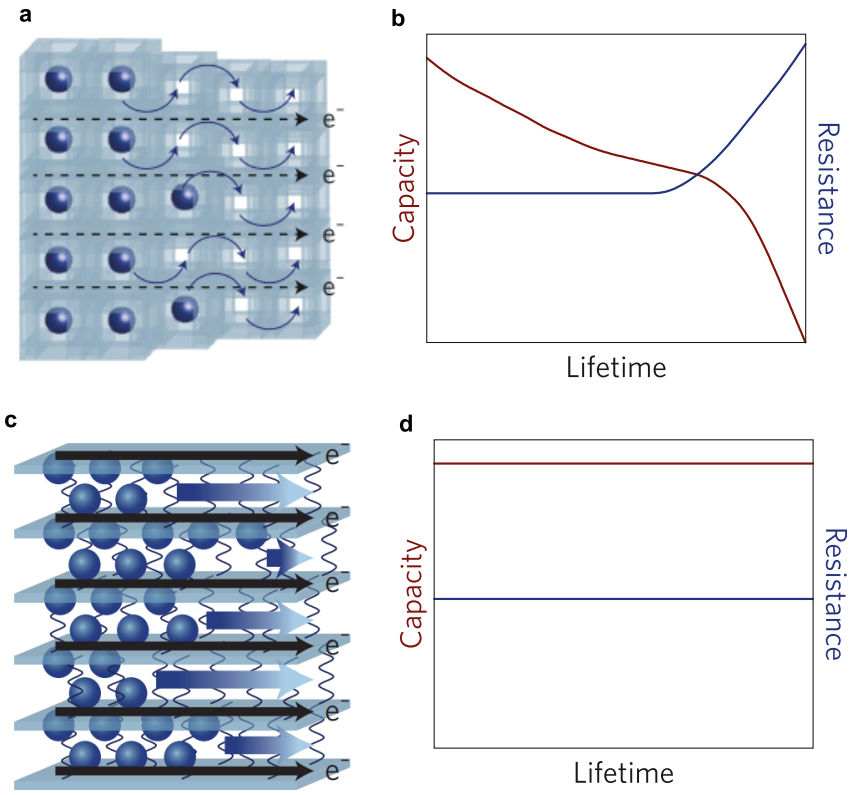

Figure 2.4: *Schematic of bulk and layered materials in battery electrodes. (a,b) 3D intercalation electrode. (c,d) Layered material with zero-expansion. Copyright 2017, Macmillan Publishers Limited*[19].

Graphite is deemed as a benchmark material in battery research. In the recent literature, several studies have been conducted to better understand the instability of Na^+ intercalation into graphite[24;25]. According to Hwang et al., graphite is thermodynamically unstable upon formation of NaC_6 and NaC_8 compounds, and it presents interlayer distance too small ($\approx$ 0.34 nm) to properly accommodate Na^+[6]. Corroborating the latter finding, Wen and co-workers reported that a suitable interlayer spacing of graphite for stable storage of Na^+ should be 0.37 nm[23]. To confirm their hypothesis, expanded graphite was synthesized with interlayer lattice distance of 4.3 Å. In 1 M $NaClO_4$ in polycarbonate solvent liquid electrolyte, the expanded graphite showed reversible capacity of 284 mA h g^{-1} at 20 mA g^{-1} towards Na^+[23]. Table 2.1 presents results of other developments in SIB in which graphite was employed as electrode material.

At this point, the readers of this thesis may have questions concerning the fact that Na^+

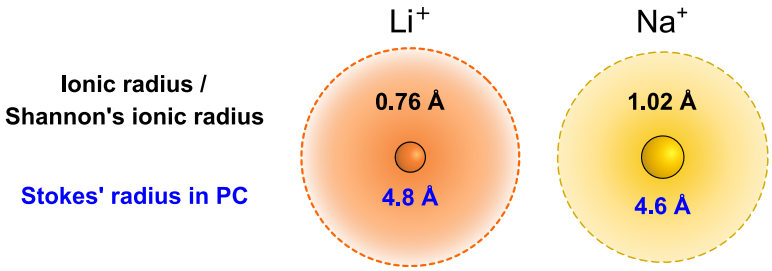

Figure 2.5: *Comparison of ionic radius, or Shannon's ionic radius, and Stokes' radius in PC of Li^+ (benchmark) and Na^+. Adapted from[26]. 2018 The Chemical Society of Japan & Wiley-VCH Verlag GmbH & Co. KGaA, Weinheim.*

radius was reported to be 1.02 Å, but the interlayer spacing of graphite (≈ 3.7 Å) was found to be not compatible for insertion of Na^+. How is that possible, considering the interlayer spacing of graphite is more than three times larger than the informed Na^+ radius?

The answer to this question is adequately discussed in chapter 5 of this thesis. The short answer is that reporting the ionic radius of Li^+, Na^+, or K^+ alone does not provide meaningful information of the electrolyte interaction with this ion. Thus, any conclusions require information of the Stokes' radius of the ion under consideration, as it takes into account the interaction of this ion with the electrolyte medium[26]. Figure 2.5 shows that in PC the Stokes' radius of Na^+ is, indeed, smaller than of Li^+; thus, counter-intuitive as often conveyed in the literature. Therefore, analyzing or reporting only the ionic radius can sometimes be misleading.

Another challenge that SIBs face is that using sodium-metal anode in SIBs poses a risk due to unstable Na^+ plating, which may lead to dendrite formation – aspect akin to using Li metal anode in LIBs. The higher reactivity of sodium and its lower melting point (i.e., 97.8 °C compared to 179 °C of Li) may result in risky thermal-runaway reactions caused by dendrite[27]. Although several dendrite-free materials have been studied, the theoretical specific capacity (1166 mA h g^{-1}), low anode potential, and low-cost of sodium metal (US$ 200 ton^{-1}) are difficult to surpass[28].

Recently, using an innovative approach to address the dendrite challenge on SIB, Yu and co-authors introduced a graphene lattice made by direct ink writing (DIW) – an AM technique – based on the concept that porous electrodes yield low current densities and

homogeneous sodium plating distribution, as shown in figure 2.6(a–d). The printed periodical structure in figure 2.6(e) showed that the current density distribution at the circumference rim regions was high, indicating preferential spots for sodium deposition (2.6(e,f)). At current density of 1 mA/cm^2, initially the wholes shown in figure 2.6(b) were preferential nucleation sites for homogeneous sodium infusion, as shown by the SEM image after cycling in figure 2.6(c,d). The successive layers of deposited graphene oxide (GO) allowed precise pore control size of 500 µm, differing from traditional template method synthesis that typically does not present precise morphology control[29]. Overall, precise morphology control from the additive manufacturing enhanced the electrochemical performance in terms of coulombic efficiency and voltage polarization and allowed accurate control of sodium deposition in the electrode while suppressing dendrite formation.

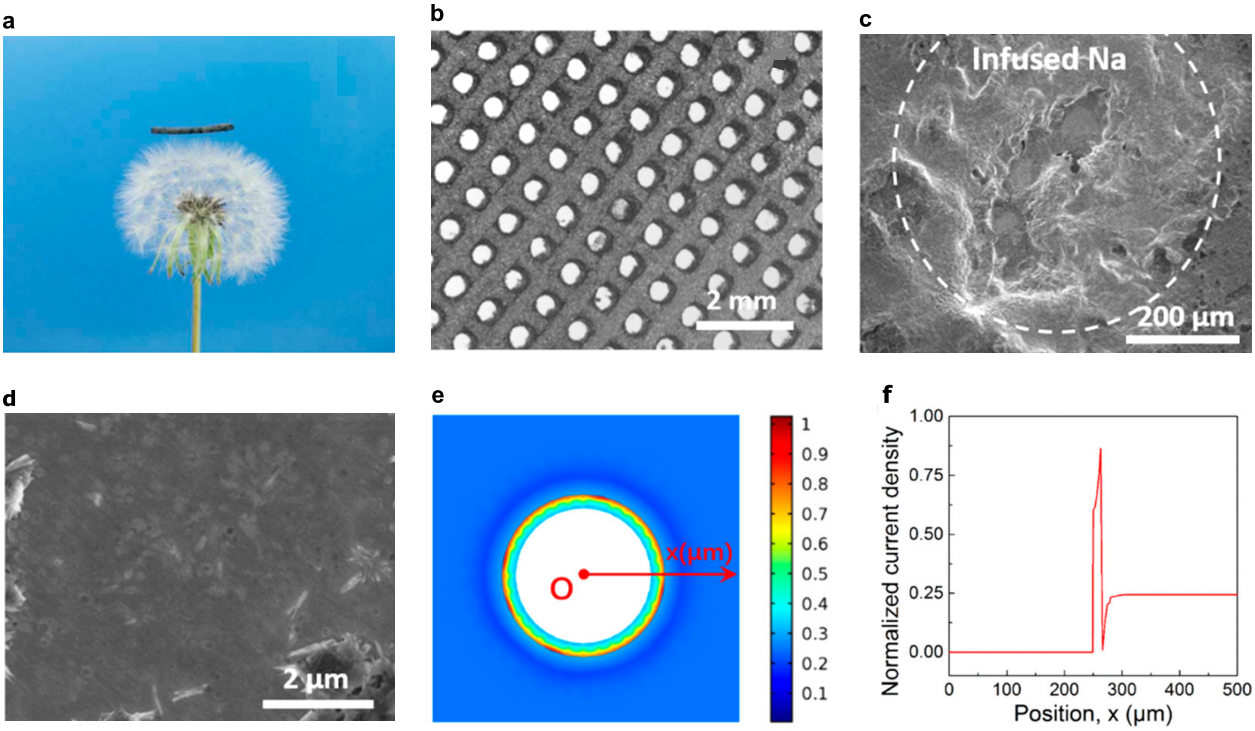

Figure 2.6: *3D printing of hierarchical graphene lattice (GL). (a) Representation of a light-weight electrode sitting on a dandelion flower. (b) Optical microscopy depicting the periodic structure of GL. (c,d) SEM images showing Na deposition preferential spots covering the whole on the periodic structure. (e,f) Current distribution profile at GL structure[29]. Copyright 2019, American Chemical Society.*

In terms of research beyond graphite electrodes for SIBs, layered sulfide-based materials

– i.e., materials with a layered structure that contain sulfur on their formula – are in prominence. The rationale for such is that more capacity and energy densities can be obtained when using these materials than graphite and other carbon-based electrode materials, as shown by the dark green data points in figure 2.7. A comprehensive discussion about the class of materials whose electrochemical performance is below described and explaining why they yield high capacity is presented in section 2.6.

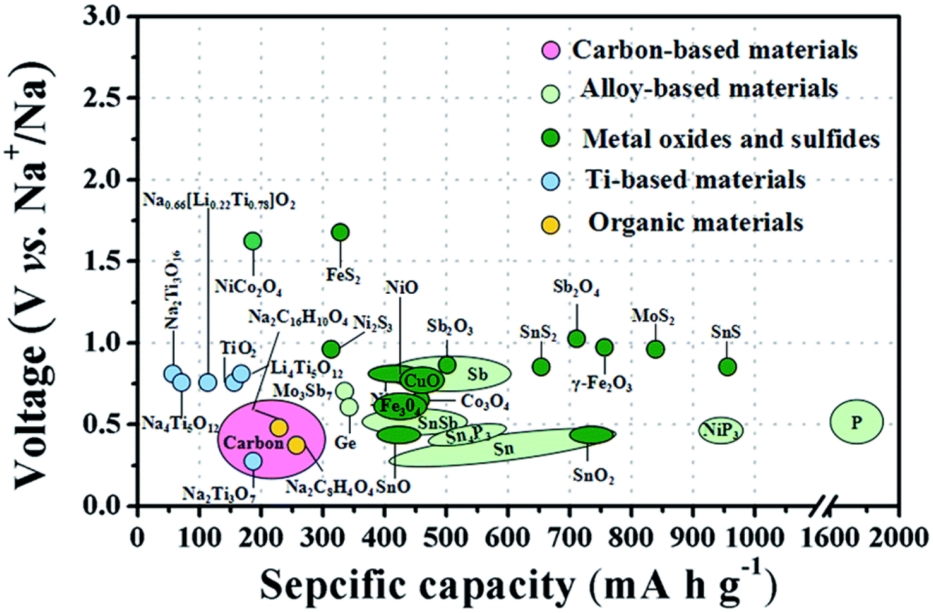

Figure 2.7: *Chart of average voltage discharge versus specific capacity of anode materials for SIBs[30]. Copyright Royal Society of Chemistry*

As previously discussed for graphite materials, the strategy of increasing the interlayer spacing is also applied to layered sulfide-based materials. Liu et al. expanded interlayer spacing of WS_2 nanowires (NWs) to 8.3 Å solvothermally with subsequent heat treatment[31]. The expanded interlayer spacing offered improved ionic accessibility for faster Na^+ intercalation and deintercalation during cycling. WS_2 NWs displayed a capacity of 605.3 mA h g^{-1} at 100 mA g^{-1}, as anode for SIBs for the voltage range from 0.01 - 2.5 V. Furthermore, for a different voltage range, i.e., 0.5 - 3 V, authors reported that WS_2 NWs presented an exfoliation process upon change and discharge, which, therefore, provided more available sites for Na^+ intercalation. Under this condition, the synthesized material presented, at 1 A g^{-1}, charge capacity of 330 mA h g^{-1} after 1400 cycles[31].

ReS_2 (rhenium disulfide) is also a species of interest for SIB given its lower interlayer coupling energy and the fact that it exhibits 1T′ phase; this phase is discussed in more details in section 2.9[32]. Mao et al. synthesized flexible ReS_2 nanosheets onto nitrogen doped carbon nanofibers (N-CNF) (ReS_2/NCNFs) paper as Na^+ ion battery anodes[33]. Intuitively, the carbon nanofibers (CNFs) improved the electronic conductivity, whilst the doped nitrogen could absorb sulfur and polysulfide species during conversion reactions. As a result, the ReS_2/N-CNFs anode yielded a reversible capacity of $245\,mA\,h\,g^{-1}$ after 800 cycles at $100\,mA\,g^{-1}$ as SIB anode. Very recently, Chen et al. reported a 1T′-ReS_2 with reduced graphene oxide (rGO) and N-doped carbon layer (rGO@ReS_2@N-C)[34]. The rGO@ReS_2@N-C electrode in SIB exhibited a capacity of $231\,mA\,h\,g^{-1}$ at $10\,A\,g^{-1}$, and a long-term cycling capacity of $192\,mA\,h\,g^{-1}$ at $2\,A\,g^{-1}$ after 4000 cycles. Authors attributed the performance to the enhanced electrical conductivity, as well as Na^+ adsorption and diffusion kinetics, to suitable interface between carbonaceous materials and 1T′-ReS_2[34].

Kim et al. reported for the first time using FeS_2 (pyrite) as cathode in SIBs[35]. The sodium/pyrite cell showed discharge capacity of $630\,mA\,h\,g^{-1}$ at $50\,mA\,g^{-1}$. In this study, authors proposed FeS_2 reduction discharge reaction may take place as follows (2.2):

$$3Na + FeS_2 \longrightarrow Na_3S_2 + Fe \tag{2.2}$$

It is worth noting that in this study, authors indicate reasons for irreversible capacity drop. From SEM images agglomerated shapes were identified during insertion reaction – discharge – which are assigned to sodium polysulfides in the electrolyte. Moreover, upon charging, the agglomerate remained; which, therefore, may be a reason for a discharge decay from $630\,mA\,h\,g^{-1}$ to $85\,mA\,h\,g^{-1}$, after 50^{th} cycles[35]. Indeed, polysulfide dissolution still a challenge when studying layered sulfide-based materials – e.g., TMDs – for energy storage systems (ESS), aspect that is addressed in this thesis in chapter 3[36]. As of 2015, Walter et al. synthesized FeS_2 nanocrystals (NCs) as anode in SIBs[37]. They showed that, as anode material, FeS_2 NCs provided specific capacities higher than $500\,mA\,h\,g^{-1}$ at 400^{th} cycle, at current density of $1\,A\,g^{-1}$. In addition, Hu et al. studied the electrochemical behavior

varying electrolyte species and voltage window in Na/FeS_2 cells[38]. In half-cell configuration, authors showed that by tweaking the cut-off voltage for charge-discharge, the rate capability is considerably altered. For a voltage window of 0.1 - 3 V, at 200 mA g^{-1}, within 50 cycles, the specific capacity varied from 780 to 100 mA h g^{-1}. In contrast, high degree of reversibility was achieved for a voltage window from 0.8 - 3 V; therefore, considerable decay within 50 cycles is no longer observed; thus, an evidence that the process of capacity decay is voltage-dependent[38]. More recently, FeS_2 nanosheets encapsulated on 3D porous carbon spheres (FeS_2@C-2 h) were synthesized using initially Fe_2O_3 hollow nanospheres by Wang et al.[39]. The final material, FeS_2@C-2 h, presented characteristic morphology, whose porous structure assisted in volumetric expansion and shrinkage upon sodiation/desodiation processes. From electrochemical impedance spectroscopy, FeS_2@C-2 h outperforms both FeS_2 and FeS_2@C materials, i.e. presents the lowest equivalent series resistance (R_{esr}) and charge transfer resistance (R_{ct}).

VS_2, which behaves as a metallic species, and has many intriguing chemical and physical properties. Despite its first synthesis is reported back in 1977[40], the synthesis of 2D high-purity VS_2 nanosheets by hydrothermal methods is still challenging. Zhou et al. synthesized hierarchical VS_2 nanosheet assemblies (NSA) comprised of aligned ultrathin nanosheets[41]. VS_2 NSA were prepared via a facile solvothermal reaction, which involves vanadyl acetylacetonate ($VO(acac)_2$) and cysteine as the precursors. As anode for SIB, VS_2 NSA provided specific capacity of approximately 700 mA h g^{-1} at a current density of 100 mA g^{-1}; moreover, excellent rate capability of 400 mA h g^{-1} at 2 A g^{-1} was also reported by the authors. Recently, three-dimensional hierarchical VS_2 structure as anode for SIBs was reported by Wang et al.[42]. According to the authors, even though the synthesis of 3D hierarchical VS_2 spheres was not performed by chemical vapor deposition (CVD), a high degree of purity was ascribed to the sample based on XRD results. The latter analysis also revealed a hexagonal crystal structure. Also, the 3D morphology provided space for volume expansion upon insertion and extraction of Na^+ and facilitated electrolyte diffusion. Accordingly, an initial coulombic efficiency of 96% is reported, and reversible capacity of 720 mA h g^{-1} was achieved after 100 cycles. Finally, the rate capability test showed after 1000 cycles at current density

of 2 A g^{-1} 565 mA h g^{-1}. Thus, showing the potential of this layered sulfide-based metallic material.

Sn-based compounds have shown good prospect as high-capacity SIB anodes based on the theoretical stoichiometry of $Na_{15}Sn_4$ (847 mA h g^{-1})[43]. Prikhodchenko et al. synthesized a nanocrystalline SnS_2 coating of rGO produced by the peroxostannate deposition route for SIB anodes[44]. According to the authors, GO-SnS_2 contains a high concentration of rhombohedral SnS_2 with average size of 2.6 nm, where planes (001) were preferentially oriented in parallel to graphene oxide sheets. With little specific capacity contribution from carbonaceous materials, i.e. approximately 46 mA h g^{-1} at 50 mA g^{-1}, GO-SnS_2 presented 600 mA h g^{-1} for 50 cycles, with coulombic efficiency of 99.6%. Synthesis of SnS_2 nanosheets confined in carbon nanostructures was reported by Liu et al.[45]. They synthesized SnS_2 ultrathin nanosheets confined in carbon nanotubes (SnS_2@carbon nano tubes (CNTs)) using MnO_x nanorods as templates. Upon employing Fe_2O_3 nanocubes or SiO_2 nanospheres as templates, the authors found out that SnS_2 nanosheets are confined in carbon "nanoboxes", namely SnS_2@CNBs. Also, a morphology known as hollow carbon nanospheres can be obtained, namely SnS_2@CNSs. At 200 mA g^{-1}, SnS_2@CNSs SIB anode delivered a specific capacity of $\approx$ 634 mA h g^{-1}. According to the authors, the carbon shell high surface area may assist in diffusing Na^+ ions, in addition to increasing electronic conductivity and acting as a buffer[45]. Similarly, Zhang et al.[46] reported SnS_2/rGO, synthesized by solvothermal method. In this work, in comparison to MoS_2 and WS_2, for instance, authors reinforce different mechanism of alloying and de-alloying for Sb and Sn based TMDs. Nevertheless, from layered SnS_2, reversible reaction may happen. Results presented capacity retention of 89% up to 400th cycle at current density of 800 mA g^{-1}, in which an initial capacitance was found to be 469 mA h g^{-1}. In addition, at a higher current density, i.e., 12.8 A g^{-1} (about 28 C), the SnS_2/rGO showed a specific charge capacity of 337 mA h g^{-1}.

Recently, Brown et al. used a 3D freeze-printing (3DFP) method to produce a novel hybrid, highly porous MoS_2-rGO electrode[47]. Using a nickel foam current collector, ink-jet printing deposited a water-based ink made from commercially available reagents, namely, ammonium thiomolybdate (ATM) and GO. Performed at −30 °C, the freeze cast caused

the ATM-GO ink to freeze into ice crystals and form a porous and continuous matrix[47]. Following the sublimation process – induced to remove the ice template completely – a single annealing process was conducted to preserve the porosity and convert the ATM into MoS_2 and the GO into rGO. Then the produced MoS_2-rGO aerogel was studied as a half-cell SIB. The charge and discharge curves showed unique behavior compared to a typical pristine MoS_2-SIB voltage profile, including surface pseudocapacitive behavior per cyclic voltammogram curves. Therefore, since surface pseudocapacitive behavior infers a charge storage mechanism based on fast surface reactions, the high porosity of MoS_2-rGO was shown to impact specific capacity[48]. Since processes rapidly occur at high current densities, the specific capacity at low current densities was low but stable. On the other hand, at lower rates, since a conversion-type mechanism has a major contribution, a specific charge capacity closer to the theoretical value can be achieved. The authors also highlighted the advantages of rGO for a continuous and electronically conducting scaffold, which is essential at high rates. Overall, their research combined two promising ESS materials, MoS_2 and rGO, and introduced a Na^+ host material with enhanced electrochemical properties during additive manufacturing[47].

As depicted in figure 2.7, some metal oxides are known due to their high specific capacity in SIBs. Using a state-of-the-art manufacturing process, Down et al. reported a freestanding sodium-ion full-cell developed entirely using 3D-printed components[49]. Microporous electrodes such as TiO_2 (anode) and $NaMnO_2$ (cathode) were printed with ABS and polyvinyl alcohol (PVA); the PVA was infused in ABS and later washed away to maximize the surface area of the electrodes, a relevant factor in electrochemical performance. In addition, no separator was required in this fully printed cell, meaning the electrolyte was inserted into the cell AA battery layout, and the electrodes were kept apart due to the cell's design. Also, the freestanding nature of the electrodes did not require a current collector. Full cells were tested in 0.5 M $NaBF_4$ in EMIBF, and the AM/3D-printed full-cell presented $83.4\,mA\,h\,g^{-1}$ at $8.43\,mA\,g^{-1}$ (0.1 C). For comparison, an ink-based electrode – made by dr blade – was also tested and presented a first-cycle specific capacity of $98.9\,mA\,h\,g^{-1}$ at 0.1 C[50]. Overall, additive manufactured electrode batteries may advantageously provide innovative production

and cell design, porous microstructured filaments, and decreased component costs. However, challenges such as decreasing the viscosity of ionic liquids while increasing their ionic conductivity and enhancing the electronic conductivity of fully produced AM electrodes remain.

In the context of layered selenide-based electrode materials for SIBs, $MoSe_2$ has also gained increasing attention. Ko et al. reported for the first time in 2014 the synthesis of yolk–shell-structured $MoSe_2$ microspheres by a facile selenization process for application as anode material in SIBs[51]. The synthesized yolk–shell morphology presented flower-like structure, which according to the authors facilitated Na^+ and electronic kinetics and assisted in the volume changes during charge and discharge cycles[51]. Initially, the yolk-shell-structured $MoSe_2$ microspheres showed 85% coulombic efficiency, with an initial charge capacity of 448 mA h g^{-1} at 200 mA g^{-1}. Also, Wang and coworkers reported layered 2H-$MoSe_2$ nanoplates as anode materials for SIBs[52]. Such material delivered an initial discharge and charge capacities, respectively, of 513 and 440 mA h g^{-1} at approximately 43 mA g^{-1} [52]. Using a surfactant-directed hydrothermal method, Zhao et al. reported a controlled growth of $MoSe_2$ nanosheets on graphene[53]. The resulting 2D nanocomposite, through its strong electronic coupling, facilitated both electron and Na-ion transfer across the interface and exhibited reversible insertion/extraction of Na-ion, enabling fast pseudocapacitive Na-ion storage and stability for over 1500 cycles at current density of 3.2 A g^{-1} delivering reversible capacity of 368 mA h g^{-1}.

As an SIB anode material, Zhang et al. studied $SnSe_2$ 2D anodes for SIBs because of their high theoretical capacity, i.e., 756 mA h g^{-1} [54]. Authors reported $SnSe_2$/rGO nanocomposites for the first time, using a stable selenium source. $SnSe_2$/rGO delivered a reversible specific capacity of 515 mA h g^{-1} after 100 cycles at 1 mA g^{-1}. Furthermore, at 2 A g^{-1} the specific capacity delivered was 365 mA h g^{-1}. Figure 2.8 presents main finds from a study recently published by Zhang et al., in which $SnSe_2$ nanoparticles were encapsulated in a carbon shell, material named $SeSe_2$@C[55].

Regarding WSe_2, Share et al. demonstrated it as an electrode for the first time in SIBs[56]. A reversible capacity of WSe_2 pristine electrode reported was about 200 mA h g^{-1} at 20 mA g^{-1}. More recently, carbon-coated WSe_2 was synthesized using solid-state reaction

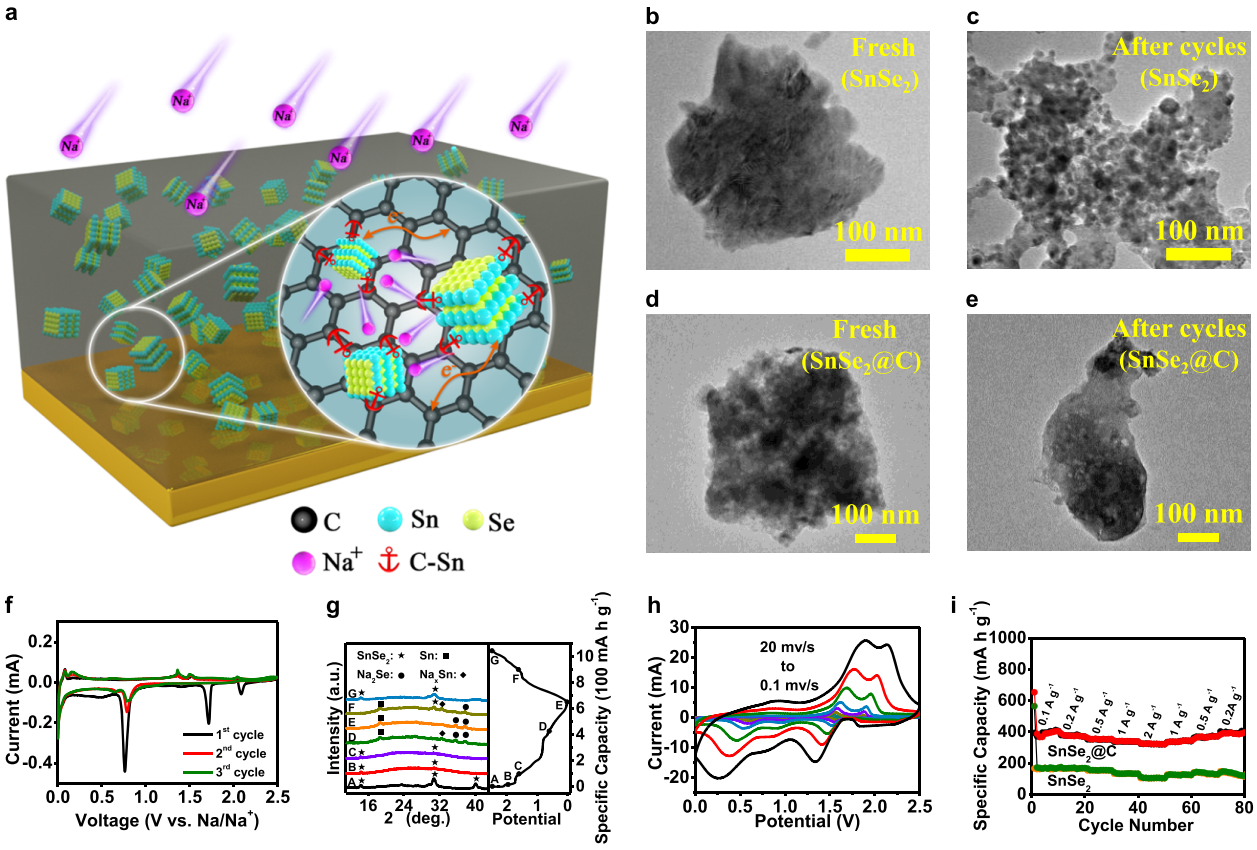

Figure 2.8: *(a) Illustration of the proposed Na^+ insertion/extraction mechanisms in $SnSe_2$@C composite; TEM of (b) $SnSe_2$ before cycling, and (c) $SnSe_2$ after 100 cycles, (d) $SnSe_2$@C before cycling, and (c) $SnSe_2$@C after 100 cycles. For both materials the current density and voltage window were, respectively, $2\,A\,g^{-1}$ and 0.01 - 2.5 V. It is possible to see the higher degree of pulverization that took place in the pristine $SnSe_2$. (f) CV for scan rate $0.1\,mV\,s^{-1}$ showing the redox peaks for the three first cycles. (g) ex-situ XRD of $SnSe_2$@C. (h) CV of $SnSe_2$@C for different scan rates. (i) rate capability[55]. Copyright 2020, American Chemical Society.*

by Zhang et al.[57]. In this study, tungsten and selenium were first ground by mechanical milling in their powder forms and subsequently annealed with carbon black. Afterwards, the WSe_2/C was directly used on electrode. WSe_2/C nanomaterials exhibited discharge capacity of $467\,mA\,h\,g^{-1}$ at $200\,mA\,g^{-1}$ current density, owing to the buffering of the carbon matrix and enhanced electronic conductivity of the composites.

In summary, based on this literature review, one can see that despite showing promising results for graphite, selenide- and sulfide-based materials only recently – a consequence of lower attention and efforts put into sodium chemistry research – SIBs present great potential

as a viable technology for several applications in the future. This can be confirmed by the fact that SIBs are currently used in large-scale electricity storage (e.g., stationary batteries) as evidenced by the approximately 200 units of HT-NSBs used by the NGK Company worldwide[58].

Likewise, one can conclude that certain layered sulfide-based and metal oxides have shown potential to become candidates for this next generation of SIB battery electrodes due to the promise of higher energy densities (figure 2.7). Yet in addition to the electrochemical performance, the availability of materials reported in this section must also be taken into consideration when it comes to commercial applications, because of the direct impact on of it on battery costs, as reported in the comprehensive work of Vaalma and co-authors[8].

In this regard, MoS_2 is layered sulfide-based material, easily available on earth that has been studied for several applications[59]. However, as reported in this literature review, capacity decay and the semiconducting nature of the thermodynamically preferred phase are drawbacks of MoS_2. These issues are known for a long time, and researchers have found that the use of carbon additives addresses drawbacks towards increased conductivity, effective stress relief, accommodation of large volume expansion/shrinkage, and facilitation of electron and Na^+ ion transport, as shown in table 2.1.

Nevertheless, to enable the utilization of MoS_2, stability upon cycling is still also a challenge. The chapter 3 of this thesis presents a comprehensive research work that intends to address this stability issue of MoS_2 upon using a supporting ceramic material with sp^2 free carbon domains – that yield higher electronic conductivity. To conclude, continuity of research will bring a better understanding of the electrochemical behavior of Na^+ for sulfide-based electrode materials, and this thesis intends to contribute to serving this purpose.

2.3 Potassium-ion battery concepts[3]

Emerging as another alternative to LIBs, KIBs are object of intense research since 2015 due potassium abundance in earth's crust, ocean, and relative non-toxicity[73].

Although presenting ionic radius larger than Li^+ (figure 2.9), K^+ presents the closest standard electrode potential to lithium in aqueous medium, i.e., E^0 (Li/Li^+) vs. SHE is $-3.04\,V$, whereas E^0 (K/K^+) vs. SHE is $-2.93\,V$[74]. A detailed comparative list of properties can be found in table 2.2. Re-emphasizing the discussion started in section 2.2, which highlighted that electrolyte media shall always be considered when reporting ion radii, Okoshi et al. reported ion-solvent interaction energies of Li, Na, Mg, and K in several solvents[75]. In all solvents evaluated, K^+ showed the lowest ion-solvent interaction energy[75]. According to the authors, this superior performance of K^+ occurred due to low reaction resistance arising from small desolvation activation energy, and high ionic mobility of K^+ in the aqueous and non-aqueous electrolytes analyzed because of small solvated ionic radius[75].

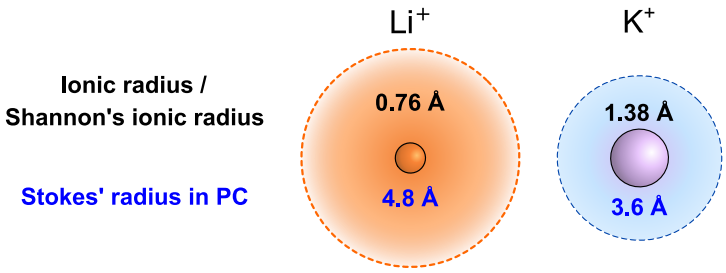

Figure 2.9: *Comparison of ionic radius, or Shannon's ionic radius, and Stokes' radius in PC of Li^+ (benchmark) and K^+. Adapted from[26]. 2018 The Chemical Society of Japan & Wiley-VCH Verlag GmbH & Co. KGaA, Weinheim.*

As a consequence of higher mobility of K^+ in electrolyte and smaller Stokes' radius, conventional graphite may accommodate reversible insertion and extraction of K^+[74]. Zhao et al. evaluated the electrochemical behavior of graphite as electrode material for KIB. Results showed the formation of KC_8 and reversible capacity of $246\,mA\,h\,g^{-1}$ at $20\,mA\,g^{-1}$ with 89% capacity retention after 200 cycles in 1 M KPF_6 EC:PC[74]; therefore, showing cycling

[3]Reprinted with permission from Soares, Davi Marcelo, Santanu Mukherjee, and Gurpreet Singh. "TMDs beyond MoS_2 for electrochemical energy storage." *Chemistry - A European Journal* (2020). Wiley-VCH Verlag GmbH & Co. KGaA, Weinheim.

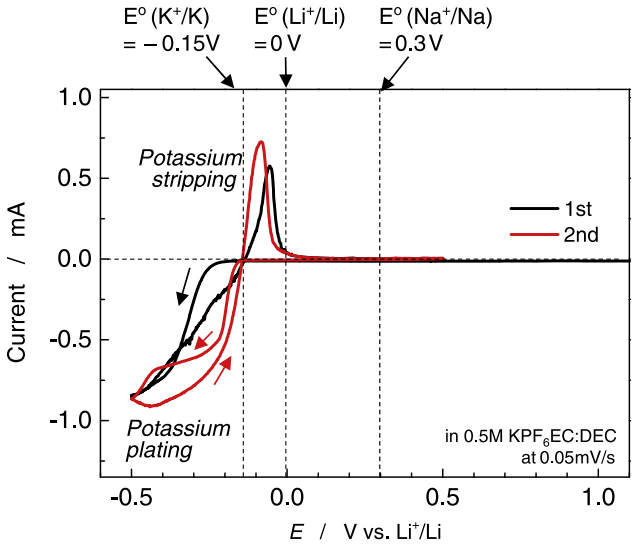

Figure 2.10: *Cyclic voltammograms of Ni mesh electrode in* $0.5\,\mathrm{mol/dm^3}$ *of* KPF_6 *EC:DEC at scan rate of* $0.05\,\mathrm{mV\,s^{-1}}$. *Copyright 2015 Elsevier B.V. All rights reserved*[77].

stability comparable to LIB.

In the work of Komaba et al., standard potential of $\mathrm{K/K^+}$ was evaluated by theoretical and experimental approaches for different electrolytes[77]. Firstly, based on standard molar Gibbs free energy calculation[78], the standard potential of $\mathrm{K/K^+}$ in PC was found to be $-0.09\,\mathrm{V}$ vs $\mathrm{Li/Li^+}$, i.e., the $\mathrm{E^0}$ of $\mathrm{Li/Li^+} = -2.79\,\mathrm{V}$ vs. SHE, whereas the $\mathrm{E^0}$ of $\mathrm{K/K^+} = -2.88\,\mathrm{V}$ vs. SHE[78]. In addition, according to Nerst equation, for EC:DMC electrolyte the calculated standard potential of $\mathrm{K/K^+}$ was found to be $-0.12\,\mathrm{V}$ vs $\mathrm{Li/Li^+}$; result that was corroborated experimentally, as figure 2.10 exhibits plating/stripping currents at $-0.15\,\mathrm{V}$ vs $\mathrm{Li/Li^+}$[77]. For the two electrolyte media studied, these results first indicate that the standard electrode potential depends upon the electrolyte, i.e., solvation state of $\mathrm{K^+}$. Secondly, one can see that KIB may present a good performance as high-voltage cells because potassium exhibited wider standard electrode potential ($\Delta\mathrm{E} = 4.6\,\mathrm{V}$) than lithium ($\Delta\mathrm{E} = 4.5\,\mathrm{V}$)[73].

Arising from these promising properties and growing research into layered electrode materials for KIBs, there are already documented results in the literature; some of these are presented in figure 2.11. Moreover, relevant results are discussed in this section with a major focus on layered selenide- and sulfide-based TMDs. Readers are reminded that TMDs are explained in detail in section 2.6.

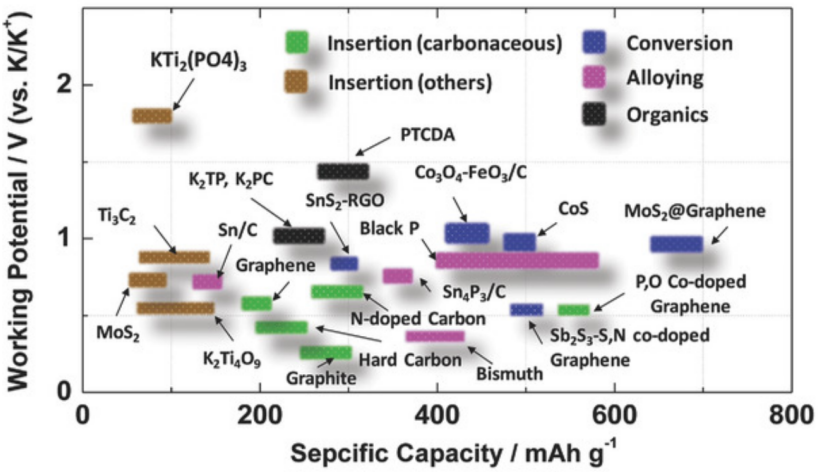

Figure 2.11: *Chart of average voltage discharge versus specific capacity of anode materials for KIBs*[79]*. Copyright © 2018 WILEY-VCH Verlag GmbH & Co. KGaA, Weinheim*

In terms of sulfide-based TMDs, Zhou et al.[41] reported the synthesis of hierarchical VS_2 nanosheet assemblies (NSA) or ultrathin few-layered VS_2 nanosheets (figure 2.12(a)), material tested as LIB, SIB, and KIB. Figure 2.12(b-d) presents the morphology of the material, which, according to the authors, possess larger exposed surface area and greater nanosheets interspacing. For the KIB half-cell tested in 0.5 M KPF_6 in EC:DEC, first cycle charge capacity was approximately 380 mA h g^{-1}, value that increased to 410 mA h g^{-1} after 600 cycles, all performed at 100 mA g^{-1}. Likewise, by increasing the current density to 500 mA g^{-1}, the initial specific charge capacity increased from approximately 290 to 360 mA h g^{-1} after 100 cycles. Authors believe that such increase can be assigned to surface wettability by the electrolyte; therefore, providing more active sites. It is worth noting that authors also present theoretical results from density-functional theory (DFT) calculations – a trend in high-impact publications these days.

Lakshmi and co-workers reported nanocrystalline SnS_2 dispersed on rGO sheets, the latter playing a role in minimizing the volume changes during cycling[80]. Cycled at 25 mA g^{-1} in half-cell configuration, the KIB presented initial charge and discharge specific capacities of 355 mA h g^{-1} and 630 mA h g^{-1}, respectively. On the other hand, the reversible charge capacity at a current density of 2 A g^{-1} was found to be 120 mA h g^{-1}. Conversely, authors also report that the addition of FEC in the electrolyte may have an undesirable effect for

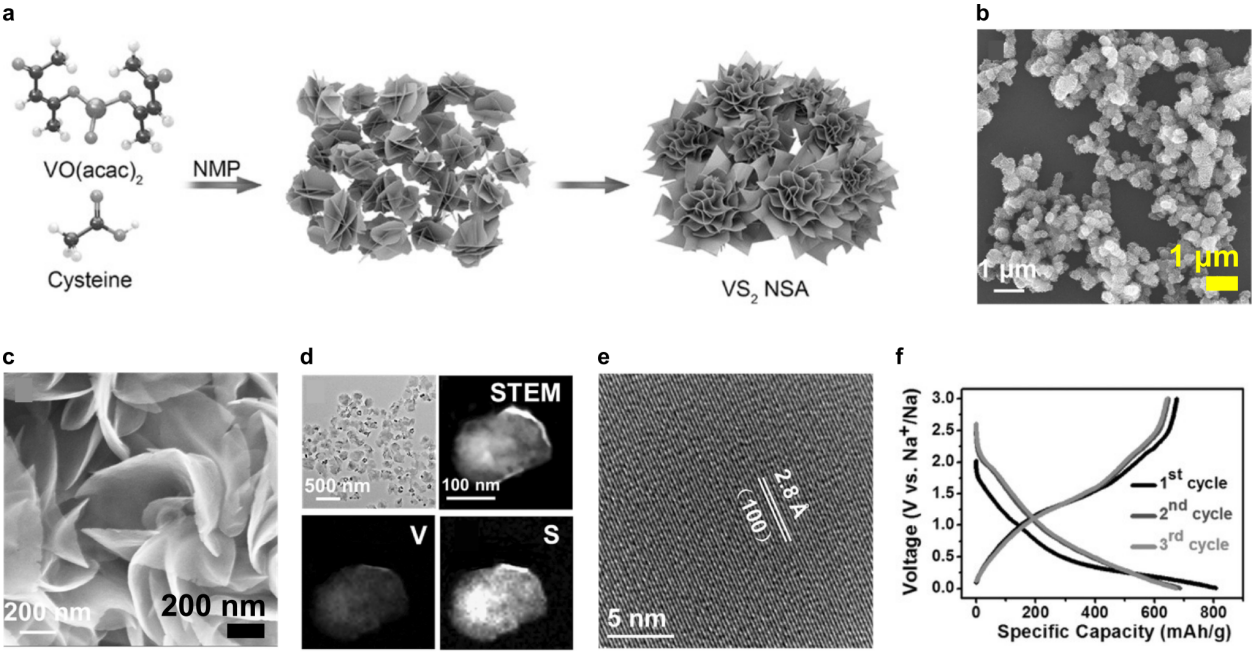

Figure 2.12: *(a) Schematics of VS_2 NSA synthesis. (b,c) SEM. (d) STEM with corresponding mappings. (e) TEM image of VS_2 NSA. (f) GCD of 1^{st}, 2^{nd}, and 3^{rd} cycles at $100\,mA\,g^{-1}$. Reprinted with permission from Ref.[41]. Copyright 2017, Wiley-VCH Verlag GmbH & Co. KGaA, Weinheim*

KIBs, which was corroborated by Bie et al. in[81].

There is very scarce literature on the performance of TMDs with tungsten in their formula as anodes in KIB systems. Wu et al. presented a study that revelated an unexpected intercalation-dominated process in WS_2 as KIB anode, a process not typical of the previous reports involving K^+ storage in layered sulfide-based TMDs[82]. Electrodes were synthesized using 2H-WS_2 bulk and exfoliated commercial powders as received. Compared to other layered TMDs for KIBs reported – where a conversion reaction prevails – in 2H-WS_2 as KIB anode intercalation dominates the K^+ storage process. The authors present a thorough explanation by presenting diffractograms and Raman spectra of cells at different charge and discharge states[82].

Considering the larger K^+ radius, which has implications in volume expansion upon intercalation of K^+, Wang and co-workers presented a solution that comprised a carbon matrix, acting as a buffer; providing, additionally, improved electronic conductivity to the electrode and safeguarding $MoSe_2$[83]. The material reported as "pistachio shuck-like" $MoSe_2$/C

core/shell nanostructure (PMC), presented by figure 2.13(a,b), exhibited $MoSe_2$ interlayer spacing of 0.85 nm, as shown by Figure 2.13(b,c). The structure of PMC may provide a better packing density, which may, therefore, enable faster kinetics. Tested in potassium half-cell configuration, the first cycle charge/discharge capacities were, 402 and 635 $mA\,h\,g^{-1}$, respectively, with Coulombic efficiency of 63.4%, which can be ascribed to solid electrolyte interphase (SEI) layer formation. Furthermore, after 100 cycles at 1 $A\,g^{-1}$, the material presented charge capacity of 322 $mA\,h\,g^{-1}$, as shown by figure 2.13(d,e). Authors assigned the optimized electrochemical performance of PMC due to carbon coated PMC surface and greater interlayer spacing, which allows K^+ transmission and mitigates the volume expansion.

Similarly, Ge and co-workers reported a carbon-coated 2H-$MoSe_2$ anode material and potassium bis(fluoro-slufonyl)imide (KFSI) as electrolyte[84]. The composite material was synthesized via solvothermal method, which employed glucose as carbon feedstock, annealed, and subsequently cast on copper form in 80% weight fraction active material. The half-cell with 1 M bis(fluoro-slufonyl)imide (KFSI)/ethyl methyl carbonate (EMC) as electrolyte presented initial discharge capacity of 376.4 $mA\,h\,g^{-1}$ and Coulombic efficiency of 79.9%. For second cycle, the values of charge and discharge capacities were, respectively, 278.3 and 256.1 $mA\,h\,g^{-1}$ at 100 $mA\,g^{-1}$. Regarding cycling performance, the material presented reasonable stability up to 300 cycles.

Furthermore, regarding selenide based TMD, in a theoretical study, Shen and co-workers reported the potential of 1T-$NiSe_2$ phase as anode for KIB. Authors conclude from such study that features such as small bandgap (0.54 eV), diffusion barrier (0.05 eV) and high capacity (247 $mA\,h\,g^{-1}$) demonstrate the potential of 1T-$NiSe_2$ as anode material for KIB[85].

Yang and co-workers[86] studied potassium-ion storage for ultrathin nanosheets of VSe_2 – the metallic member of TMD family, and which possesses a graphene-like structure, and their result is presented in Figure 2.14(a). The key for studying such species for K^+ storage lies in the fact that VSe_2 interlayer distance is 6.11 Å as depicted by Figure 2.14(b). Therefore, it can allow diffusion for the larger alkali metals without considerable structural distortion. The single-crystalline metallic graphene-like VSe_2 material was synthesized by a one-step colloidal method. As presented in Figure 2.14(d, e), with regard to electrochemical

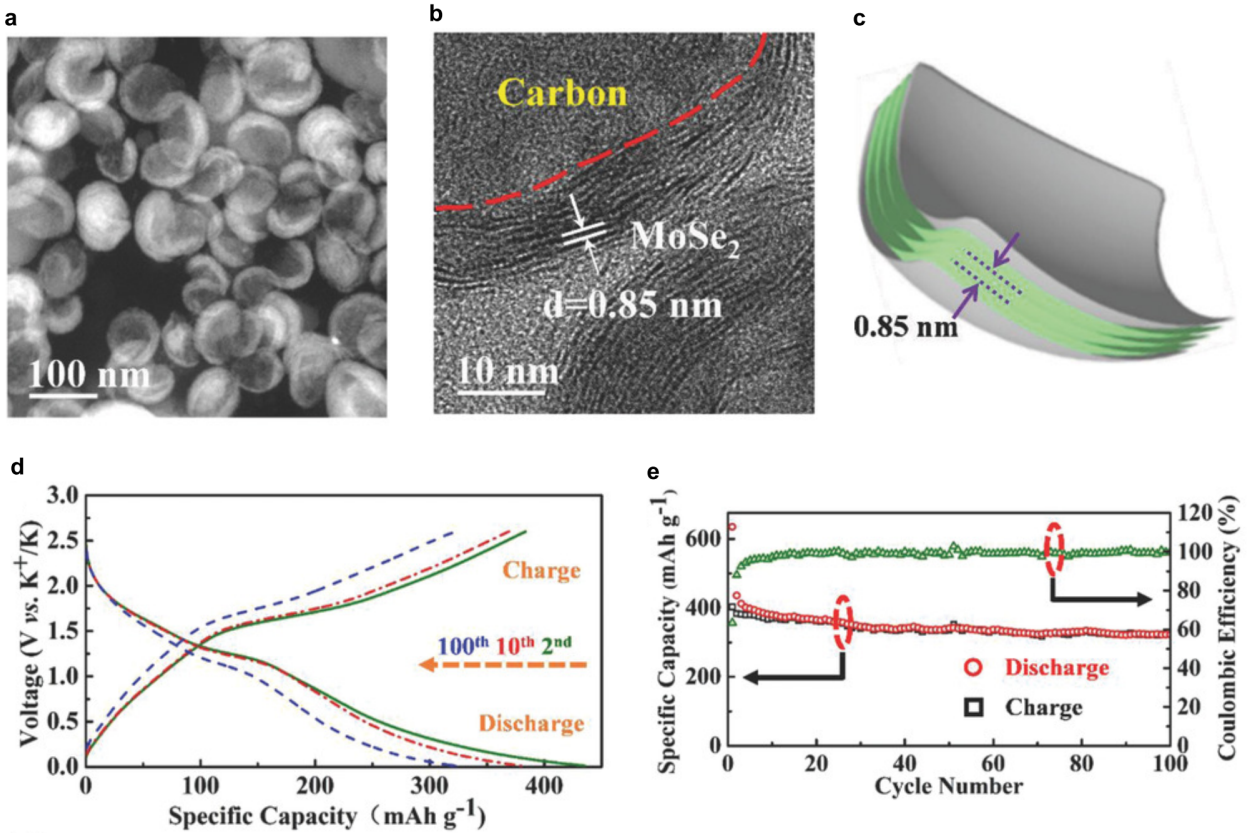

Figure 2.13: *(a) HAADF-STEM of PMC; (b) PMC HRTEM image showing the expanded interlayer spacing, and (c) illustration of $MoSe_2$ interlayer spacing; (d) 2nd, 10th, and 100th charge/discharge profiles at 200 mA g^{-1}; and (e) corresponding charge/discharge of PMC at 200 mA g^{-1}. Reprinted with permission from*[83]*. Copyright (2018) John Wiley & Sons.*

performance, in its first cycle, the specific values of charge and discharge capacities were, respectively 366 and 530 mA h g^{-1}. Furthermore, after 200 cycles of charge and discharge at a current density of 200 mA g^{-1}, the specific charge capacity value was 335 mA h g^{-1}; thus, corresponding to 95.1% of first cycle charge capacity. Authors concluded from this study that the electrochemical performance achieved was due to VSe_2 nanosheets' large adsorption energy allied with low diffusion barrier[86].

Lastly, in addition to the fascinating chemistry, which is still being unveiled, and novel layered electrode materials, potassium does not form alloys with aluminum. Thus, for anode electrodes the use of copper as current collector is not required. As reported by Vaalma, considering that copper prices are more volatile in the market than aluminum, this may represent a competitive aspect driving down costs for large scale production of KIB cells[87].

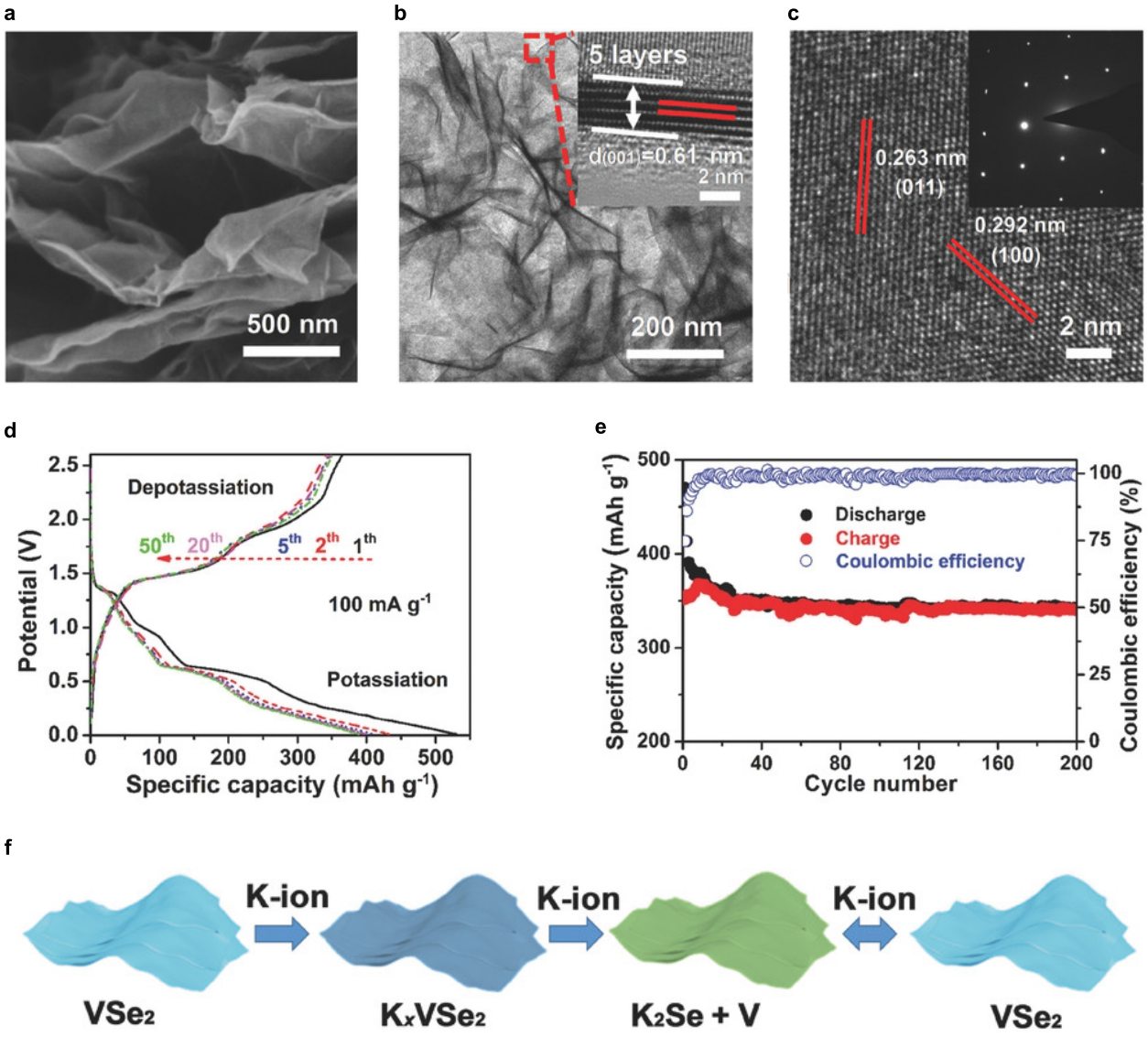

Figure 2.14: *Ultrathin layered VSe_2 nanosheets morphologies: (a) SEM, and (b)TEM with interlayer spacing in the inset. (c) SAED pattern of ultrathin layered VSe_2 nanosheets material. (d) Charge/discharge voltage profiles at* $100\,\mathrm{mA\,g^{-1}}$. *(e) Cycling performance and Coulombic efficiency at* $200\,\mathrm{mA\,g^{-1}}$. *Reprinted with permission from*[86]. *Copyright (2018) John Wiley & Sons.*

Lastly, experience has shown that although Li and Na share common properties as alkali metals, simply transferring the insights acquired from LIB chemistry to KIB does not always apply. As a result, ponderation on chemistry, electronic, and mechanical properties of KIB electrode materials is required.

2.4 Electrochemical characterization

2.5 Definition and assessment of (specific) capacity

As a key parameter to assess batteries, the concept of capacity can sometimes be confusing. According to the definition, battery capacity is given in units of A h, which is also known as the Charge. Based on the definition of Kirchev[88], battery capacity is the electric Charge collected during its charging cycle; maintained when the circuit is open; and supplied to the load when on its discharge cycle[88]. Analogously, the derivative of charge over time is the current[10], i.e.

$$I_t = \frac{dC}{dt} \tag{2.3}$$

Where, in equation 2.3, C is the Charge (A h), I_t is the current (A), and t is the time (h). It is worth noting that in the literature current is not used by itself, but with relation to the active mass of electrode (m_{active}). Consequently, it results in the following unit: (A g^{-1}). Additionally, the cell is tested under galvanostatic conditions, which means controlled Current (current is held constant, while the Time required to reach a specified voltage limit is measured)[12]. Thus, rearranging terms in equation 2.3 and integrating both sides results in the relation below.

$$C = \int \left(\frac{I_t}{m_{active}} \right) dt \tag{2.4}$$

Since the term Current divided by the active mass of the electrode is a constant value – because of galvanostatic condition – it results in

$$C = \left(\frac{I_t}{m_{active}} \right) \int dt \tag{2.5}$$

Hence, the charge or discharge capacity is calculated by integrating the current and time while the cell voltage range is set in the battery tester software.

2.5.1 Electrochemical impedance spectroscopy

Electrochemical impedance spectroscopy is a frequency domain technique to evaluate an ESS upon application of a small sinusoidal perturbation – commonly $\Delta E \approx 10\,mV$ – superimposed on an fixed D.C voltage[89;90]. As a technique based on generalized linear system theory (LST), it obeys the superposition principle, as shown by Figure 2.15, which illustrates the small Voltage amplitude signal applied (red line) and the desired linear region (blue line).

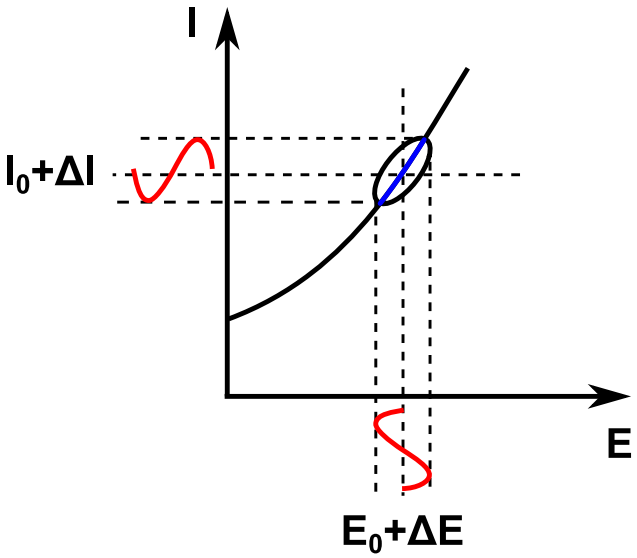

Figure 2.15: *Illustration of the principle of EIS.*

Considering the input Voltage signal in figure 2.15 is given by equation 2.6.

$$E(t) = E_0 + \Delta E\ \sin(\omega t) \tag{2.6}$$

Where in equation 2.6, E is the voltage, E_0 is the fixed D.C. voltage, ΔE is the amplitude of the sinusoidal signal, ω the angular frequency given by 2π times the frequency, and t the time. For a system that is purely resistive – i.e., voltage and current in phase – upon application of the potential presented by equation 2.6, the obtained current response can be expressed as follows.

$$I(t) = I_0 + \Delta I\ \sin(\omega t) \tag{2.7}$$

Yet for a system that is not purely resistive, upon application of the potential presented by equation 2.6, the current response will have a phase angle, φ.

$$I(t) = I_0 + \Delta I \, \sin(\omega t + \varphi) \tag{2.8}$$

Readers can see that only time-domain analysis has been presented up to this moment. By employing phasors, one can use algebraic expressions in frequency-domain; thus, avoiding having to solve differential equations characteristic of time-domain circuits. Equations 2.9 and 2.10 show in phasorial form how current ($\dot{I}$) and voltage ($\dot{E}$) can be written for a purely resistive load (R), respectively.

$$\dot{I} = \frac{\dot{E}}{R} = \frac{E^{j\,0}}{R} = \frac{E}{R} \tag{2.9}$$

And,

$$\dot{E} = \dot{I}\, R \tag{2.10}$$

Where in equation 2.9, $j = \sqrt{-1}$. Now, for a circuit that has either capacitive (C) or inductive (L) elements, the term resistance (R) should not be used. Instead, the term impedance ($\dot{Z}$) should be used. The impedance of a capacitive load in the time domain is given by:

$$Z(t) = \frac{E(t)}{I(t)} = \frac{E_0 + \Delta E \, \sin(\omega t)}{I_0 + \Delta I \, \sin(\omega t + \varphi)} \tag{2.11}$$

Where, from equation 2.11 one can confirm that handling equations in the time-domain can be an arduous task. On the other hand, the impedance of a load whose current and voltage in frequency-domain is given by equations 2.9 and 2.10 yields,

$$\dot{Z} = \frac{\dot{E}}{\dot{I}} = \frac{E}{I^{j\,\varphi}} = Z\, e^{-j\,\varphi} \tag{2.12}$$

It is important to highlight that the impedance ($\dot{Z}$) of a purely capacitive element is

calculated based upon the capacitive reactance, as presented below:

$$\dot{Z} = \frac{1}{C\,(j\,\omega)} \tag{2.13}$$

Where in equation 2.13, C is the parameter related to the element capacitance[91]. Moreover, the inverse of the impedance (Z) is known as admittance (Y), and it is presented as follows.

$$Y = \frac{1}{Z} \tag{2.14}$$

It is worth noting that the concepts presented above are used as presented in electric circuits. However, for electrochemical systems, some adjustments to these equations are required. For example the universal element used to simulate the equivalent circuit that also takes into account dispersion effects that deviate the ideal capacitive behavior of an electrochemical system is known as constant phase element (CPE), and is presented in equation 2.15[91].

$$Z_{CPE} = \frac{1}{Y_0\,(j\omega)^n} \tag{2.15}$$

Where in equation (2.15), Y_0 is admittance and $0 < n < 1$ determines whether the element more capacitive (n closer to 1), or more resistive (n closer to 0). Particularly for $n = 1/2$, the element is known as "*Warburg*" (W) and is extensively employed in equivalent circuit, as presented in figure 2.16. The Warburg element corresponds to a semi-infinite linear diffusion whose mass transfer impedance has identical real ($|Re(\dot{(}Z)|$) and complex parts ($|Im(\dot{(}Z)|$)[91]. In other words, let the angle between the linear segment with the real axis in figure 4.10(a) – known as phase angle – be φ. For the case where ($|Im(\dot{(}Z)|$) = ($|Re(\dot{(}Z)|$), this leads to

$$\tan(\varphi) = \tan\left(\frac{\Delta\,(|Im(\dot{(}Z)|)}{\Delta\,(|Re(\dot{(}Z)|)}\right) = 1 \tag{2.16}$$

Which from equation 2.16 yields $|\varphi|$ =45°. In the chapter 4 of this thesis, a discussion

regarding the use of Warburg element in EIS equivalent circuits is presented.

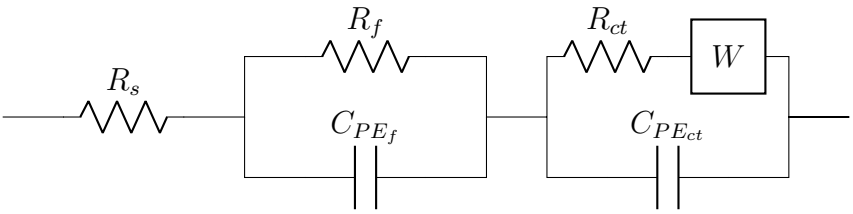

Figure 2.16: *Equivalent circuit for EIS fitting employed for results presented in Table 4.3. The Warburg element (W) is in series with* R_{ct} [74;92].

2.5.2 Galvanostatic Intermittent Titration Technique

GITT is a technique used to acquire thermodynamics and kinetic parameters of an electrochemical system under consideration[93]. The basis of this technique lies in applying successive current pulses, of positive and negative polarities, followed by a relaxation time, i.e., periods in which no current is applied.

As shown in figure 2.17, during the application of a positive current pulse of duration τ, initially the cell potential increases proportionally to IR value, where R is the value of the equivalent resistance and I is the constant current value. Subsequently, the potential starts to increase more gradually in order to maintain the concentration gradient. After the current pulse is interrupted, the potential again drops rapidly and then decreases at a slower pace until the equilibrium in the electrode is reached, and so the open circuit potential (OCP). In other words, GITT is a technique that measures the transient voltage change (ΔE_t) upon application of a current pulse (I_P). From the curves obtained parameters such as the chemical diffusion coefficient (D^{GITT}) can be calculated, as presented by equation 2.17.

$$D^{GITT} = \frac{4}{\pi\,\tau}\left(\frac{m_B\,V_M}{M_B\,S}\right)^2\left(\frac{\Delta E_S}{\Delta E_t}\right) \tag{2.17}$$

Where in equation 2.17, τ is the constant current pulse duration, m_B, V_M, and M_B are the mass, molar volume, and molar mass of the electrode material, respectively; S is the area of the electrolyte-electrolyte interface; lastly, ΔE_S and ΔE_t are the steady-state potential

change and the potential change, respectively.

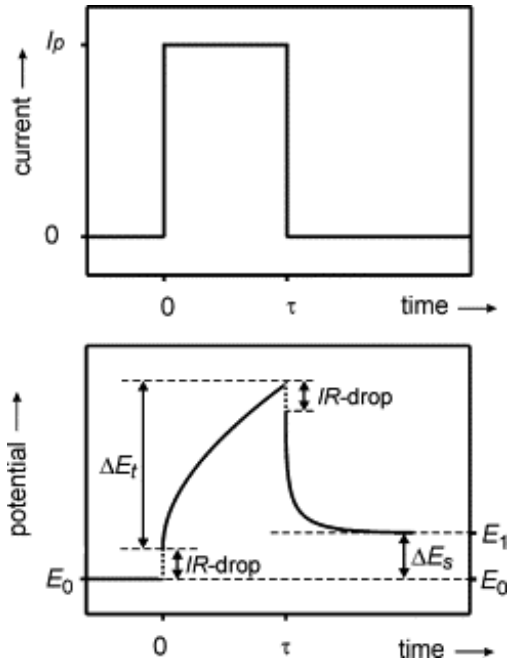

Figure 2.17: *Upper figure: single step positive polarity current pulse. Lower figure: potential response upon application of current pulse with parameters highlighted*[93]. *Copyright 2004 Elsevier Ltd. All rights reserved.*

2.6 Transition metal dichalcogenides

In the 1920s, Linus Pauling first reported a class of layered materials known as TMDs with generalized formula MX_2, where M corresponds to a transition metal (from groups 4 to 10) and X stands for a chalcogen species, i.e., S, Se, Te[94]. Arising from this general formula, more than 60 TMDs are known to exist, among which at least two-thirds present a layered structure, thereby presenting various chemistries, mechanical and electronic properties, as well as polymorphism[95].

As the major focus of this thesis, TMD crystals of group 6 present layered morphology with one transition metal in a sandwiched-like structure with two chalcogen atoms highlighted in figure 2.18. The transition metal in the structure crystallizes so that the coordination is generally trigonal prismatic or octahedral. Depending on the arrangement of transition metal and chalcogen atoms, one of these two coordination is thermodynamically preferential[96]. As

such, TMDs are a family of compounds that exhibit a diversity of structures and crystallographic, e.g., hexagonal 2H-MoS_2 , 2H-WS_2 (space group $P6_3/mmc$), octahedral 1T-MoS_2 (space group $P\bar{3}m1$), or the orthorhombic tellurides $MoTe_2$ and WTe_2 (space group $Pmn2_1$); thus, providing a spectrum of anisotropy in electronic properties e.g., the superconducting $NbSe_2$ and $PdTe_2$, and semiconducting 2H-MoS_2, 2H-WS_2, and HfS_2[97]. It is also important to highlight that TMD band gaps can be doped rather efficiently for various functionalities such as catalysis and optical applications[98].

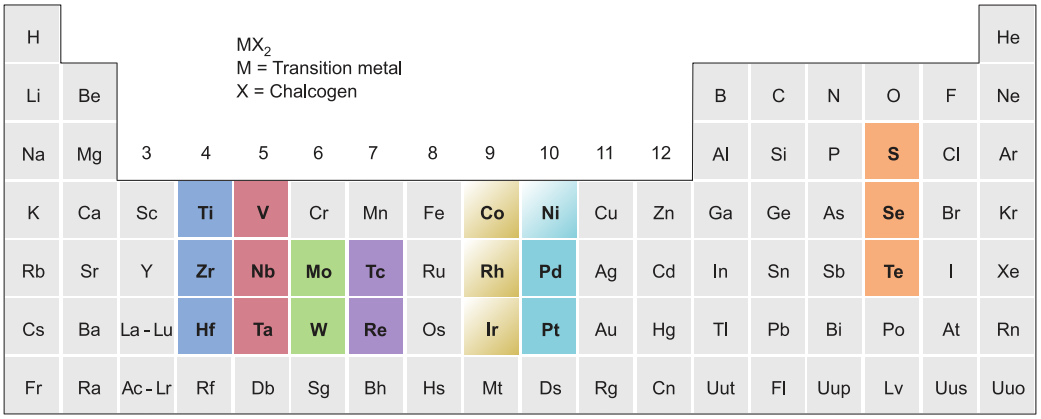

Figure 2.18: *General formula of TMDs and periodic table illustrating the elements that are known to crystallize in layered structures. Atoms Co, Rh, Ir, and Ni are partially highlighted as some species form layered TMD structures. Copyright 2013, Nature Publishing Group, a division of Macmillan Publishers Limited. All Rights Reserved*[97].

Owing to TMDs crystal structure anisotropy, massive research efforts are currently put into modification in interlayer interactions and phase engineering to allow additional tuning of TMDs electronic properties[99;100]. This can be illustrated by 1T-MoS_2, whose electronic conductivity is 1×10^7 times higher than the most stable thermodynamic and semiconducting phase 2H-MoS_2[101]. Hence, TMDs are candidates for flexible electronics, photodetectors, nano-electrochemical systems (NEMS), and ESS[36;102;103].

About ESS, exfoliated TMDs nanosheets may provide exciting features such as high theoretical energy density, high surface area, larger interlayer spacing, which allows accommodation of several alkali-ion metals, e.g., Li^+, Na^+, K^+. Moreover, structural stability – nanosheets are weakly held together by van der Waals forces and therefore may accommodate phase changes better than bulk crystals – and a greater degree of interaction with

electrolyte interface may considerably reduce the path for ions to access the host material. A more detailed discussion on synthesis techniques is presented in section 2.7.

Among the various types of electrochemical ESS currently being explored by researchers (e.g., metal-ion rechargeable batteries and supercapacitors), selecting suitable positive and negative electrodes is important. Mainly because established electrode materials for lithium-ion batteries may not be suitable for other alkali metal-ion batteries. This can be illustrated by graphite, which presents lithium theoretical capacity of $372\,\mathrm{mA\,h\,g^{-1}}$; notwithstanding it shows negligible capacity towards Na^+, as discussed in section 2.2[74;104]

Graphite is a layered material with widespread utilization in commercial LIBs. Reasons for its utilization are the safety, low cost, electronic conductivity, high reversibility lithium capacity, and low electrochemical potential to Li/Li^+[105;106]. Nevertheless, Li^+ storage in graphite relies on intercalation, process that yields the transfer of one electron per transition metal for alkali metal ions (figure 2.19(a)). More than a decade ago, Armand and Tarascon highlighted that the energy density of commercial LIB was only a factor of 5 greater than lead-acid batteries, and according to Moore's law, this is not a good indicative[107].

One feasible strategy for developing materials that can store more energy is the use of conversion electrode materials, which are illustrated in figure 2.19(b). Conversion-type reactions are advantageous because they can transfer up to 6 electrons; therefore, yielding higher specific capacity and ultimately higher energy density. It is also worth noting that due to a higher transfer of electrons, alloying-type reactions are also object of intense research, yet they were not studied and are not discussed in detail in this thesis[108].

The study of TMDs as electrodes for rechargeable batteries has revealed several species that rely on conversion and alloying type reactions[66]. Importantly, the occurrence of these reactions can be controlled as they are potential-dependent. For instance, MoS_2 shows intercalation Li^+ storage up to $1.5\,\mathrm{V}$ *versus* Li/Li^+. However, going to potentials lower than $0.05\,\mathrm{V}$ a total of four electrons are transferred; thus, indicating that intercalation is not the only mechanism involved[109]. Moreover, recently Ma and co-authors reported that SnS_2 as SIB electrode material shows intercalation, conversion, and alloying stages depending on the potential applied[110].

For clarification, in the literature sometimes the terms "*intercalation*" and "*insertion*" are used interchangeably. However, these terms have different meanings. Intercalation indicates a layered host material that attains its structural integrity upon letting ions in and out of its structure, e.g., graphite. On the other hand, insertion comprehends a more broad scope, as it may refer to processes where structural rearrangement may occur, such as the alloying reaction of Li^+ with Si or Sn, where major structural changes happen[111;112].

Overall, because of these exciting, tunable, and favorable structural and electronic properties, TMDs have drawn a great deal of research interest as electrode materials for ESS applications. In this thesis, MoS_2, a sulfide-based TMD, is studied in chapter 3 due to its great potential and availability for the future of ESS; also, WTe_2, a telluride-based TMD, is also studied because its fascinating properties, which are presented in chapters 4 and 5.

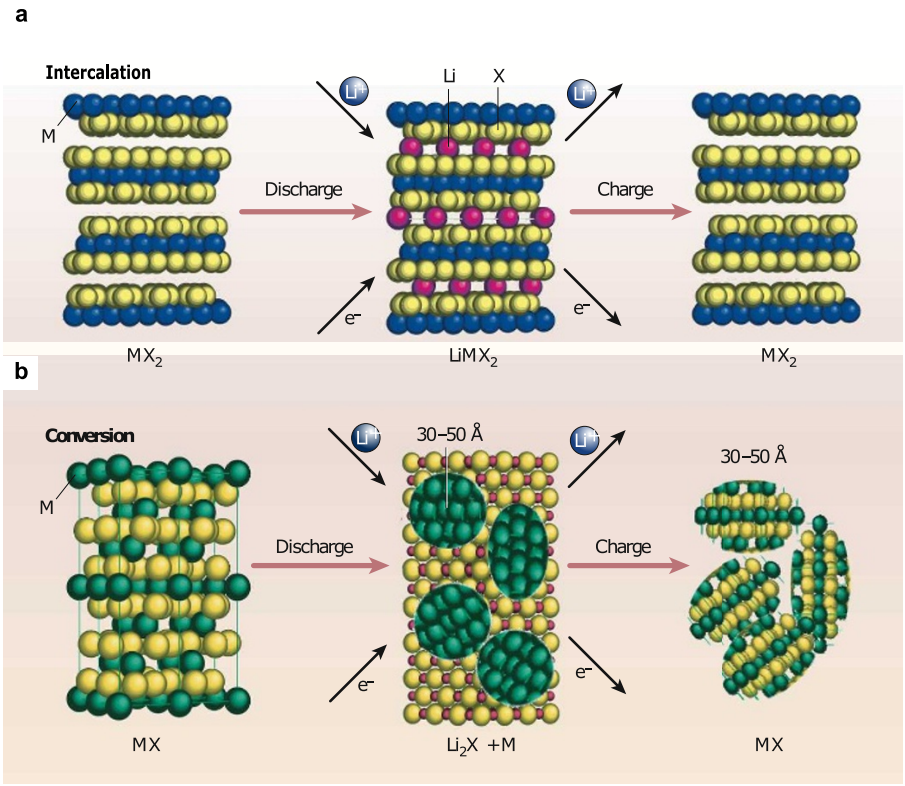

Figure 2.19: *Schematic of charge storage mechanisms, (a) intercalation, and (b) conversion reaction. Copyright 2008, Nature Publishing Group*[107].

2.7 Synthesis techniques of TMDs[4]

One of the most essential and attractive properties of TMDs are their considerable anisotropy in properties, especially in electronic and crystallographic structure[97]. Therefore, synthesis methods aim to modulate these properties towards the application's needs by tweaking the interlayer spacing and microstructural morphology. It should also be noted that the synthesis approaches should be high yield and scalable while being as less energy-intensive and inexpensive as possible.

Synthesis techniques of TMDs are generally classified as "top-down" or "bottom-up". As the name suggests, top-down techniques usually start with the bulk precursor material and achieve the desired morphology. This contrasts with bottom-up processes, where atomic layers are built up in a "block-by-block" or "layer-by-layer" fashion.

Generally, top-down approaches are relatively cost-effective and yield a somewhat more significant quantity of material that can be suitably used for scalable electrochemical energy storage applications[118]. Mechanical exfoliation is one of the prevalent techniques that has been used; it has the advantage of providing high-quality and very pure single layers, although they are not commonly scalable and, as a result, are suitable for very fundamental studies. In this case, mechanical exfoliation per se indicates just the peeling off individual TMD layers, similar to graphene[17], using tools such as scotch-tape as illustrated by figure 2.20(a). To summarize, bottom-up techniques can be used to study the fundamental behavior of TMDs e.g., transport and semiconducting properties[119].

On the other hand, the liquid solvent-based exfoliation technique is one of the most popular and important methods for providing a considerable amount of material for electrochemical energy storage applications (figure 2.20(b))[120]. Organic solvents – e.g., hexane, isopropanol – are commonly used, and sometimes a pre-intercalating ion such as Li^+ (n butyl-lithium is a common source in such cases) is used to induce and facilitate the exfoliation process[101]. Ambrosi et al. studied the performance of MoS_2 exfoliated by different lithiated

[4]Reprinted with permission from Soares, Davi Marcelo, Santanu Mukherjee, and Gurpreet Singh. "TMDs beyond MoS_2 for electrochemical energy storage." *Chemistry - A European Journal* (2020). Wiley-VCH Verlag GmbH & Co. KGaA, Weinheim.

organic molecules, e.g., methyllithium, n-butyllithium, and tert-butyllithium. They were able to demonstrate more efficient exfoliation when n-butyllithium and the tert-butyllithium were employed as exfoliating agents[121]. Similarly, Xiao et al. demonstrated the use of polyethylene oxide (PEO) for enhancing the interlayer spacing of MoS_2 for electrochemical storage applications. Results showed a 95% coulombic efficiency and good capacity retention in the process[122]. Further, Bang et al. used a 1-methyl-2-pyrrolidone (NMP) solution to exfoliate MoS_2 to be used as anodes in SIB systems. They were able to obtain first cycle sodiation and desodiation capacities of 254 and 164 $mA\,h\,g^{-1}$, respectively, and a coulombic efficiency of 97%[123].

As another route to prepare electrode materials for EES, very strong acids ("*superacids*") such as chlorosulfonic acid (HSO_3Cl) have been used to exfoliate TMDs, as demonstrated by Singh et al.[124]. This approach showed the advantage of forming stable dispersions and not restacking easily; restacking of nanosheets is a recurrent problem in these layered compounds[124]. Using this technique, the authors were able to obtain a capacity of 230 $mA\,h\,g^{-1}$ and a coulombic efficiency of 99% in a Na-ion half-cell configuration[124].

Bottom-up approaches find limited applications for electrochemical energy storage applications, primarily due to the energy-intensive nature of the processes themselves and the rather low yields obtained. CVD (figure 2.20(c)), physical vapor deposition (PVD) (figure 2.20(d)) are some of the bottom-up techniques used, in general, to synthesize layered TMDs[125]. In the literature, the study of thin films of TMDs prepared by bottom-up technique for application in electrochemical energy storage devices is rather scarce. Yet in their pioneering work, Xu et al. synthesized WS_2 "platelet like" thin-films by a sputtering process as anodes in SIB systems and a reversible volumetric capacity of 554 $mAhcm^{-3}$ at 50 $mA\,g^{-1}$ was obtained[126].

In perspective, the synthesis of TMDs remain a very active and developing research area. As restacking and aggregation of the exfoliated TMD sheets constitute a significant area of concern, the emphasis currently lies in synthesizing uniform, exfoliated nanosheets of TMDs able to perform reliably for long term cycling[128]. An important paradigm shift lies in moving away from using pure TMDs, and instead, synthesize heterostructures, which are alternate

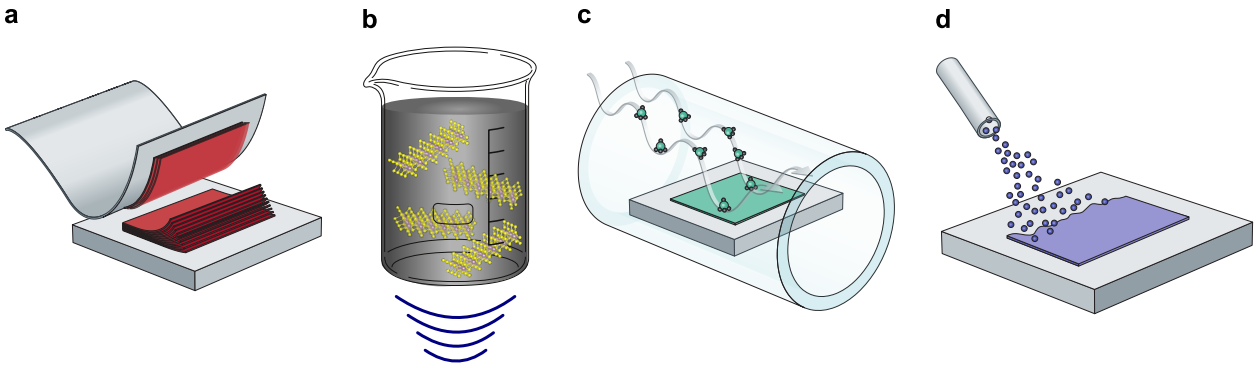

Figure 2.20: *Schematics of some synthesis methods of 2D materials. (a) Mechanical exfoliation. (b) Liquid exfoliation by ultrasonication. (c) CVD. (d) PVD. Copyright 2017, Macmillan Publishers Limited*[127].

atomically thin layers of different TMDs or TMDs interspersed with graphene[19;129].

Heterostructures provide the advantage of using the constituent parts' benefits and maintaining the overall layered morphology[19]. Synthesis of TMD based nanocomposites and using functionalized moieties to enhance the electrochemical activity are other novel avenues that are currently being considered[130].

2.8 Polymer derived ceramics

Polymer derived ceramics (PDCs) are ceramic materials synthesized from a liquid polymeric ceramic precursor with active research in fields ranging from aerospace to biotechnology[131]. Reasons for this growing interest in PDCs is conventional ceramics are brittle materials and difficult to machine. Nevertheless, PDCs provide the advantage of polymer synthesis, which can be tweaked to result in a ceramic material whose production may employ state-of-the-art techniques – such as AM – and with properties of interest. Therefore, as unique ceramic materials, PDCs exhibit high oxidation and thermal shock resistance, electronic conductivity, negligible creep-behavior, and lower synthesis temperatures when compared with conventional ceramics[132].

In 1960, Ainger and Herbert firstly reported the synthesis of non-oxide ceramics synthesis from molecular precursor[133]. Subsequently, Verbeek and co-inventors developed ceramic fibers from the following pre-ceramic polymers: polysilazanes, polysiloxanes, and polycar-

boxilanes. Based on this discovery, patents on behalf of Bayer AG were filed[134;135]. At the same period, in Japan, Yajima reported the production and high stability under high temperature of SiC ceramic fibers, synthesized by thermolysis of polycarbosilanes[136;137]. Ever since, the synthesis of ceramic networks upon low-temperature pyrolysis of pre-ceramic polymers is intensively studied.

As materials that can be employed in the synthesis of nano- and micro-ceramics composites with complex shapes – as presented by figure 2.21(a-g) – polymer derived ceramic (PDC) usually exhibit facile synthesis routes. Although the synthesis processes still involve thermal treatments, these commonly require lower temperatures – and energy – compared to traditional ceramics synthesis[131].

2.8.1 Types of pre-ceramic polymers

As previously discussed, one of the advantages of PDC is the fact that elements in the composition of pre-ceramic polymer (initial stage) may remain in the ceramic structure after the pyrolysis; therefore, enabling macroscopic physical properties to be present in the final material application. Arising from this remarkable aspect, a wide range of possibilities is possible by applying the diversity of polymer chemical design, i.e., changing the functional and/or organic groups of the monomer, in order to develop new ceramic materials with complex shapes. The simplified representation of the preceramic polymer emphasized in this thesis (organosilicon polymer) is depicted in figure 2.22.

Where, in figure 2.22, X and R_n represent, respectively, the group of the polymer backbone and the functional or organic groups that can be attached to the repeat unit. It is worth noting that the organic groups (R_n) selection plays a role with respect to solubility, chemical, and thermal stability of the polymer, as well as its electronic, optical, and rheological properties[132]. Similarly, by changing the X group new classes of organosilicon polymers can be obtained, for instance, X = Si originates a poly(organosilanes), X = O poly(organosiloxanes), and X = CH_2 poly(organocarbosilanes). Figure 2.23 introduces a chart originated from the simplified formula shown in figure 2.22[139].

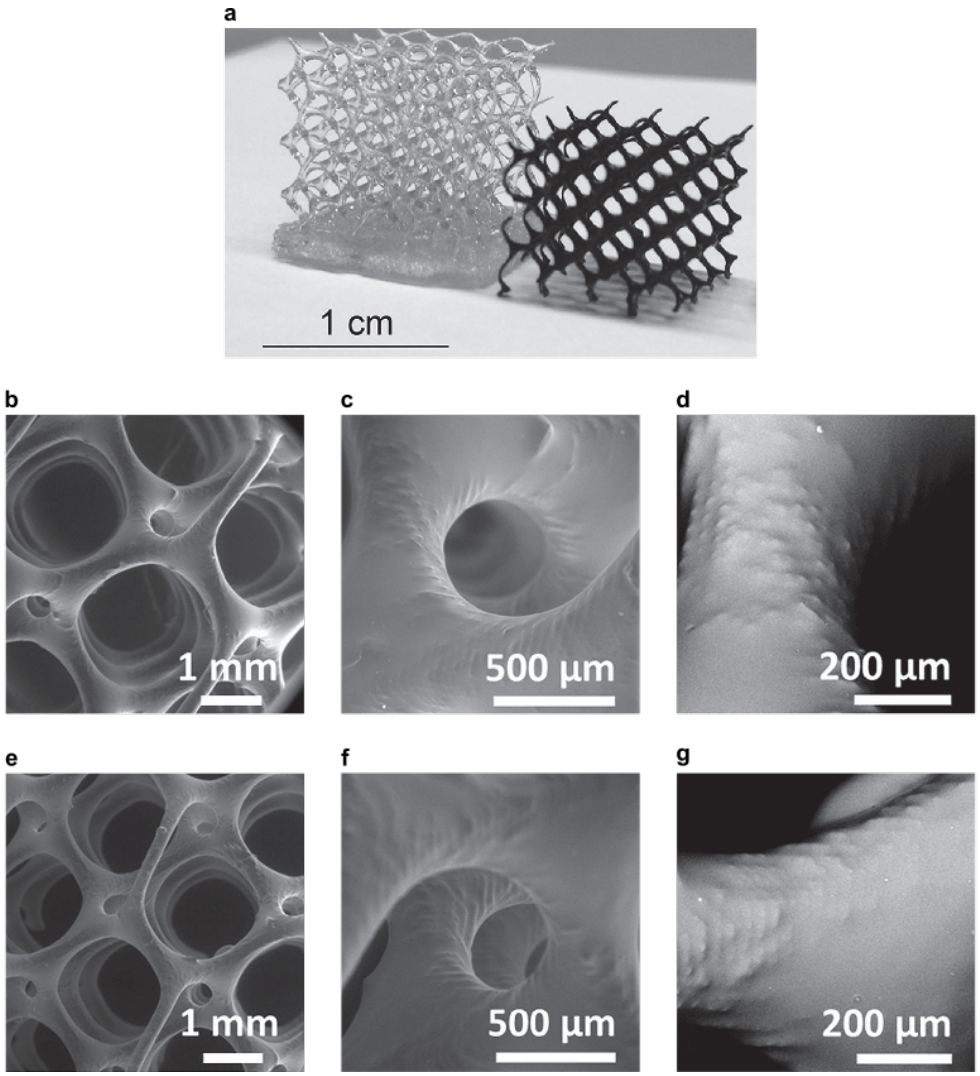

Figure 2.21: *(a) Cross-linked 3D structure made by additive manufacturing (left-hand side) and the same 3D structure after pyrolysis (right-hand side). SEM images of 3D structure after (b-d) cross-linking, (e-g) pyrolysis at* 1000 °C. *Copyright 2015, WILEY-VCH Verlag GmbH & Co. KGaA, Weinheim*[138].

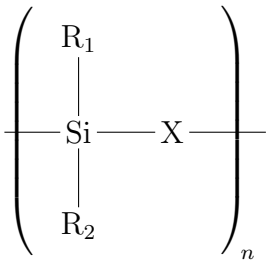

Figure 2.22: *Simplified representation of organosilicon pre-ceramic polymer.*

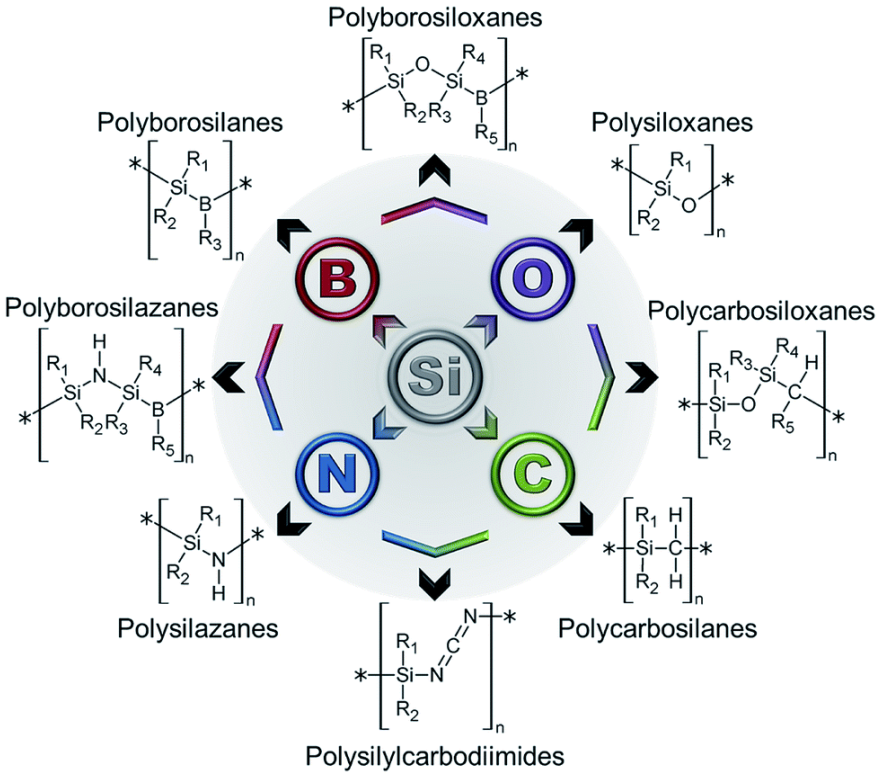

Figure 2.23: *Classes of Si-based polymer as precursors for ceramics. Reproduced with permission from The Royal Society of Chemistry (2018)*[140].

In this thesis, emphasis is given to silicon oxycarbide (SiOC) ceramics, which when in polymer form corresponds to Si bonded to $X = \mathrm{O}$ atoms in figure 2.22 (poly(organosiloxane))[131;141].

2.8.2 From polymer to ceramics: the transformation process

Up to this point, pre-ceramic polymer structures have been presented, and the advantages of using polymer synthesis approaches to produce PDC emphasized. In this section, a brief discussion of the mechanisms of conversion from polymers to ceramics is presented.

The conversion process from polymer to ceramic happens in two main steps, namely, cross-linking of the polymers at low temperatures (100 - 400 °C) – a process that provides infusible organic and inorganic networks – and ceramization process at temperatures also considered low (compared to the traditional sintering methods of ceramic materials) from 1000 to 1400 °C.

During the cross-linking process, the precursors are converted into inorganic and organic

materials, which assures a higher cross-link yield by avoiding higher losses of low molecular mass components from the pre-ceramic polymer. Furthermore, the infusible organic and inorganic networks mentioned preventing the materials from melting during ceramization process – second step – in which a higher temperature is involved[139].

Subsequently, the pyrolysis step is conducted at a higher temperature under inert conditions. In this last step, thermal decomposition of volatile compounds, oligomers, and hydrocarbons occurs, so the amorphous ceramic can be obtained. Moreover, depending on the pyrolysis parameters, higher retention of hydrogen can be achieved (at $\approx 800\,^{\circ}\mathrm{C}$), or nano-sized crystalline phases in the ceramic (at $\approx 1400\,^{\circ}\mathrm{C}$). Lastly, depending upon pre-ceramic polymer composition, free sp^2 carbon domains are present in the ceramic material; this property is relevant for energy storage applications because of higher electronic conductivity.

2.9 Considerations upon crystal structures of TMDs

Bulk TMDs present ordered layers stacked by van der Waals interactions — similar to graphene[142]. One remarkable feature exhibited by TMDs is the polymorphism, in other words, atoms may exhibit different intermolecular arrangement while maintaining the same formula MX_2. Thus, the coordination of the transition metal atom of TMDs plays an important role because TMDs may crystalize in the following phases: 3R, 2H, 1H, 1T, $1T'$, and Td, where the number in the nomenclature accounts for the number of X-M-X arrangements in the unit cell. For clarification, figure 2.24 illustrates the these phases[143].

The 3R phase corresponds to a lattice with rhombohedral (R) symmetry and trigonal prismatic metal coordination, where three sets of X-M-X layers per unit cell are found (figure 2.24(a,b)). Figure 2.24(b) illustrates the stacking sequence AbA CaC BcB – where upper- and lower-case letters represent the chalcogen and metal atoms, respectively[97].

Figure 2.24(c) shows the 1H and 2H phases, where metal coordination is trigonal prismatic with hexagonal symmetry (D_{3h} point group). Phase 2H presents stacking sequence AbA BaB (figure 2.24(d)), whereas phase 1H only shows AbA.

1T phase displays tetragonal symmetry (D_{3d} point group) with octahedral coordination of metal atoms (figure 2.24(f)). As presented by figure 2.24(g), the stacking sequence is AbC. Comparing phases 1H- or 2H- with the tetragonal symmetry phase, a shift of 60° in the chalcogen atoms in the arrangement X-M-X exists.

Although sometimes confused with 1T phase, figure 2.24(h,i) shows 1T′ phase, which is ascribed to a distorted octahedral metal coordination. Examples of TMDs that present 1T′ phases are telluride-based TMDs, e.g., $MoTe_2$ and WTe_2[144]. Likewise, phases 1T′ and Td are akin; nevertheless, they present centrosymmetric monoclinic and non-centrosymmetric orthorhombic unit cells, respectively. Figure 2.24(h-k) illustrates the small differences between them.

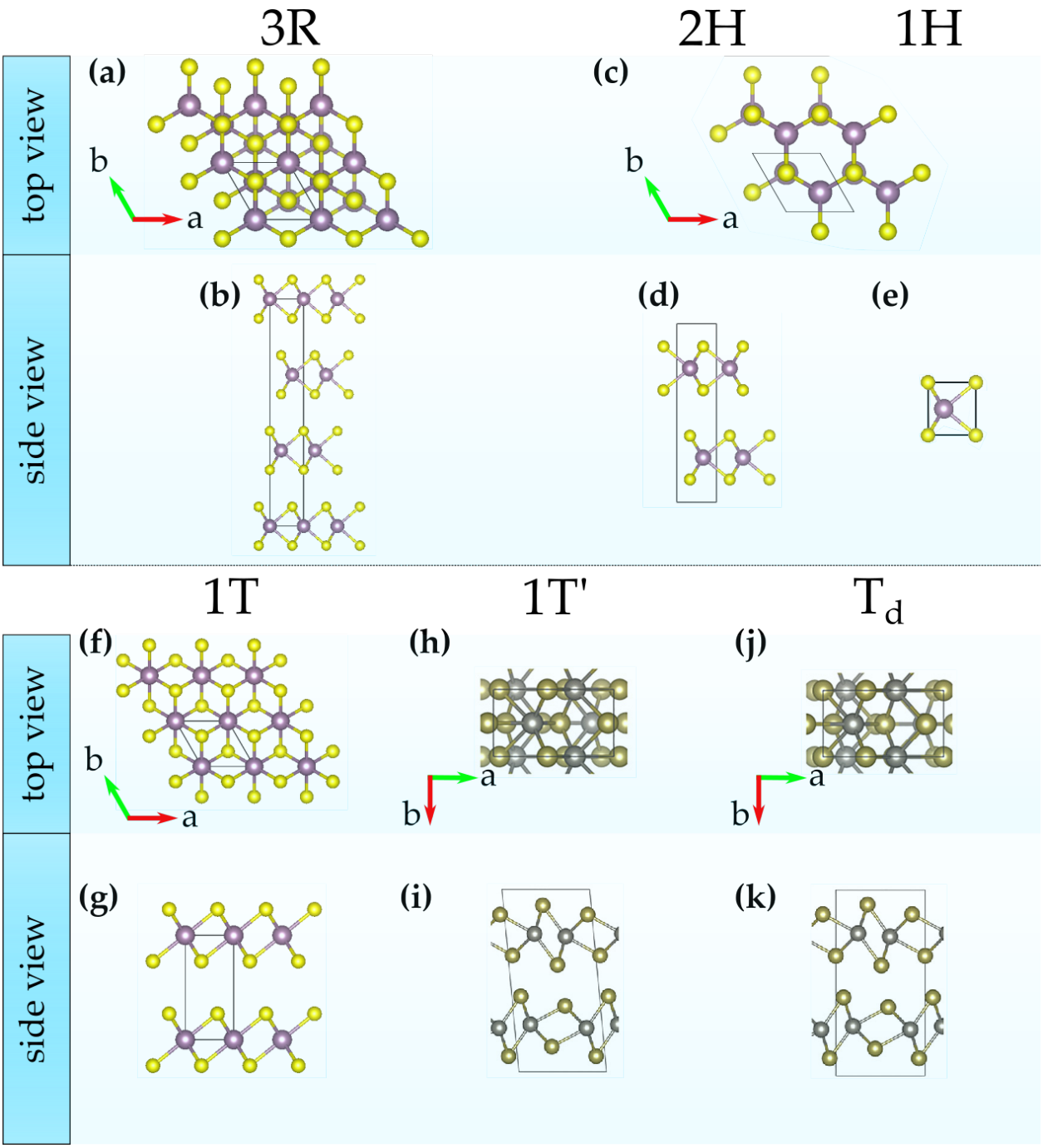

Figure 2.24: *Polytypes of MoS_2 crystals. (a,b), 3R. (c), 1H and 2H top view. (d), 2H. (e). 1H. (f,g) 1T. (h,i) 1T′. (j,k) Td.*

Table 2.1: *Performance of some TMDs as SIB applications.*

Materials	Electrolyte chemistry	Voltage range (V vs Na/Na^+)	Performance Specific capacity [mAh g-1] / number of cycles / current density [mAg-1]	Reference
graphite	1 M $NaPF_6$ in DEGDME	0.001 - 2.5	∼100 / 2500 / 500	[60]
graphene foam	1 M $NaPF_6$ in diglyme	0.01 - 2	∼120 / 8000 / 12000	[61]
WS2/rGO	1 m NaPF6 in EC / DMC (1:1)	0.01 - 3	∼200 / 200 / 1000	[62]
FeS_2 nanoparticles	1 M $NaPF_6$ in DEGDME	0 - 3	∼320 / 30 / 100	[63]
FeS_2 quantum-dots / functionalized graphene-sheet (QDs/FGS)	1 M $NaSO_3CF_3$ in DEGDME	0 - 3	552 / 100 / 500	[64]
FeS_2@C	1 M $NaSO_3CF_3$ in DEGDME	0.01 - 2.8	173 / 2000 / 4460	[65]
SnS_2/graphene	1 M $NaClO_4$ in EC/DEC (1:1)	0.01–2.5	∼610 / 300 / 200	[66]
SnS_2 nanosheets	1 M $NaClO_4$ in PC with 5% FEC	0.005 - 3.0	647 / 50 / 100	[67]
SnS_2/NGS	1 M $NaClO_4$ in PC with 2% fluoroethylene carbonate (FEC)	0.01 - 3.0	453 / 200 / 500	[68]
TiS_2	1 M $NaPF_6$ in dimethoxyethane (DME)	0.3 - 3.0	740 / 9000 / 20000	[69]
$MoSe_2$	1 M $NaClO_4$ in EC/DMC (1:1) with 5% FEC	0.01 - 3.0	459 / 90 / 200	[70]
$MoTe_2$	1 M $NaClO_4$ in EC/PC (1:1) with 3% FEC	0.1 - 2.5	270 / 200 / 1000	[71]
WTe_2 nanorods	1 M $NaClO_4$ in EC/DMC (1:1) with 5% FEC	0.01 - 3.0	221 / 100 / 100	[72]

Table 2.2: *Relevant properties of Li, Na, and K for rechargeable ion battery applications*[27;75;76].

	Li^+	Na^+	K^+
relative atomic mass	6.94	22.99	39.10
mass-to-electron ratio	6.94	22.99	39.10
Shannon's ionic radii (Å)	0.76	1.02	1.38
density (g/cm^3)	0.535	0.968	0.856
E^0 vs. SHE in aqueous media (V)	-3.04	-2.71	-2.93
melting point (°C)	180.54	97.72	63.38
theoretical capacity of metal electrode ($mA\,h\,g^{-1}$)	3861	1166	685
theoretical capacity of metal electrode (mAh/cm^3)	2062	1131	591
theoretical capacity of $ACoO_2$ ($mA\,h\,g^{-1}$)	274	235	206
theoretical capacity of $ACoO_2$ (mAh/cm^3)	1378	1193	-
molar conductivity of $AClO_4$ in PC/ (Scm^2/mol)	6.54	7.16	-
desolvation energy in PC ($kJ\,mol^{-1}$)	218	157.3	119.2
Cost (US$ ton^{-1})	165,000	200	1,000

Table 2.3: *Crystal and electronic properties of group IV layered TMDs. Properties correspond to bulk material unless otherwise specified.*

Group	M	X	Crystal lattice	Electromagnetic properties	Bandgap (eV)	a (Å)	c (Å)	Reference
VI	Mo	S	2H	semiconducting, diamagnetic	0.788 - 1.679	3.2	12.3	
VI	Mo	S	3R	semiconducting, diamagnetic	0.788 - 1.679	3.2	18.4	113;114
VI	Mo	Se	2H	semiconducting, diamagnetic	0.852 - 1.393	3.3	12.9	114;115
VI	Mo	Se	3R	semiconducting, diamagnetic	0.852 - 1.393	3.3	19.4	114;115
VI	Mo	Te	2H - α	semimetallic, diamagnetic	1.04 (monolayer)	3.5	14.0	114;115
VI	Mo	Te	2H - β	semimetallic, diamagnetic	1.04 (monolayer)	3.7	13.8	114;115
VI	W	S	2H	semiconducting, diamagnetic	0.917 - 1.636	3.2	12.3	114
VI	W	S	3R	semiconducting, diamagnetic	0.917 - 1.636	3.2	18.5	114
VI	W	Te	Td	semimetallic	$\rho \approx 1 \times 10^{-3}\,\Omega\,\mathrm{cm}$	3.4	14.0	96;97;116
graphene (C)			H	semiconducting	0	2.4	6.9	117

Chapter 3

SiOC functionalization of 2H-MoS_2[1]

3.1 Preview

The development of feasible, scalable, and environmentally safe electrode materials that provide stable cycling performance is critical for the success of beyond lithium rechargeable batteries and supercapacitors. Concerning the SIB anodes constituting of TMDs such as molybdenum disulfide (MoS_2), poor cycle stability and fast capacity degradation, due to low electronic conductivity and dissolution of chemical species in the electrolyte, hinders the use of these promising layered materials as SIB anodes. Herein we report chemical functionalization in MoS_2 nanosheets with polymer-derived silicon oxycarbide or SiOC to preserve MoS_2 from dissolution in the SIB organic electrolyte, without compromising its role in sodiation and desodiation processes. Our results suggest that a MoS_2-SiOC composite electrode is effective in bringing improved cycle stability to sodium-ion cycling over pristine MoS_2 even after 100 cycles

[1]Reprinted with permission from Soares, Davi Marcelo, and Gurpreet Singh. "SiOC functionalization of MoS_2 as a means to improve stability as sodium-ion battery anode." *Nanotechnology* 31.14 (2020): 145403. IOP Publishing. All rights reserved.

3.2 Introduction

Layered TMDs materials have suitable properties as anode materials for SIB[19;97;145]. This class of materials presents lamellar structure – similarly to graphite – allowing insertion of sodium ions. Moreover, as introduced in section 2.6, TMDs present ≈ 40 layered chemical species; thereby, showing versatile chemistries and unique electrical, chemical, mechanical and thermal properties. Among these species, the Mo-based TMDs, e.g., MoS_2, $MoSe_2$, $MoTe_2$ possesses sandwich-like structure, which, on the one hand, allows sodiation and desodiation among its layers. On the other hand, sodiation may induce structural transformations in TMDs; hence, showing electrochemically undesired repercussions[145;146]. These structural changes may occur during initial cycles causing large first cycle loss and irreversible capacity decay. These undesirable outcomes can be assigned to SEI layer formation, side reactions, and dissolution of sulfides in the electrolyte by virtue of lower reversibility of metal sulfide chemical reactions, for instance[147–150]. In addition, volume changes during insertion and extraction of sodium ions and mechanical stresses associated with such process may culminate in lower electronic conductivity of electrode with subsequent sluggish cycling stability[151–153].

In an initial study to address the drawback of cyclability in TMDs, three species of Mo-based TMDs were tested in long-term cycling as SIB half-cells at 200 mA g^{-1} to evaluate which would be worth studying. Results of this electrochemical test are presented in figure 3.1.

From the data presented by figure 3.1, one can clearly see the highest specific charge capacity of MoS_2 electrode. Nevertheless, a continuous capacity decay exists during cycling. Arising from the availability, polymorphism, and historic of use in battery electrodes[15], MoS_2 was chosen as material of interest towards a composite material with higher stability upon cycling.

Thus, here our goal is to present one alternative to address the cyclability drawback of MoS_2 in SIB. Thus, we report a facile and safe synthesis of MoS_2 and silicon oxycarbide (SiOC) composite.

As presented in section 2.8, PDCs are materials that can improve stability and mitigate high first cycle loss and sulfide dissolution in SIB MoS_2 anodes[150;154]. Due to its open

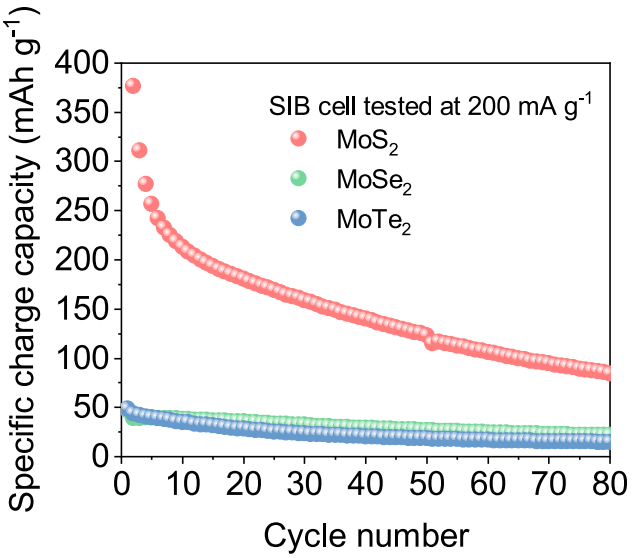

Figure 3.1: *Electrochemical performance of Mo-based TMDs in long-term cycling.*

polymer-like network and chemistry, SiOC is capable of decreasing capacity decay and suppressed regeneration of MoS_2 because, during the synthesis process, the pre-ceramic polymer molecules may diffuse in between MoS_2 nanosheets. Therefore, establishing an alternating structure of SiOC ceramics and MoS_2 upon pyrolysis, which – given the inherent nature of SiOC ceramic material – may furnish resistance to degradation and oxidation to the active material[131;155]. Accordingly, a thin layer of SiOC may effectively protect the active material without affecting its crystal structure or disrupting ion insertion/extraction during cycling.

It is worth noting that there are studies published reporting the electrochemical behavior of SiOC for Li^+ storage properties[156–158]. Nevertheless, there are not many published studies of SiOC as composite anodes for SIB, primarily because SiOC has negligible capacity toward Na^+. Moreover, to our best knowledge, this is the first report of MoS_2-SiOC composite as electrode material for SIBs. To summarize, this study reports a facile process for preserving MoS_2 from prominent capacity fading under cycling; therefore, mitigating the suppressed regeneration of MoS_2 by safeguarding this TMD species with SiOC.

3.3 Experimental

3.3.1 Material preparation

The simplified synthesis method of MoS_2 functionalized by polymer-derived SiOC ceramic is presented by figure 3.2, and in details as follows. Initially, MoS_2 technical grade and 1,3,5,7-tetravinyl-1,3,5,7-tetramethylcyclotetrasiloxane (TTCS) (purchased from Gelest), in which 1% wt. dicumyl peroxide (Sigma Aldrich, 98%) was added, were mixed until obtained a homogeneous mixture in several MoS_2:TTCS weight ratios, i.e., 1:1, and 1:4, and 1:10. Then, samples were placed in open-air oven at 160 °C for cross-link for 18 hours, and afterward pyrolyzed in argon atmosphere at 800 °C for 30 min. The latter is responsible for providing amorphous SiOC ceramic through decomposition of the polymer precursor above mentioned. Under these conditions, the polymeric precursor presented ceramic yield of ≈ 70%. Consequently, for samples of MoS_2:TTCS containing weight ratios 1:1, and 1:4, and 1:10, it resulted in yield values of ≈ 35%, 56%, and 63% of SiOC in MoS_2–SiOC composites, respectively. It is important to highlight that lower weight ratios of TTCS were also studied; nevertheless, no crosslinking of TTCS was achieved in these samples, i.e., the preceramic polymer did not change phase or solidify, even after several hours of heating. Reasons for this are presently unknown and could be the focus of future work.

Electrodes were prepared by mixing the active material – i.e., pristine MoS_2 or MoS_2–SiOC – (70 wt. %), carbon black as conducting agent (15 wt. %) (Alfa Aesar 99.9%), and polyvinylidene difluoride as a binder (15 wt. %) (Alfa Aesar). Few drops of 1-Methyl-2-pyrrolidinone (Sigma Aldrich) were added until a homogeneous mixture was obtained. Subsequently, a uniform thin film of ≈ 125 µm was cast on a 9 µm copper substrate through dr blade technique, and dried overnight in open-air oven at 80 °C for solvent removal. After dried, circular cells were punched for use as working electrodes in coin cell (CR2032 model) assembly. Cell assembly was performed in a high-precision argon atmosphere glove box with sodium metal (negative electrode) and stainless-steel spacers used. Additionally, a Celgard separator soaked in 1 M $NaClO_4$ (Alfa Aesar) in (1:1 v/v) EC:DMC (anhydrous,

99%, Sigma) was used to keep the cathode and anode electrodes apart. All chemicals were used without any further purification.

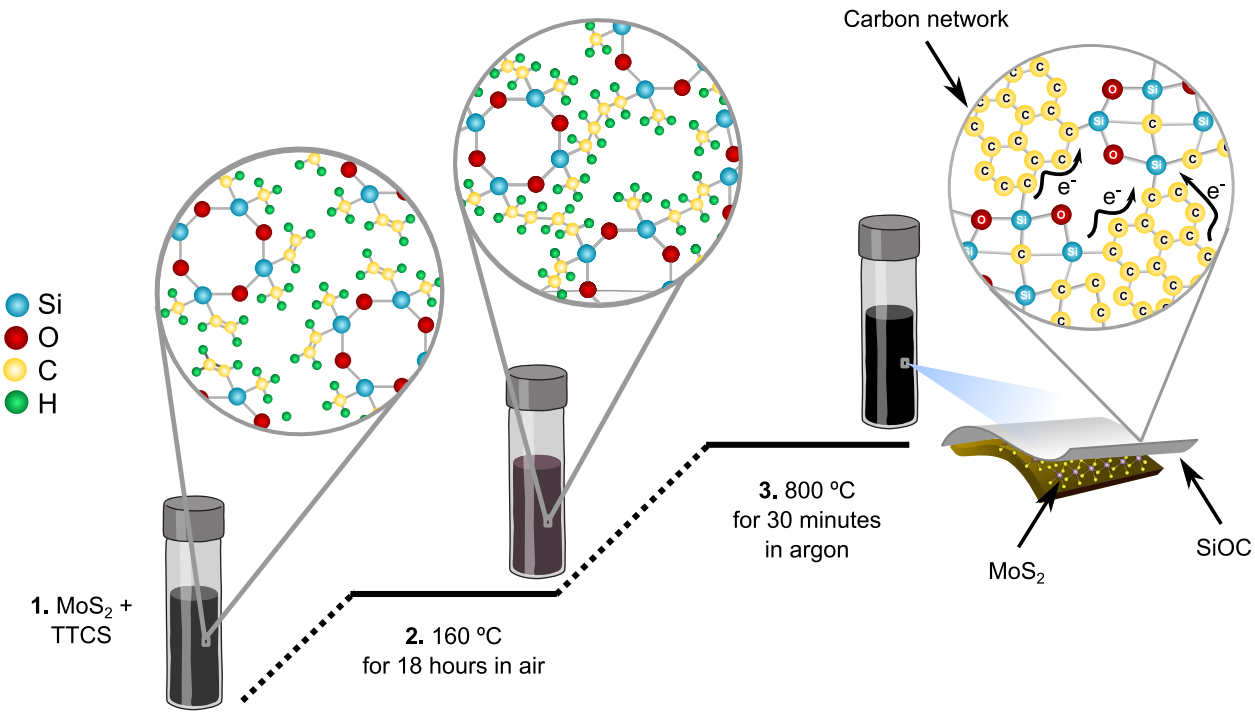

Figure 3.2: *Schematic of composite electrode (MoS_2-SiOC) preparation, including TTCS transformation into ceramics.*

3.4 Material characterization

Morphological analysis of materials were observed using Carl Zeiss EVO MA 10 SEM, Philips CM 100 TEM 100 kV, and high-resolution transmission electron microscope FEI Tecnai Osiris TEM 200 kV equipped with EDX spectrometer. Raman spectra were taken in HORIBA Jobin Yvon, HeNe laser wavelength 633 nm, and XPS in Thermo Scientific, monochromatic Al anode Kα (hν = 1486.6 eV) with spot size 400 µm. Also, for XPS, a surface etching was carried out by in-situ sputtering of argon ions with energy of 3 keV for 2 min. MoS_2 and MoS_2-SiOC structures were studied by X-ray diffractograms, which were taken in Rigaku Miniflex II Cu Kα (λ = 1.5406 Å). Lastly, half-cells were tested in Arbin BT2000 multi-channel battery tester and electrochemical station CHI660E of CH Instruments, Inc.

3.5 Results and discussion

From morphology analysis, SEM images of pristine MoS_2 and MoS_2–SiOC composite electrodes are presented, respectively, by figure 3.3(a,b), which depict particles with fairly similar morphology and particle size.

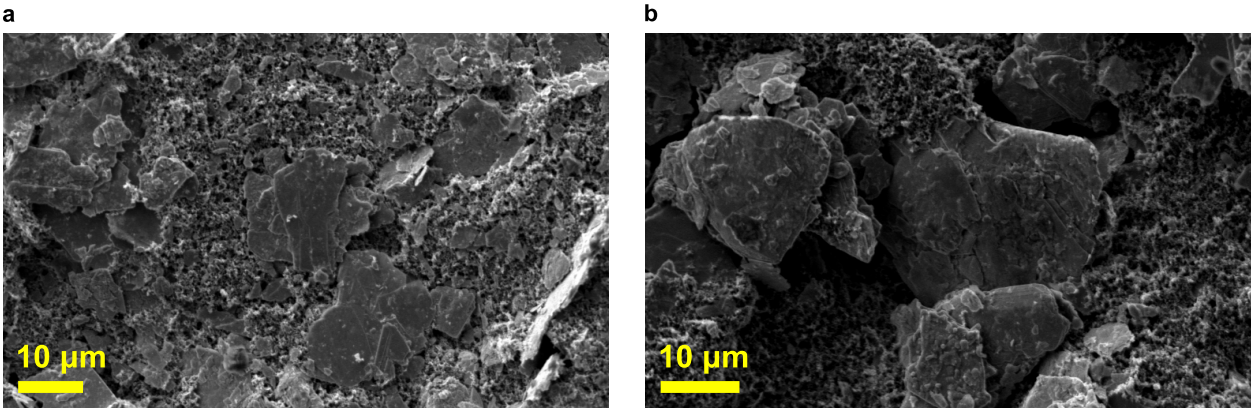

Figure 3.3: *SEM images of electrode materials cast on copper foil: (a) pristine MoS_2, and (b) MoS_2-SiOC.*

The layered structure of MoS_2 functionalized with SiOC is presented by figure 3.4(a), where thin sheets possessing hundreds of nanometers long can be identified. Additionally, from HRTEM image depicted by figure 3.4(b,c), no defects could be identified, which indicates that the functionalization did not affect the morphology nor crystallinity of MoS_2 nanosheets. Likewise, from figure 3.4(d)–(j) and table 3.1, given the nature of EDX analysis, the elemental mapping reveals very low atomic percentage of silicon, for instance, which indicates that SiOC may be deposited on the surface of MoS_2 nanosheets; thus, protecting its intact structure.

Table 3.1: *Composition data from EDX.*

Element	Atomic number	Series	Unn. C [wt. %]	Atomic C [at. %]
C	6	K-series	0.92	5.37
Si	14	K-series	0.58	1.45
S	16	K-series	14.3	31.39
Mo	12	L-series	84.21	61.8

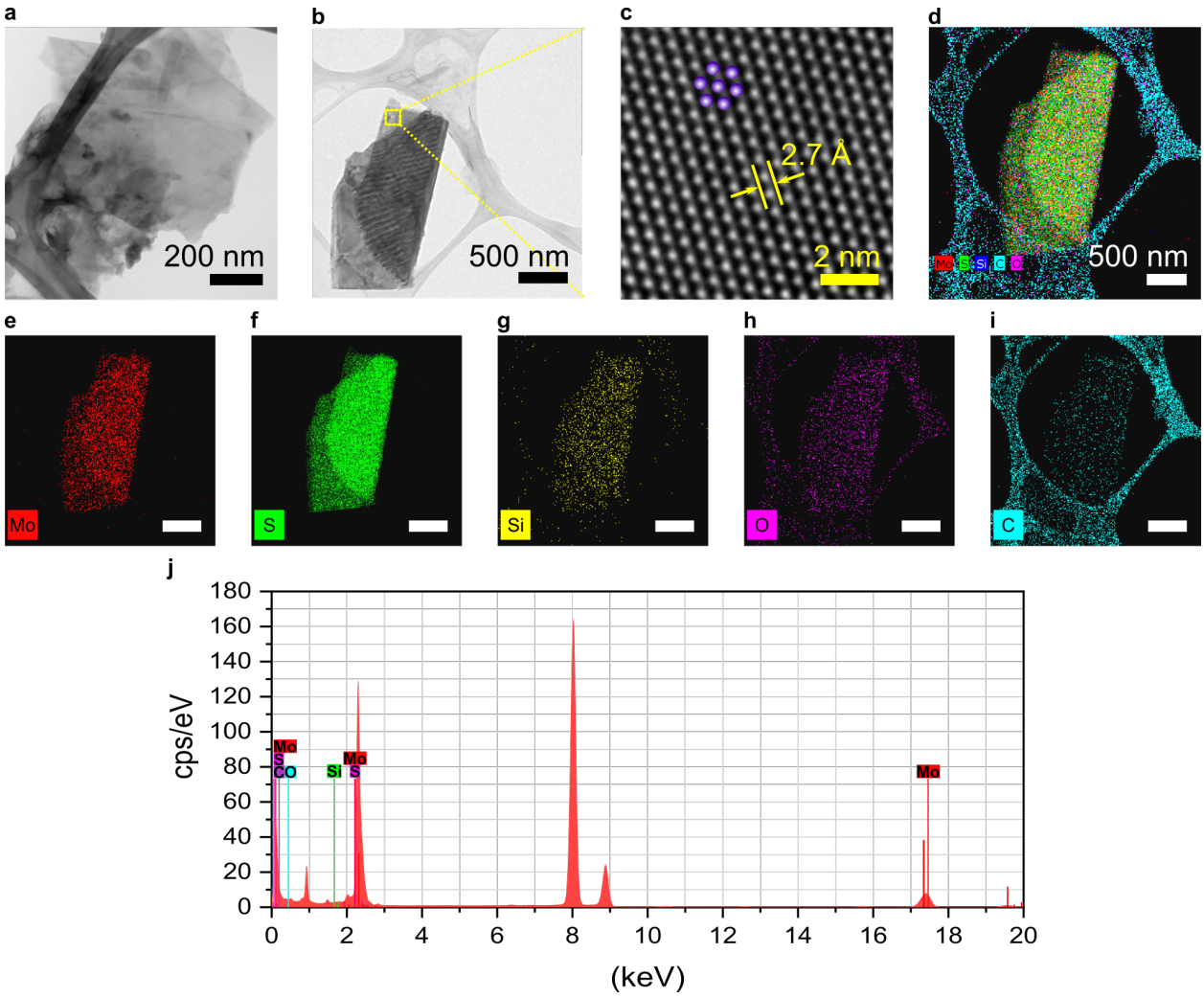

Figure 3.4: *(a) TEM image of MoS_2-SiOC composite, (b) HRTEM image of MoS_2-SiOC composite sheet, (c) annular dark-field STEM, (d) STEM image with elemental mapping of, (e) Mo, (f) S, (g) Si, (h) O, and (i) C. (Scale bar for (d)-(i) is* 500 nm*). (j) EDX spectrum of functionalized MoS_2-SiOC material.*

To further understand the functionalization, evaluate chemical species, chemical states and bonding XPS was conducted. Figure 3.5(a) shows the survey scan and reveals the main species in the composite material. In contrast to EDX, XPS peak analysis reveals a greater atomic percentage of silicon on MoS_2–SiOC – fact inherent of its surficial analysis. The detailed peak analysis is presented in table 3.2. The molybdenum spectrum – depicted by figure 3.5(b) – presents the lowest binding energy peak at 226.2 eV, which can be ascribed to sulfur 2s orbital; while the peak at 227.9 eV is assigned to $3\,d_{5/2}$ elemental molybdenum. The deconvolution of Mo 3d also reveals peaks assigned to $3\,d_{5/2}$ and $3\,d_{3/2}$ of MoS_2 at

228.8 eV and 232.8 eV, respectively[101;159–161]. The peak at 231.2 eV is assigned to Mo^{4+} state and presents a shift to metal state of ≈ 3.2 eV, in accordance with literature results[162]. Regarding sulfur species, figure 3.5(c) presents binding energy range presents four component peaks with orbitals $2\,p_{3/2}$ and $2\,p_{1/2}$ and spin coupled with chemical shift of $\Delta E = 1.2$ eV[163]. Thus, photoemission peaks at 161.7 eV and 162.9 eV are assigned to $2\,p_{3/2}$ basal sulfide ions S^{2-} and $2\,p_{1/2}$ to atomic sulfur, respectively[164–167]. Further, the peak at 163.5 eV was ascribed to elemental sulfur[164]. According to the silicon line (figure 3.5(d)), one can see that the facile functionalization with SiOC performed did not produce chemical bonding with neither Mo nor S atoms; therefore, maintaining the chemical structure of MoS_2 intact for its purpose. Moreover, as shown by microscopy images, SiOC acts as a physical protection for MoS_2 molecule, mitigating (poly)sulfide dissolution during sodiation and desodiation processes[168]. In fact, Si spectrum shows the most intense peak is attributed to Si – C bonds, at 101.7 eV; whilst the other is attributed to Si – O bonds[169–172]. In relation to carbon species, the peak at 284.4 eV – figure 3.5(e) – is assigned to C–C bonds, and peaks located at 283.6 eV and 286.1 eV are assigned to Si–C and C–O bonds, respectively[173–176]. Furthermore, the less intense peak at 288.8 eV is ascribed to O=C–O, which corroborates with lower intensity peak at 530.4 eV for O1s spectral line, which is presented by figure 3.5(f)[177–179]. Indeed, the higher intensity peak from the O 1 s spectrum reveals the presence of Si – O bonds[180].

Table 3.2: *XPS peak table of MoS_2-SiOC.*

Name	Start BE (eV)	Peak BE (eV)	End BE (eV)	Height CPS	FWHM (eV)	Atomic %
C1s	292.38	284.39	280.28	45353	1.86	40.63
Mo3d	236.48	228.12	226.38	30668.17	1.78	3.45
O1s	541.18	532.41	527.48	95625.56	1.7	30.23
S2p	168.48	162.07	159.18	10502.66	2.37	5.15
Si2p	108.08	102.76	97.98	19492.87	2.5	20.53

In addition, to comprehend the vibrational modes of pristine MoS_2 and functionalized material, Raman spectroscopy was performed. The pristine MoS_2 spectra, presented by figure 3.5(g), presents the three high intensity peaks located at $\approx$ 375, 400, and 440 cm^{-1}. The peak located at 375 cm^{-1} is assigned to in-plane active mode E^1_{2g} of bulk crystal[181];

the one located at $400\,cm^{-1}$ is an out-plane mode A_{1g} [182;183]; lastly, the peak located at $\approx 440\,cm^{-2}$ is ascribed to Mo−S vibration of reduced or Mo^{6+} oxysulfide species, which may be formed by exposing such samples to an oxidizing atmosphere [184;185]. Concerning the MoS_2-SiOC sample, in addition to the peaks seen in the pristine MoS_2 sample, there were peaks ascribed to SiOC, i.e., peaks at $\approx 1350\,cm^{-1}$ and $1590\,cm^{-1}$, which are attributed to bands D and G, respectively, characteristic of carbon materials. The D band – located at $1350\,cm^{-1}$ – is assigned to the sp^2 disordered carbon breathing modes. Additionally, a peak not very intense at $\approx 1500\,cm^{-1}$ is assigned to D″ band, which is characteristic of amorphous carbon present in the SiOC composite [132]. Finally, G band is ascribed to bond stretching of sp^2 carbon pairs [186;187]. It is also important to highlight that the presence of sp^2 carbon may provide higher electronic conductivity for the electrode; therefore, an also attractive property of SiOC, which may grant higher rate capability [82;188–190]. In addition, crystallite size of MoS_2 could be estimated from the resonant Raman spectroscopy. The ratio of the intensity of longitudinal acoustic mode – LA(M) – located at $\approx 228\,cm^{-1}$ to that of mode A_{1g}, for both materials, presents values lower than 0.1; therefore, indicating that the crystallite size of MoS_2 is much greater than 10 nm or even micro-crystalline domain size for MoS_2 species [191;192].

Concerning crystalline structure of the materials, as portrayed by figure 3.5(h), diffraction peaks indicate hexagonal crystal system space group $P6_3/mmc$, also reported in literature as 2H, once such structure has two MoS_2 layers per unit cell with trigonal prismatic coordination [193–196]. Again, the crystal and layered structure of MoS_2 were preserved after cross-link and pyrolysis procedures performed during SiOC synthesis; thereby, corroborating that the functionalization did not modify the structure of MoS_2. Just for comparison purposes, pristine MoS_2 was annealed in argon for 30 min at 800 °C (green diffractogram in figure 3.5(h)), where a new peak at $2\theta = 26°$ was observed. This new peak suggested that functionalization with SiOC suppresses the mentioned (unknown) phase to be formed in MoS_2 during pyrolysis step. Lastly, crystallite sizes of pristine and composite materials – $D_{(002)}$ – were calculated using Scherrer relation (equation 3.1). Domain sizes of MoS_2 and MoS_2-SiOC were estimated to be 46 nm and 45.1 nm, respectively.

$$D = \frac{\kappa\,\lambda}{\beta\,\cos\theta} \tag{3.1}$$

Where, in equation (3.1), D is the crystallite domain size, θ is a particular diffraction angle – given in radians – λ is the X-ray wavelength ($\lambda = 1.5406\,\text{Å}$), and κ is a numerical factor, also known as Scherrer constant. At present study, for the plane (002), κ was set to 0.76[197]. Yet, it is worth noting it can vary from 0.89 to 1.39.

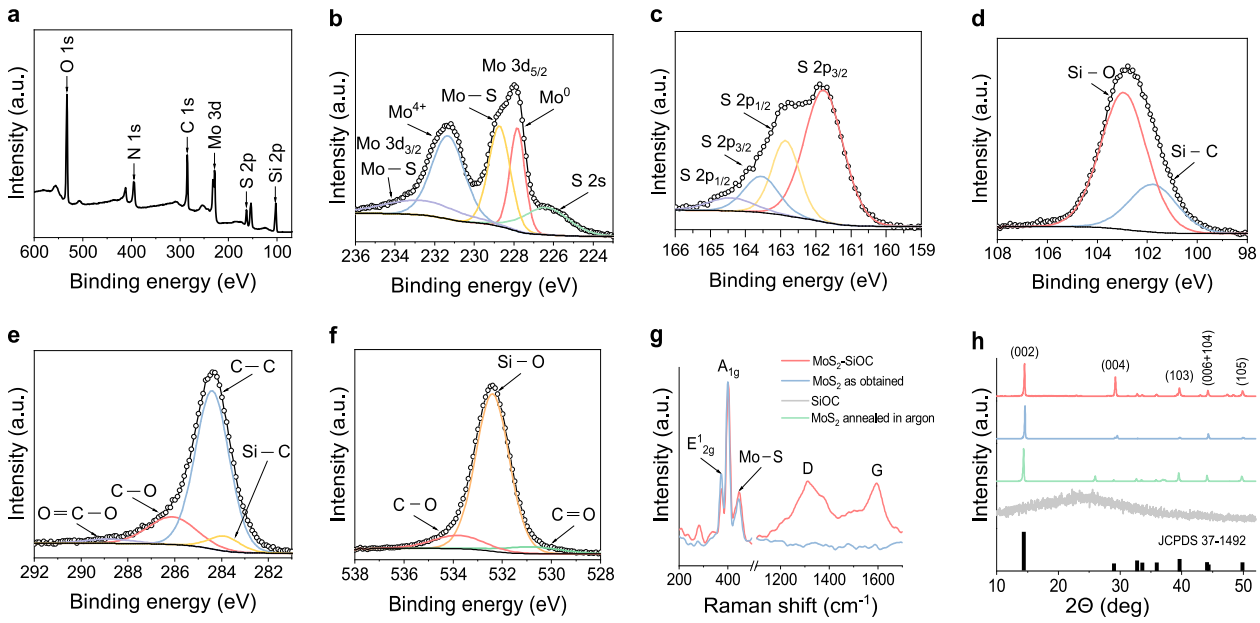

Figure 3.5: *(a) Survey scan of MoS_2-SiOC composite, and respective high-resolution spectra of (b) Mo 3d, (c) S 2p, (d) Si 2p, (e) C 1s, and (f) O 1s; (g) Raman spectra of pristine MoS_2 and functionalized MoS_2-SiOC material; (h) XRD diffractograms of MoS_2-SiOC (red), pristine MoS_2 (blue), pristine MoS_2 annealed in argon flow at* 800 °C *(green), and SiOC (gray).*

Electrochemical characterization of pristine MoS_2 and MoS_2-SiOC composite was carried out through galvanostatic half-cell configuration with reference to sodium metal. From figures 3.6(a), 3.6(b), and 3.7(a) it is possible to see at first discharge cycle the three plateaus, inherent of MoS_2 species previously reported in the literature[124;147].

The discharge cycle processes can be quantified in two main reactions, namely equations 3.2 and 3.3, which yield equation 3.4[198;199]. From figures 3.7(a), (b), reduction peaks at 0.8 V and 0.9 V can be ascribed to insertion of Na^+ into MoS_2 (equation 3.5), and Na_xMoS_2

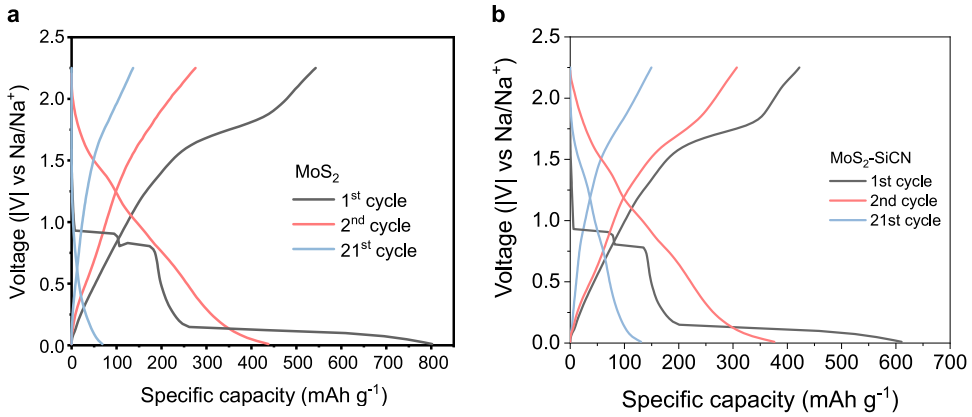

Figure 3.6: *Charge and discharge profiles of half-cell cycled between 0.01 and* 2.25 V *versus* Na/Na^+ *of (a) pristine* MoS_2*, and (b)*MoS_2*-SiCN.*

layers, respectively, as well as to irreversible formation of the SEI during the first cycle due to the greater value of dQ/dV depicted in figure 3.7(b) [124;200;201].

$$MoS_2 + y\,Na^+ + y\ e^- \longrightarrow Na_yMoS_2, \tag{3.2}$$

$$Na_yMoS_2 + (4-y)\,Na^+ + (4-y)\,e^- \longrightarrow 2Na_2S + Mo, \tag{3.3}$$

$$MoS_2 + 4\,Na^+ + 4\,e^- \longrightarrow 2\,Na_2S + Mo, \tag{3.4}$$

$$Na_xMoS_2 + (4-x)\,Na^+ \longrightarrow Mo + Na_xS \tag{3.5}$$

The prominent oxidation peak shown by figure 3.7(b) at first cycle at ≈ 1.7 V is assigned to extraction – or desodiation – of Na^+ from Na_2S/Mo of MoS_2, and Mo^0 oxidation to regenerate MoS_2 [200;202]. Importantly, one can see that for second cycle of figure 3.7(b), the peak at 1.7 V still presented such oxidation peak; in contrast to the differential capacity plot of pristine MoS_2, presented by figure 3.8(a). Considering that all cells were synthesized, assembled, and tested under the exact same conditions, SiOC prevented this reaction to happen entirely on the first cycle, in opposition to pristine MoS_2 electrode [203]; therefore,

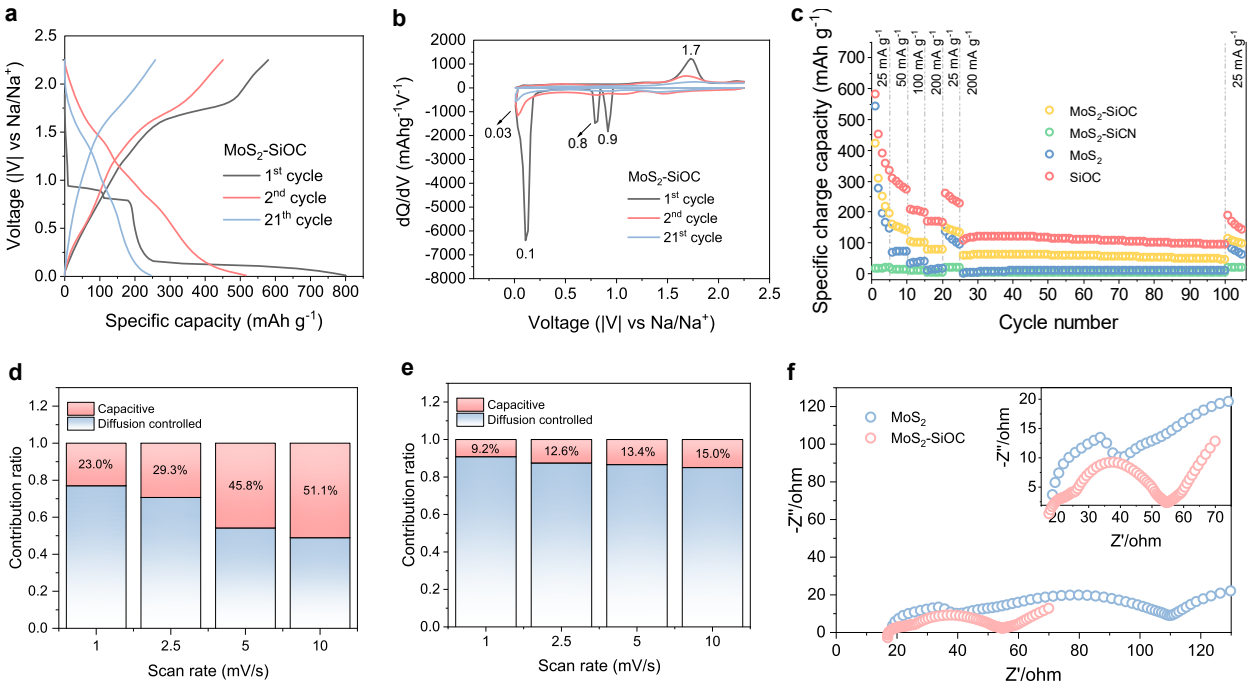

Figure 3.7: *(a) Charge and discharge profiles of MoS_2-SiOC half-cell composite between* 0.01 V *and* 2.25 V *versus* Na/Na^+ *at* 25 mA g^{-1}*, and (b) respective differential capacity curves; (c) cycle performance comparison of pristine and composite half-cell electrodes; capacitive and diffusion controlled contribution ratios for different scan rates of (d) pristine MoS_2, and (e) MoS_2-SiOC; (f) EIS of both material electrodes after one cycle of galvanostatic charge–discharge at* 50 mA g^{-1}.

corroborating to ascertain our hypothesis that SiOC protected MoS_2 species.

With respect to the sharp peak – located at ≈ 0.1 V for 1st cycle – it accounts for Na^+ adsorption on NaS_2 and Mo interface[199]; at 2nd cycle we believe such reaction took place at ≈ 0.03 V[198;204].

Due to amorphous characteristic of SiOC, and by the fact it does not is chemically bonded to MoS_2 – as corroborated by XPS and Raman spectra – the voltage plateau in charge-discharge profile of MoS_2-SiOC composite material is not significantly changed when compared to the pristine MoS_2 voltage profile (figures 3.6(a) and 3.8(a)). Therefore, the capacity contribution from SiOC was negligible[10]. Finally, in relation to agglomeration issue of MoS_2 previously mentioned, SiOC molecules may also play a role in preventing it as well as in suppressing volume expansions during insertion and extraction of Na^+[205;206]. Figure 3.7(c) presents results of rate capability test of MoS_2-SiOC and its comparison with other

half-cells, namely pristine MoS_2, pristine SiOC and MoS_2-SiCN (silicon carbon nitride), the latter another silicon-based PDC whose voltage profiles and differential capacity curves are presented in figures 3.6(b) and 3.8(b), respectively. The specific charge capacity values of MoS_2-SiOC illustrated in figure 3.7(c) were calculated considering the total mass of MoS_2-SiOC.

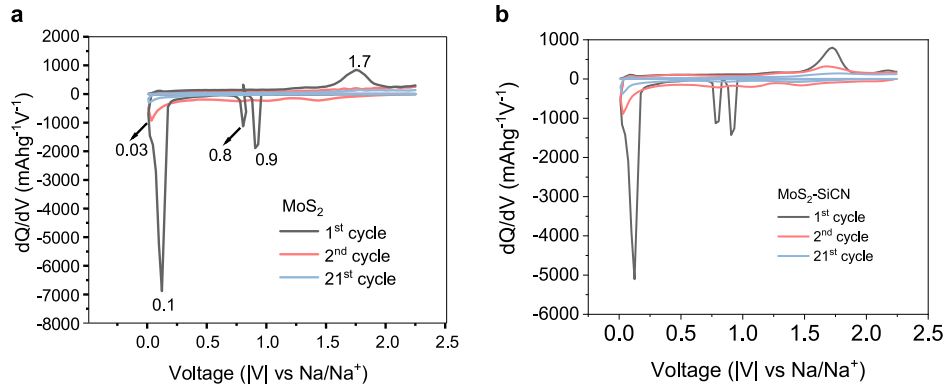

Figure 3.8: *Differential capacity curves of sodium half-cells of (a) MoS_2, (b) MoS_2-SiCN.*

Capacity values displayed were calculated according to definition presented by equation 2.3. At current densities of 25, 50, 100, and 200 $mA\,g^{-1}$, MoS_2-SiOC composite presented values for charge capacities of 226.1, 270.0, 166.5, and 92.8 $mA\,h\,g^{-1}$, respectively. Although charge capacity values dropped at higher current densities, at 200 $mA\,h\,g^{-1}$ MoS_2-SiOC presented capacity retention of $\approx$ 86.5%. Likewise, at 200 $mA\,h\,g^{-1}$, MoS_2-SiOC showed specific capacity 12 times greater than pristine MoS_2 electrode.

Figure 3.9 displays the Coulombic efficiency (η) of rate capability test presented in figure 3.7(c). As a general trend for the reported materials in this work, η at 1st cycle showed lower values. At first cycle, MoS_2-SiOC presented η of 72.4%, or first cycle loss of 27.6%, value ascribed to electrolyte decomposition and irreversible reaction of MoS_2 or SiOC species with Na^+. On the other hand, the material functionalized with SiOC exhibited at third cycle Coulombic efficiency higher than 90%, and, during rate capability test η is predominantly greater than 96%. It is also worth noting that MoS_2-SiCN electrode – synthesized under the exact same conditions as published elsewhere[157] – presented capacity retention at 200 $mA\,g^{-1}$ of $\approx$ 80% after 100 cycles. Indeed, from the data presented in figure 3.7(c), MoS_2-SiCN

confirmed that PDCs assist in providing higher stability for the MoS_2 upon cycling.

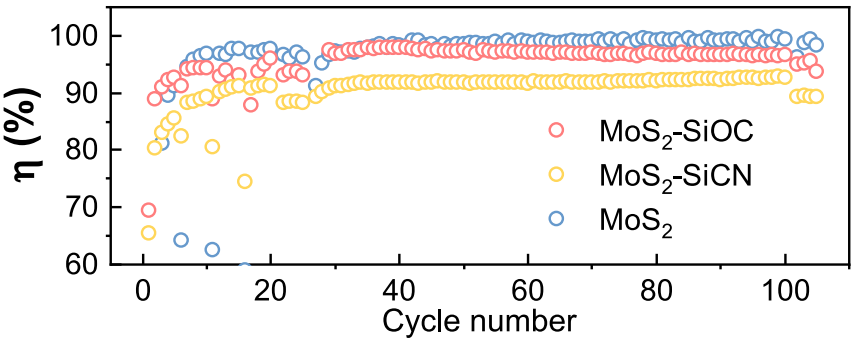

Figure 3.9: *Coulombic efficiency (η) comparison of various electrode materials used in this study.*

Overall, MoS_2-SiOC composite outperformed all the electrodes presented in figure 3.7(c). A summary of the electrochemical data is presented in table 3.3.

To further assess the stability of MoS_2 upon functionalization, other MoS_2-SiOC electrodes were prepared with higher weight loading of preceramic polymer, namely MoS_2:TTCS (1:4) and (1:10) weight ratios. Figure 3.10(a,b) depicts the rate capability tests of theses materials.

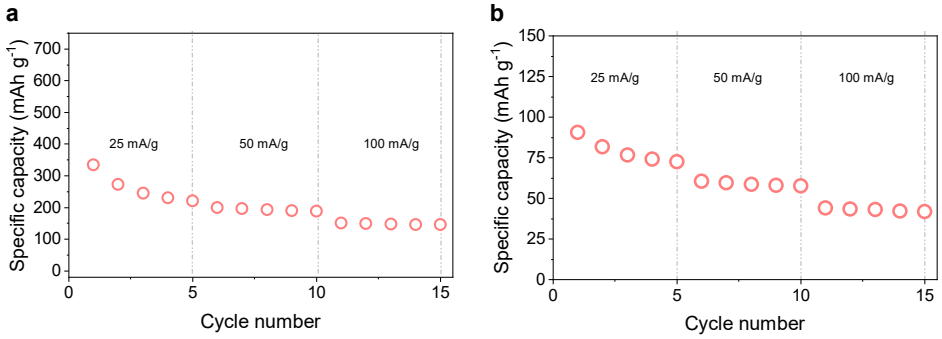

Figure 3.10: *Rate capability of MoS_2-SiOC electrodes, synthesized with (a) MoS_2:TTCS (1:4) wt. ratio, and (b) MoS_2:TTCS (1:10) wt. ratio.*

According to figure 3.10(a,b), one can see that although stability is reached, the specific capacities are lower than the electrode prepared with MoS_2:TTCS (1:1) wt. ratio; therefore, ascertaining our claim that SiOC capacity contribution is negligible, and higher proportion of it in electrode drives the capacity down, as the specific capacities were calculated considering the total mass of MoS_2-SiOC. As a result, MoS_2:TTCS (1:1) weight ratio was the best

Table 3.3: *MoS_2 (sheet morphology only) electrode data in SIB half-cell from the literature.*

Material description	Synthesis	Voltage range (V vs Na^+/Na)	Electrolyte	Current density ($mA\,g^{-1}$)	Charge capacity ($mA\,g^{-1}$) / cycle number	η at first cycle %	Ref.
MoS_2 nanosheets / rGO	Liquid exfoliation	0.4 - 2.6	1 M $NaClO_4$ in FEC/PC	20	~150 / 100^{th}	64.6	123
MoS_2	Mechanical milling	0.4 - 2.5	1 M $NaCFSO_3$ in tetraglyme	50	~89.5 / 100^{th}	87.4	207
MoS_2 nano	Molten salt electrolysis	0.01 - 2.6	1 M $NaClO_4$ in PC	20	100 / 100^{th}	~75	208
MoS_2 / rGO paper	Exfoliation and vacuum filtration	0.01 - 2.25	1 M $NaClO_4$ in EC/DMC	25	218 / 20^{th}	~75	124
MoS_2 bulk	-	0.01 - 2.25	1 M NaClO4 in EC/DMC	25	95 / 100^{th}	56	this work
MoS_2-SiOC	Pyrolysis	0.01 - 2.25	1 M $NaClO_4$ in EC/DMC	25	190 / 100^{th}	40	this work

performing as electrode based on their ratio show both stability and higher charge capacity.

In order to evaluate the the electrochemical response of MoS_2 and MoS_2-SiOC composite electrodes was evaluated from CV. Figures 3.11(a,b) present the CV at different at several scan rates (ν) of MoS_2 and MoS_2-SiOC, respectively. From such analysis one may estimate the contributions from current response in CV, which are, namely, surface capacitive effects and diffusion-controlled insertion processes[209;210]. Equation (3.6) translates this sum of these contributions.

$$\frac{i(V)}{\nu^{(1/2)}} = k_1 \nu^{(1/2)} + k_2 \tag{3.6}$$

where, in (3.6), $k_1\,\nu^{(1/2)}$ is the contribution from surface capacitive effects; while k_2 corresponds to the diffusion-controlled intercalation mechanism.

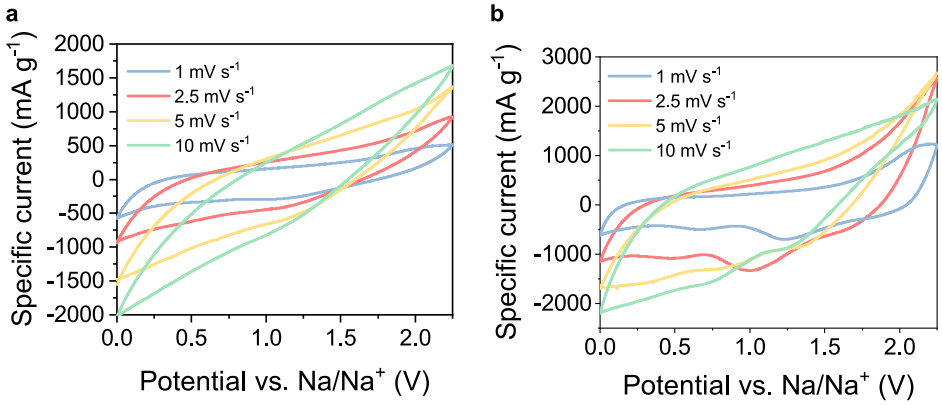

Figure 3.11: *Cyclic voltammetry used to calculate the capacitive and diffusion-controlled contributions of (a) pristine MoS_2, and (b) MoS_2-SiOC.*

From the data obtained from figure 3.11(a,b), the areal contributions were calculated. As a result, figure 3.12(a,b) was obtained, which presents a linear behavior again identified in equation (3.6); this equation allows the calculation of constant values k_1 and k_2 to calculate figure 3.7(d,e).

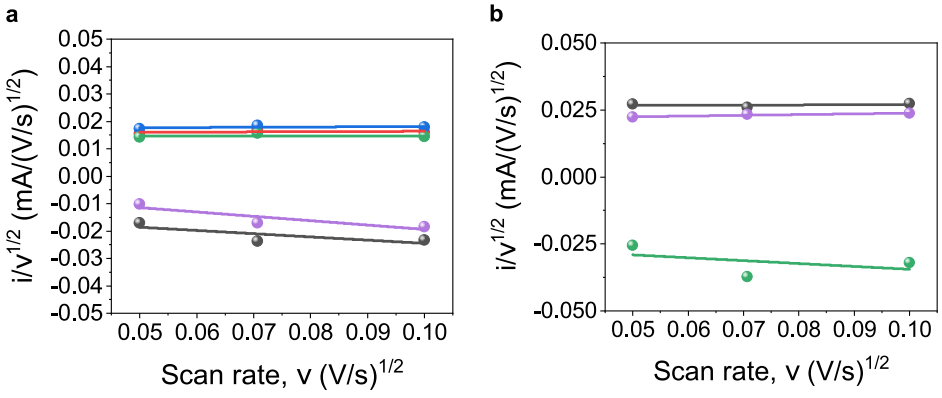

Figure 3.12: *Fitting of anodic and cathodic voltammetric sweep data of (a) MoS_2, and (b) of MoS_2-SiOC composite electrode.*

As presented by figures 3.7(d,e), as the scan rate increases, higher the capacitive contribution. Moreover, pristine MoS_2 electrode shows higher capacitive contribution than for

MoS_2-SiOC electrode. This can be illustrated that at $1\,mV\,s^{-1}$ capacitive effects accounted for MoS_2 and MoS_2-SiOC, respectively, for 23% and 9.2% for the total sodium ion storage in the system. Therefore, pristine MoS_2 charge storage relies more in capacitive mechanism than MoS_2-SiOC composite[211]. As a result, one can infer that on pristine MoS_2 electrode more charge is electrostatically stored through reversible ion adsorption at electrolyte/electrode interface than in MoS_2-SiOC electrode[190;212].

Cells were also studied by EIS technique. Figure 3.7(f) presents the complex plane impedance representation, also known as Nyquist plot. In order to provide a quantitative analysis of the electrochemical system, a circuit depicted in figure 2.16 was employed, which has following components: R_s, element characteristic of intrinsic resistance of bulk electrolyte; R_f and C_f which are, respectively, the SEI layer resistance and capacitance of dielectric relaxation. In addition, R_{ct} and C_{dl} are, respectively, the charge transfer resistance associated with exchange of current as stated by Butler-Volmer equation, and the capacitance which relies on charge accumulation the at interface of electrode/electrolyte, also known as double-layer capacitance[212–214]. Lastly, the element identified as W is referred to as Warburg element and represents the system's polarization by virtue of finite-length diffusion[91;215].

From figure 3.7(f) two semi-circles can be identified at high frequency region in Nyquist plot, characteristic shape of MoS_2 impedance spectrum[216;217]. The fitted parameters for resistance – presented by table 3.4 – show that resistance values of R_e, R_f, and R_{ct} for MoS_2-SiOC composite are, respectively, 42%, 65%, and 80% lower than pristine MoS_2.

Table 3.4: *Real impedance parameters obtained from circuit fitting from figure 2.16.*

Electrode	R_s (Ω)	R_f (Ω)	R_{ct} (Ω)
pristine MoS_2	28.9	88.7	31.9
MoS_2-SiOC composite	16.7	31.1	6.40

Based on the characterizations performed, we believe the resistance of MoS_2-SiOC composite is lower than the resistance of pristine MoS_2 because of free carbon domains of SiOC. In conclusion, with reference to small value of R_{ct} – identified by the smallest semi-circle for

MoS_2-SiOC composite – it also implicates in improved kinetics, providing greater current densities and, therefore, higher capacity values[153].

3.6 Conclusion

We have successfully synthesized SiOC functionalized MoS_2 through a facile process that involves polymer pyrolysis in inert atmosphere. As confirmed by TEM and EDX, this synthesis route allowed uniform distribution of SiOC on MoS_2 nanosheets without altering the crystal structure of MoS_2. Likewise, Raman and XPS corroborated that SiOC was deposited mainly on MoS_2 surface. The synthesized composite material was later studied as electrode material for SIB, which showed higher stability upon cycling; therefore, fulfilling its role in preventing (poly)sulfide dissolution and suppressed regeneration of MoS_2 – aspects that lead to capacity fading. Electrochemical results showed that the composite material presented specific capacity $\approx$ 12 times higher than pristine MoS_2. Additionally, characterizations demonstrated that the free-carbon domains from amorphous SiOC molecule played a role for the superior rate capability arising from increased electronic conductivity, i.e., MoS_2–SiOC half-cell tested at $200\,mA\,g^{-1}$ presented capacity retention of 86.5% – the highest among the samples evaluated. In summary, MoS_2 with precursor-derived ceramics presents facile and safe preparation, enabling the application's potential as SIB anode and continuity of research of TMDs as electrodes for rechargeable batteries.

Chapter 4

Electrochemical performance of layered Td-WTe_2[1]

4.1 Preview

Potassium-ion batteries are prominent candidates among research involving post lithium-ion batteries due to abundant availability, low-cost, and low standard reduction potential of potassium metal. Although some chemistry correlation with other monovalent alkali metal-ion batteries may exist, research on KIBs chemistry is still in its infancy. A relevant research aspect of KIBs is the development of a stable anode material that can efficiently cycle K^+ ions in its crystal structure within the 0 to 3 V potential window range; providing reasonable charge capacity and reversibility. To this end, TMDs are promising electrode materials because of their favorable electrochemical properties. In this work, we studied electrochemical performance of tungsten ditelluride (WTe_2) TMD as working electrode in a KIB half-cell. Results show that WTe_2, a telluride-based TMD, has high first cycle specific charge capacity – with up to 3.3 K^+ stored per WTe_2 molecule (at least 4 times that of WS_2 electrode) – stable capacity of 143 mA h g^{-1} at 10^{th} cycle number – outperforming WS_2

[1]Reprinted with permission from Soares, Davi Marcelo, and Gurpreet Singh. "Superior electrochemical performance of layered WTe_2 as potassium-ion battery electrode." *Nanotechnology* 31.45 (2020): 455406. IOP Publishing. All rights reserved.

($66\,\mathrm{mA\,h\,g^{-1}}$) and graphite ($95\,\mathrm{mA\,h\,g^{-1}}$) – good reversibility, reasonable cycling stability, and low charge transfer resistance.

4.2 Introduction

In the matter of alternative alkali metals to substitute lithium, potassium is currently object of intense research by virtue of abundant potassium availability, standard reduction potential ($K/K^+ = -2.93\,V$ versus E^0) closer to lithium ($Li/Li^+ = -3.04\,V$ versus E^0), high K^+ diffusion coefficient, and flexibility to deploy either copper or aluminum foil as current collector for electrodes[8;218]. Furthermore, in comparison with SIB – another beyond lithium-ion candidate – KIBs have higher theoretical energy density and lower standard reduction potential ($Na/Na^+ = -2.71\,V$ versus E^0)[21].

In addition to finding novel battery technologies to address the issues discussed in chapter 1, the development of material electrodes that can reversibility insert and extract metal ions into its structure is another challenge. In this regard, the motivation behind the use of layered TMD-based electrodes for ESS primarily stems from the fact that TMDs have larger interlayer spacing – approximately 6 Å vs. 3 Å in graphite – and unique conversion chemistry with alkali-metal ions. These facts make TMDs more suitable as metal-ion host than traditional graphite anode. It is noteworthy to mention that the commercial success of LIB was largely attributed to the discovery of graphite anode. However, the large radius of K^+ and sluggish kinetics (compared to Li^+) makes it difficult for graphite to accommodate the repeated K^+ uptake causing fast capacity fading[74].

Larger inter-layer spacing makes TMDs potential host materials for electrochemical storage of metal ions, such as Na^+, K^+, Mg^{2+}, and Ca^{2+}; accordingly, offering enhanced diffusion towards these metal ions[219–221]. Among various TMDs, sulphide-based TMD electrodes such as MoS_2[124;222;223], SnS_2[80], TiS_2[224], VS_2[41], and WS_2[92;225] have been reported as prospective electrode materials in alkali-ion based batteries; while reports on selenide-based TMDs have gained traction only recently[83;84;226].

Belonging to group 6, Mo- and W-based TMDs were closely analyzed for this study given

Table 4.1: *Crystallographic data of TMDs. Copyright Springer & Material Phases Data System (MPDS), Switzerland & National Institute for Materials Science (NIMS), Japan, 2016.*

	MoS_2	$MoSe_2$	$MoTe_2$	WS_2	WSe_2	WTe_2
Space group	P63/mmc	P63/mmc	Pmn21	P63/mmc	P63/mmc	Pmn21
a (nm)	0.316	0.329	0.347	0.314	0.329	0.348
b (nm)	0.316	0.329	0.633	0.314	0.329	0.627
c (nm)	1.23	1.29	1.39	1.23	1.29	1.40
α (°)	90	90	90	90	90	90
β (°)	90	90	90	90	90	90
γ (°)	120	120	90	120	120	90

the potential applications, electronic properties, and polymorphism of those. Table 4.1 shows the main crystallographic data of Mo- and W-based TMDs. From the presented data, one can see that WTe_2 displays the largest c among all the analyzed structures; thus, an attractive properties for intercalation of larger ions.

Apart from its semimetallic characteristic, Td-WTe_2 is also attractive for KIBs due to its interlayer space (c = 14.07 Å), which is expected to provide more efficient and faster intercalation of K^+ ions within its interlayer spacings.

After conducting this initial theoretical analysis, an experimental study was performed to assess the long-term stability upon cycling of three species of W-based TMDs as KIB half-cells at 100 mA g^{-1}. The rationale for selecting W-based TMDs is because the novelty of them – as Mo-based TMDs are commonly reported – as well as the larger interlayer spacing of WTe_2. Results of this electrochemical test are presented in figure 4.1.

Based on the higher stability and charge capacity of WTe_2, this TMD was chosen to be studied. Moreover, to our best knowledge this is the first report on WTe_2 TMD as anode for KIB.

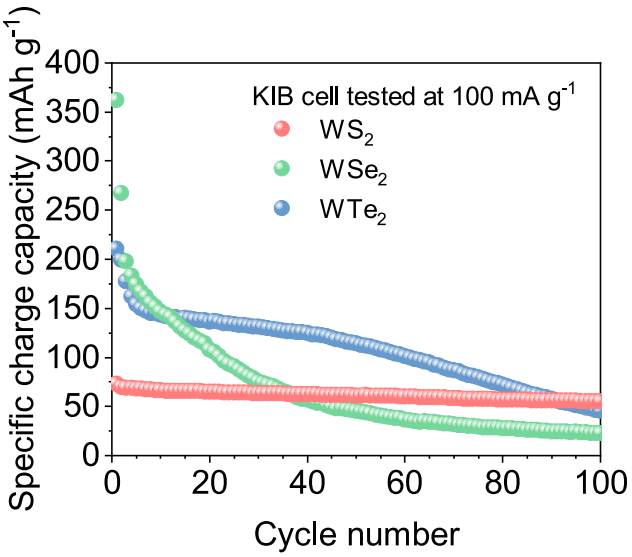

Figure 4.1: *Electrochemical performance of W-based TMDs in long-term cycling.*

4.3 Experimental

4.3.1 Material preparation

Electrodes studied were synthesized with the corresponding composition: 70 wt.% of TMD as active material – WTe_2 (Ossila 99.9+%), WS_2 (Sigma Aldrich 99%), or graphite (Sigma Aldrich 99%) – 15 wt.% of carbon black (Alfa Aesar 99.9+%) as conducting agent, and 15 wt.% of poly(vinylidene fluoride) as binder (Alfa Aesar). Upon obtaining a homogenous slurry – through the addition of few drops of 1-Methyl-2-pyrrolidinone (Sigma Aldrich) – the mixture was cast on a 9 μm thickness copper substrate and subsequently dried for 18 hours at 80 °C for solvent removal. The thickness of the thin films deposited was found to be approximately 125 μm. Regarding the KIB cells, coin cells (CR2032 model) were used for assembly in a high precision argon atmosphere glove box, where potassium metal was used on the negative side and the synthesized electrode on the other side. Electrodes were separated by a monolayer membrane (Celgard) soaked in 1 M KPF_6 (Alfa Aesar) in (1:1 v/v) EC:DMC (anhydrous, 99%, Sigma). All synthesis reported herein were performed using materials as received and without any further purification.

4.4 Material characterization

The morphology of samples was investigated low- and high-resolution TEM using Philips CM 100 kV and FEI Tecnai Osiris 200 kV, respectively. In addition, Renishaw Invia Raman spectrometer, laser wavelength of 532 nm, was used to understand further the interlayer interaction and changes in the structure of the synthesized materials. XPS was performed to analyze the surface chemistry using a Thermo Scientific, monochromatic Al anode Kα (hν = 1486.6 eV), spot size 400 μm, with in-situ sputtering with Ar^+ at 3 keV for 2 minutes for surface contamination removal. The crystal structure was evaluated using Bruker AXS D8 advance Cu Kα, wavelength 1.540 60 Å. KIB cells were studied in Arbin BT2000 multichannel tester and electrochemical station CHI660E, from CH Instruments, Inc.

4.5 Results and discussion

Morphology and structure were evaluated by SEM – presented in figure 4.2(a,b) – TEM and STEM.

The TEM image presented by figure 4.4(a) shows the layered morphology of pristine WTe_2. From Figure 4.4(b), WTe_2 presents lattice fringes of approximately 3.5 Å, ascribed to Td-WTe_2 (100) plane. In addition, SAED of WTe_2 – depicted by Figure 4.4(c) — is in agreement with the atomic structural model of Td-WTe_2 illustrated by Figure 4.4(d)[116;227], as well as measurements displayed by figure 4.3 and table 4.2.

Lastly, Figure 4.4(e) exhibits the HAADF and Figure 4.4(f-h) presents STEM images with elemental mapping of pristine Td-WTe_2.

With respect to crystal phase, XRD pattern (figure 4.7(a)) of the electrode as prepared confirms the Td phase in orthorhombic space group $Pmn2_1$[228]. Moreover, the most intense peak located at 12.6°, assigned to plane (002), corresponds to a plane-spacing distance between adjacent planes of 7 Å (equation 4.1); hence, more than 13.5% wider than 2H-WS_2 (equation 4.2) and 2H-MoS_2 (equation 4.2)[229–231], evidence that may indicate higher intercalation capacity in WTe_2 layered structure. It is essential to highlight that there are

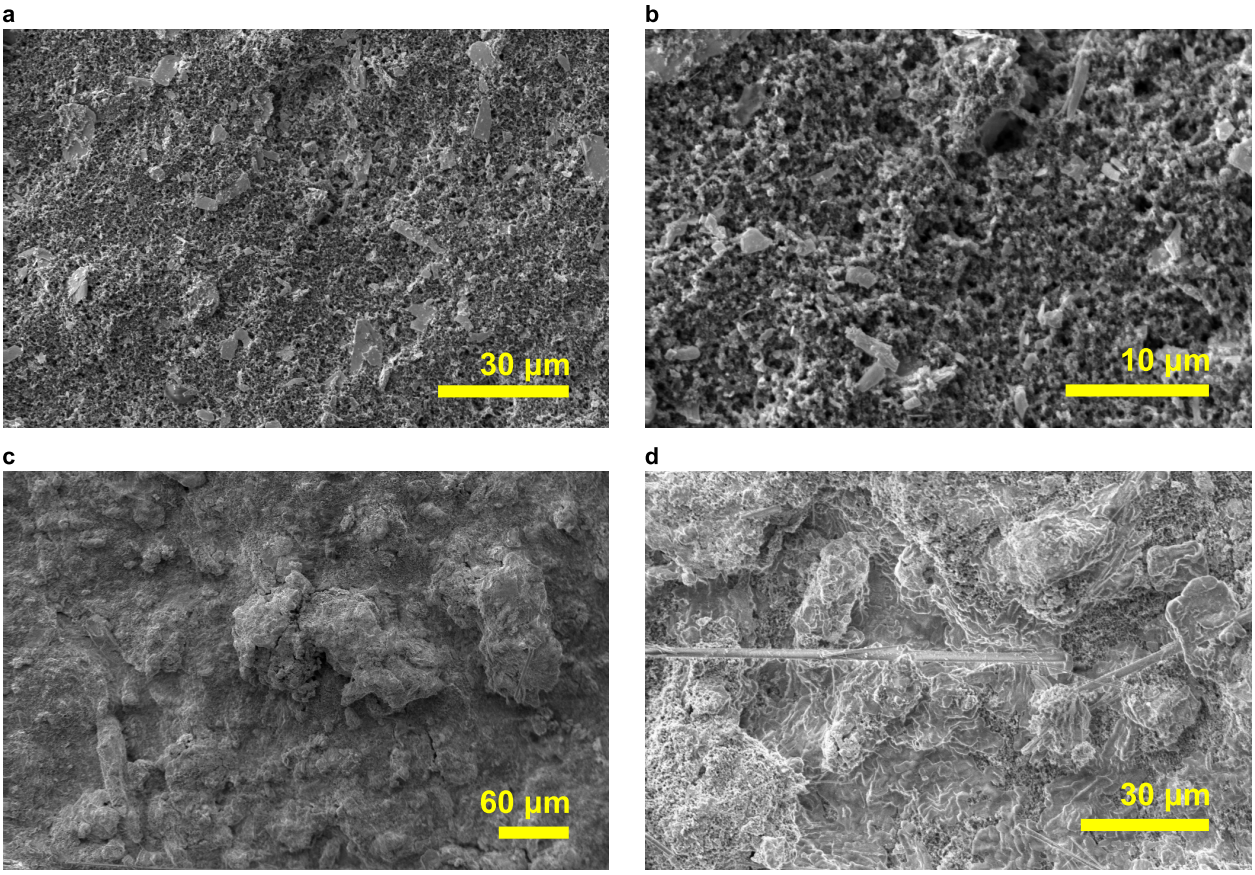

Figure 4.2: *SEM morphology characterization of Td-WTe_2. (a,b) Electrode as synthesized (prior to cell assembly). (c,d) After discharge at* $100\,\mathrm{mA\,g^{-1}}$.

papers in the literature that report WTe_2 Td phase identical to 1T′, which is not correct. For clarification, crystal structures of the TMDs reported herein and WTe_2 common phases are presented by figures 4.5 and 4.6, respectively.

$$\frac{1}{d^2} = \frac{h^2}{a^2} + \frac{k^2}{b^2} + \frac{l^2}{c^2} \tag{4.1}$$

$$\frac{1}{d^2} = \frac{4}{3}\left(\frac{h^2 + kh + k^2}{a^2}\right) + \frac{l^2}{c^2} \tag{4.2}$$

The Raman spectrum, shown by figure 4.7(b), is in consonance with bulk WTe_2, where four vibrational modes can be identified, namely, A_2^4, A_1^8, A_1^5, and A_1^2, at approximately 110, 132, 162 and $208\,\mathrm{cm^{-1}}$, respectively[235–238]. The phonon mode A_2^4 implies that the material is neither monolayer nor few layers[239], implying that no exfoliation procedure was performed.

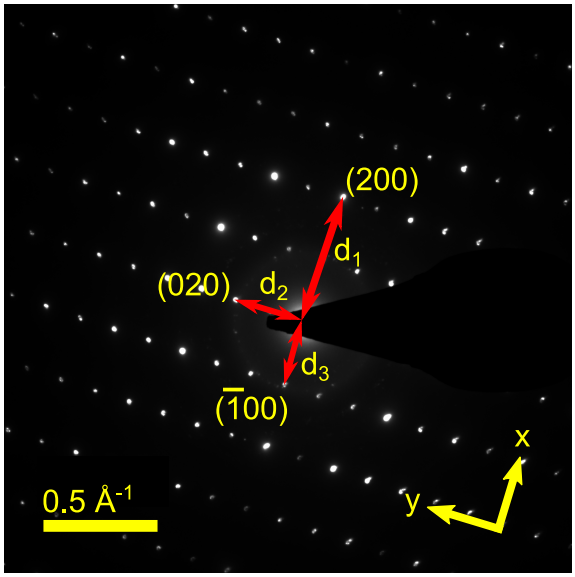

Figure 4.3: *Selected area electron diffraction (SAED) of Td-WTe_2. Reported in the inorganic crystal structure database (ICSD collection code 14348).*

Table 4.2: *Distances highlighted in Figure 4.3 with respective calculated data – performed using ImageJ 1.52p.*

Distance identification	x	y	G (nm^{-1})	d (Å)
d_1	22.6685	14.0422	5.8580	1.7071
d_2	17.8826	18.6258	3.2003	3.1247
d_3	20.0590	22.4206	2.9174	3.4277

The XPS survey scan is exhibited in figure 4.7(c). XPS spectrum of W4f line is presented by figure 4.7(d), where the two prominent peaks are located at 31.2 and 33.3 eV, respectively, characteristic of spectral lines $W4f_{7/2}$ and $W4f_{5/2}$, assigned to W – Te bonds – the chemical shift of $\Delta E = 2.1$ eV is in accordance with the literature results[240]. As regards Te3d spectral line, figure 4.7(e) exhibits the $Te3d_{5/2}$ and $Te3d_{3/2}$ peaks at 572.6 and 583.0 eV, respectively, also ascribed to W – Te bonds[241].

Concerning electrochemical analysis, for the first GCD cycle, at 50 mA g^{-1}, WTe_2 delivered specific charge capacity of 238.8 mA h g^{-1} with Coulombic efficiency (η) of 50.7%; whereas, at 100 mA g^{-1}, it delivered specific charge capacity of 210.7 mA h g^{-1} with η of 49.0%. These initial low η values account for the SEI formation, a process where reduction of ethylene carbonate and dimethyl carbonate – from the electrolyte – occurs, producing a

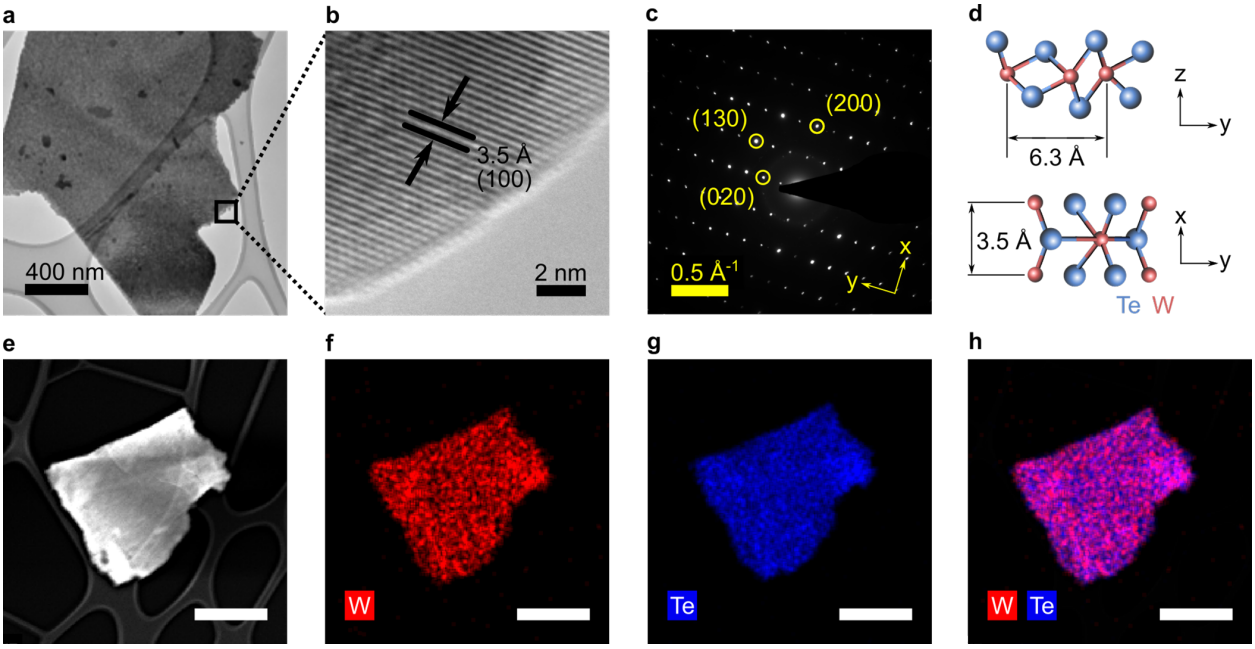

Figure 4.4: *Morphology characterization of pristine Td-WTe_2. (a) Low-resolution TEM. (b) High-resolution TEM. (c) SAED pattern of Td-WTe_2 pristine. (d) Schematic of Td-WTe_2 phase structure (ICSD collection code 14348). (e) HAADF. (f-h) STEM with mapping of the indicated elements. Scale bars for (e-h) is* 800 nm.

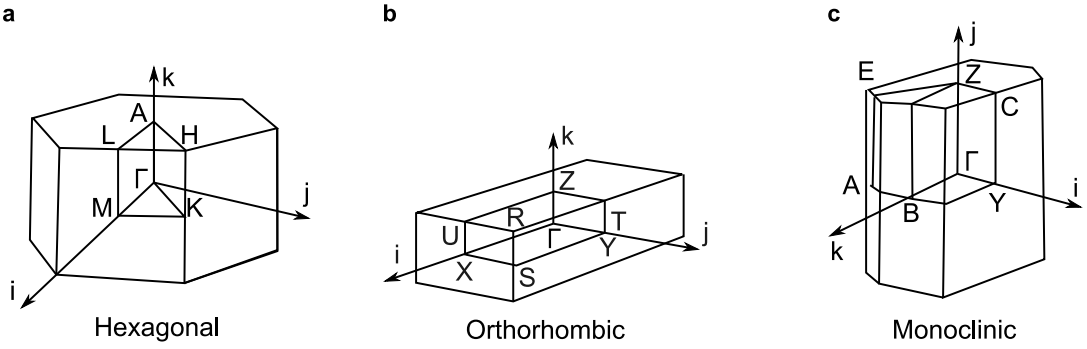

Figure 4.5: *Crystal structures (Brillouin zones) schematic. (a) Hexagonal 2H. (b) Orthorhombic. (c) Monoclinic.*[232–234].

thin layer on the anode material[242]. Despite culminating in initial lower η values, the SEI is beneficial to the cell by lowering the chances of solvent species intercalation into active material layers and mitigating the exfoliation of it. Likewise, SEI may also prevent further electrolyte decomposition[243].

Additionally, the only plateau at the first cycle discharge in figure 4.8(a) suggests that K^+ intercalation happens at the average potential of 0.47 V versus K/K^+, with a maximum

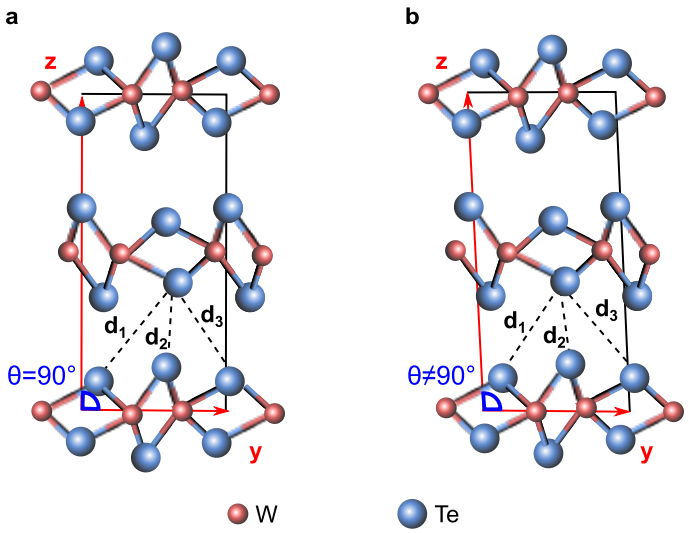

Figure 4.6: *Lattice structure variants of WTe_2. (a) Td phase with orthorhombic non-centrosymmetric unit cell with* $d_1 > d_3$ *and* $\theta = 90°$. *(b) 1T' phase with monoclinic centrosymmetric unit cell, where* $d_3 > d_1$ *and* $\theta > 90°$.

of $3.3K^+$ inserted or extracted per WTe_2 molecule, value that outperforms values of widely reported TMD species such as MoS_2, (K_2MoS_2) and WS_2 ($K_{0.65}WS_2$) KIBs at $100\,mA\,g^{-1}$, as displayed by figures 4.9(a) and 4.9(b), respectively. From the differential capacity curve (dQ/dV) in figure 4.8(b) the overlap of second and third cycle curves demonstrates the reversibility of WTe_2 [92;244;245]. Consequently, the superposed peaks from second and third cycles present the cathodic and anodic peaks at approximately 1.15 and 1.61 V, correspond to potassiation and depotassiation, respectively. Overall, the proposed mechanism of K^+ storage in WTe_2 anode consists of an intercalation reaction, which takes place at a potential above 0.4 V *vs.* K/K^+, and a conversion reaction, as shown by equations (4.3) and (4.4), respectively.

$$WTe_2 + x\,K^+ + x\,e^- \longleftrightarrow K_xMoTe_2 \tag{4.3}$$

$$K_xWTe_2 + x\,K^+ + x\,e^- \longleftrightarrow 2\,K_xTe + W^0 \tag{4.4}$$

Apart from GCD tests, WTe_2 electrode was also evaluated in terms of rate capability under different current densities. From figure 4.8(c) one can see that WTe_2 anode delivered

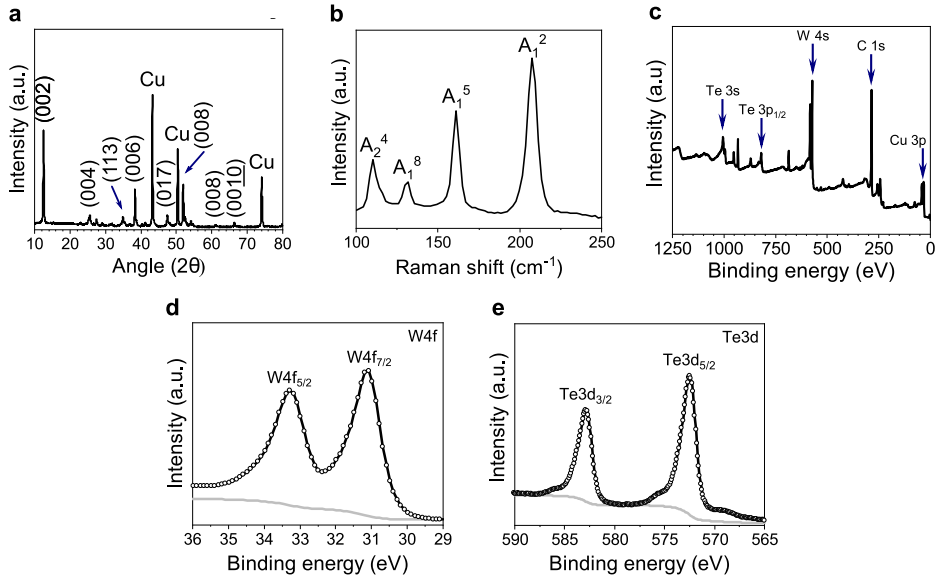

Figure 4.7: *Characterization of pristine Td-WTe_2 electrode before KIB cell assembly. (a) XRD. (b) Raman. XPS (c) survey scan, (d) W4f, and (e) Te3d.*

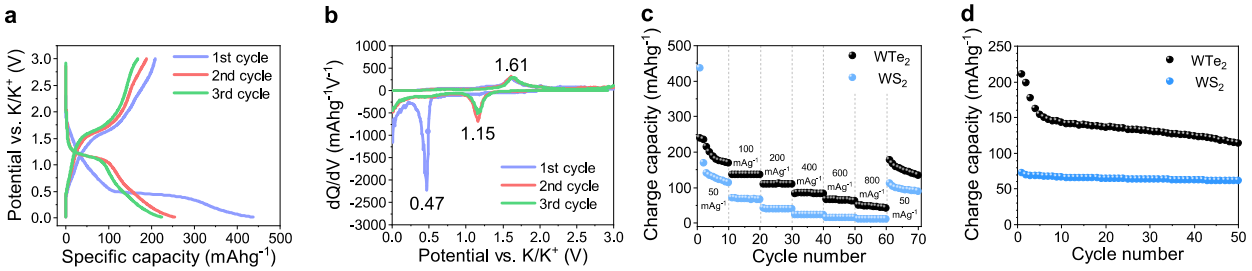

Figure 4.8: *Electrochemical characterization of potassium-ion half-cells. (a) WTe_2 electrode voltage profile upon charge and discharge cycles at* $100\,\mathrm{mA\,g^{-1}}$*, and (b) respective WTe_2 electrode differential capacity curves. (c) WTe_2 and WS_2 electrodes rate capability test. (d) Potassium specific charge capacity at constant current density of* $100\,\mathrm{mA\,g^{-1}}$ *of WTe_2 and WS_2 electrodes*

specific charge capacities of 238.8, 136.2, 108.4, 82.6, 66.0, 50.12, and $176.4\,\mathrm{mA\,h\,g^{-1}}$ at 50, 100, 200, 400, 600, 800, and $50\,\mathrm{mA\,g^{-1}}$, respectively. Although at lower current densities the capacity decay was more prominent, it is worth noting that the 10^{th} cycle, at $50\,\mathrm{mA\,g^{-1}}$, presented a reversible specific capacity value lower than the 61^{st} cycle – also at $50\,\mathrm{mA\,g^{-1}}$; again, conveying the reversibility of WTe_2[92;246]. Moreover, figure 4.8(c) exhibits the rate capability and superior specific charge capacity of WTe_2 over WS_2. Pertaining to long term cycling test, figure 4.8(d) presents the specific charge capacities of WTe_2 and WS_2 electrodes

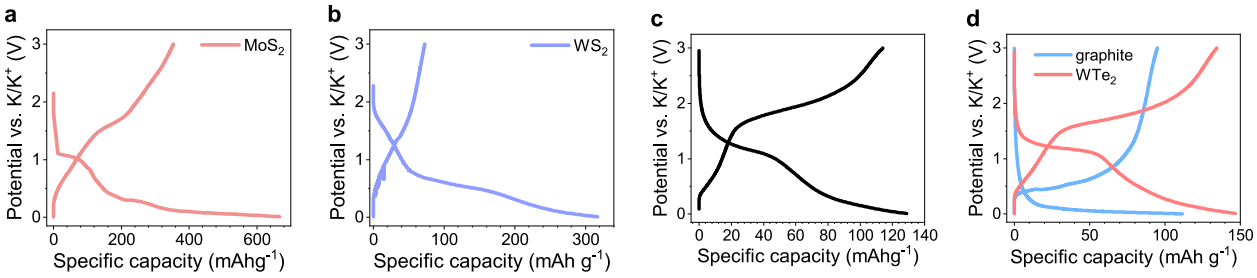

Figure 4.9: *First cycle Voltage profiles of KIB cells assembled in 1 M KPF_6 in EC:DMC (1:1) vol. % and cycled at* $100\,\mathrm{mA\,g^{-1}}$ *of (a) 2H-MoS_2, and (b) 2H-WS_2. (c)* 50^{th} *cycle Voltage profile of WTe_2 KIB at constant current density of* $100\,\mathrm{mA\,g^{-1}}$*. (d)* 10^{th} *cycle Voltage profile of WTe_2-KIB and graphite-KIB, both tested at constant current density of* $100\,\mathrm{mA\,g^{-1}}$ *in 1 M KPF_6 in EC:DMC (1:1) vol. %.*

at $100\,\mathrm{mA\,g^{-1}}$. Importantly, for the electrochemical characterizations no activation on the material was performed, i.e., running the first cycle with a lower current density procedure that may impact the electrochemical performance results presented herein. As a result, after the formation of SEI, from the 5^{th} up to the 50^{th} cycle capacity retention was $\approx 74\%$.

As an inherent aspect of the high reversibility, figure 4.9(c) shows the well defined voltage plateau at 50^{th} cycle, whose shape and voltage profile remain close to second and third cycles depicted in figure 4.8(a). In part, the superior electrochemical performance of WTe_2 can also be attributed to its larger interlayer as well as to its semimetallic nature, which has implications on reversibility[247]. Deemed to be an important material for LIB and KIB, graphite presents more favorable intercalation in potassium than in lithium in terms of enthalpy of formation of KC_8 ($-27.5\,\mathrm{kJ\,mol^{-1}}$) and LiC_6 ($-16.5\,\mathrm{kJ\,mol^{-1}}$)[4]. Similar to TMDs, graphite revealed a capacity decay within the first cycles, showing subsequently reasonable stability up to 50 cycles in EC:DMC electrolyte[74]. At $100\,\mathrm{mA\,g^{-1}}$, in the 10^{th} cycle graphite presented specific charge capacity of approximately $95\,\mathrm{mA\,h\,g^{-1}}$, whereas WTe_2 yielded $143.3\,\mathrm{mA\,h\,g^{-1}}$, as presented by figure 4.9(d). In the same manner, η of WTe_2, for the respective cycle, was 91.1%, whilst graphite presented 85.1%. As a consequence, although graphite possesses good electrical conductivity and layered structure – factor that facilitates the diffusion of K^+ – WTe_2 larger interlayer spacing and conversion type reaction are some of the compelling features that allow WTe_2 to outperform graphite as KIB anode material[97].

To further understand the interfacial phenomena and mechanism of K^+ storage, EIS was

conducted from 0.1 to 1×10^5 Hz. Regarding the equivalent circuit employed, considering that each electrochemical system has its particularities, a different model to the presented in figure 2.16 was used. Even though no restriction applies to the number of circuit elements used for EIS fitting, each circuit should be physically identified and assigned to the respective phenomena taking place at the electrode and electrode/electrolyte interface. To this end, an approach referred to Occam's razor can be applied. Occam's razor principle states that the number of circuit elements in the equivalent circuit shall be not more than the respective physical phenomena[248]. In summary, the simplest model capable of physically providing a reasonable electrochemical impedance simulation shall be employed[89]. As one can see in figure 4.10(a), for the cells after cycling at the lower frequency region an approximate linear behavior exists. Such behavior differs from theory – where a vertical line describes a pure capacitive system in the Nyquist plot – and consequently is characteristic of a real system–where the charge storage is proportional to the time[248]. In order to model a system that is phase-dependent, a circuit element known as CPE is employed[249]. The CPE element takes into account the frequency dispersion process caused by the adsorption of anions on the surface of the electrode and its non-homogeneity in atomic-scale[250;251]. CPE complex impedance mathematical representation is presented in equation 2.15.

Table 4.3: *EIS summary values of KIB anode materials reported in the literature. The equivalent fitting circuit is presented by Figure 2.16.*

Material - cell	Condition	R_s (Ω)	R_f (Ω)	R_{ct} (Ω)	Electrolyte	Reference
Graphite - KIB	After three GCD (activation cycles)	5.046	87.88	4358	1 M KPF_6 in EC:PC (1:1) by volume	74
WS_2 - KIB	Initial	57.73	-	4615	5 M KTFSI in DEGDME	92
	After five cycles	5.46	31.54	1671		

In the Nyquist plot, in figure 4.10(a), the WTe_2 phase angles φ_1 and φ_3 – where φ_i was

identified in equation 2.16 – for 1 and 3 discharge cycles were, respectively, $|\varphi_1| = 20°$ and $|\varphi_3| = 13°$. Therefore, the Warburg element should not be employed – as discussed in section 2.5.1. Consequently, in the present work, instead of using a model with Warburg-Randles circuit[91] – a model that only has CPE elements is more suitable[252]. Likewise, the model introduced in this work is more flexible because despite not having a Warburg element, this model may, if the Nyquist representation pertains, have $n = 1/2$. Concisely, this novel model intends to have an equivalent circuit that does not present Warburg since the phase angle is not 45°. In fact, authors suggest that each electrochemical system should be carefully studied since generalized equivalent circuits may sometimes lead to discrepancies in the quantitative impedance analysis, and misinterpretation of the phenomena taking place.

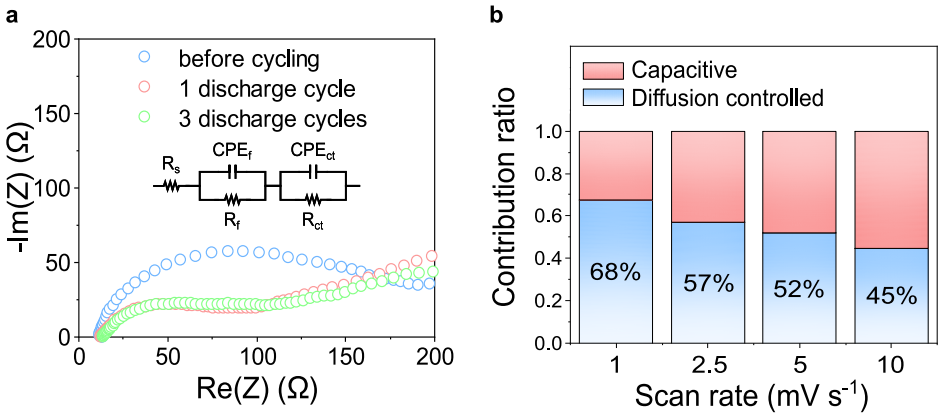

Figure 4.10: *(a) EIS of WTe_2 electrode before, after one, and after three potassiation cycles; inset: equivalent circuit employed for EIS curve fitting. (b) Capacitive and diffusion-controlled contribution ratios for different scan rates of WTe_2 electrode.*

In the circuit depicted by figure 4.10(a) inset, R_s accounts for the equivalent series resistance, R_f and CPE_f are, respectively, the resistance of SEI layer and dielectric relaxation capacitance; and, lastly, R_{ct} and CPE_{ct} are the charge-transfer resistance and capacitance, respectively. Results presented by table 4.4 suggest a decrease in R_{ct} value; therefore, indicating that the processes occurring in the WTe_2 electrode may get faster as the galvanostatic charge-discharge happens[91].

Furthermore, the R_s value remains stable. Considering that R_s takes into account contributions from the system, namely, intrinsic resistance from the electrode and interfacial

resistance between active material and current collector[212], the stable R_s value can be ascribed to the preservation of sites for electronic transfer at the surface of the electrode[247]. For comparison purposes, a summary of EIS fitting results with other anode materials for KIB – and the respective equivalent fitting circuit is presented in table 4.3.

Table 4.4: *Real impedance parameters obtained from circuit fitting from figure 4.10 inset upon GCD at* $100\,\mathrm{mA\,g^{-1}}$.

Electrode	R_s (Ω)	R_f (Ω)	R_{ct} (Ω)
After one cycle	13.2	64.3	233.0
After three cycles	13.5	188.0	68.7

Correspondingly, CV of WTe_2 and WS_2 were performed to evaluate the charge storage mechanisms of each material and are presented by figures 4.11(a) and 4.11(b), respectively.

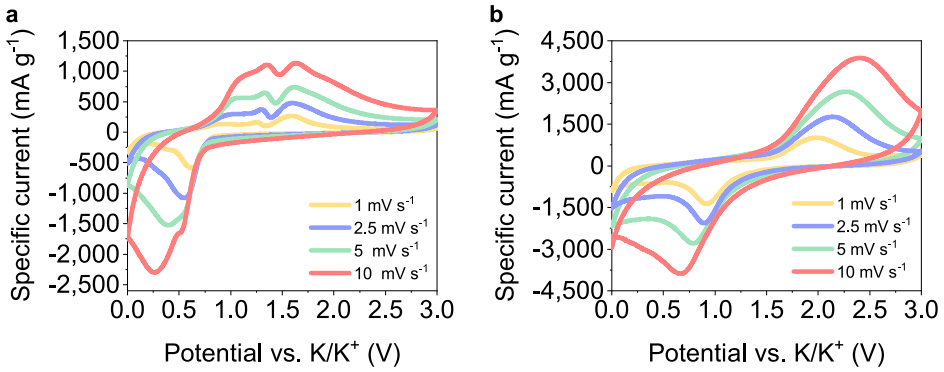

Figure 4.11: *Cyclic voltammetry after one discharge at* $100\,\mathrm{mA\,g^{-1}}$ *used to calculate the capacitive and diffusion-controlled contributions of (a)* WTe_2*, (c)* WS_2*.*

In accordance with the definition quantified by equation 3.6, for a potential the current response ($i(V)$) is given as for surface capacitive mechanism, revealed by a constant response of $di(V)/d\nu$, and diffusion-controlled effect – attributed to constant $di(V)/d\nu^{(1/2)}$. In sum, taking both charge storage processes into account results in equation 4.5[209;253].

$$i(V) = k_1\nu + k_2\nu^{(1/2)} \tag{4.5}$$

Where in equation 4.5, ν is the scan rate, $k_1\,\nu$ and $k_2\,\nu^{(1/2)}$ are, respectively, the capacitive and diffusion-controlled portions arising from the current response $i(V)$[36;253]. As per

expectation, the higher the scan rate, the higher is the capacitive contribution of WTe_2 and WS_2,

As presented in figure 4.10(b) at $5\,mV\,s^{-1}$ the majority of the total potassium-ion storage in WTe_2 is assigned to diffusion-controlled process (52%); in contrast, for WS_2 such mechanism accounts for 36% (figure 4.12). To summarize, for all scan rates analyzed, WS_2 presents higher surface effect contribution compared to WTe_2.

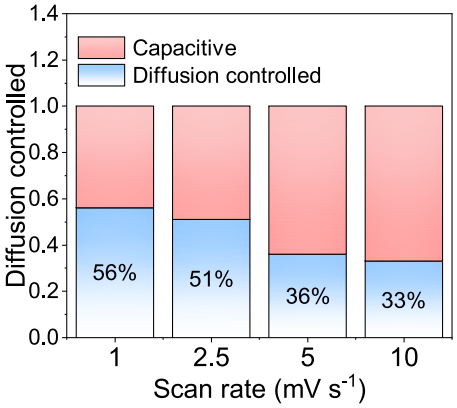

Figure 4.12: *Capacitive and diffusion-controlled contribution ratios for different scan rates of WS_2.*

In relation to post-cycling analysis, morphology of the disassembled cell is portrayed by figure 4.2(c,d), which shows a SEI formation. Further, ex-situ analysis of the potassiated and depotassiated cells were also performed. Firstly, the survey scan of the potassiated electrode is shown in figure 4.13(a). Deconvolution of W4f region is presented by figure 4.13(b), in which peaks corresponding to $W4f_{7/2}$ could be assigned to elemental tungsten (W^0) at 30.8 eV and W^{5+} oxidation state at 34.7 eV[254;255]. Concerning the K2p core-level region, figure 4.13(c) reveals two peaks assigned to $K2p_{3/2}$ and $K2p_{1/2}$ with binding energies of 292.8 eV and 295.2 eV, respectively, assigned to K^+ ions[256;257]. These potassium ions could be bonded together with Te, since the high-resolution Te3d (figure 4.13(d)) peaks at 571.7 and 582.0 eV are assigned to $Te3d_{5/2}$ and $Te3d_{3/2}$, respectively; these peaks are reported by the literature as Te oxidation state -2[258]. Lastly, the shoulder peaks at 574.5 and 585.8 eV are attributed to oxide species, such as TeO_2 – spontaneously formed on the surface of the material[257]. In summary, the elemental tungsten (W^0) arising from WTe_2

molecule can be an indicative of the conversion reaction proposed in equation 4.4. Likewise, during potassiation the metallic tungsten identified, along with Te oxidation state -2 and K^+, may be an indication of the formation of K_2Te, as presented by equation 4.4[258;259].

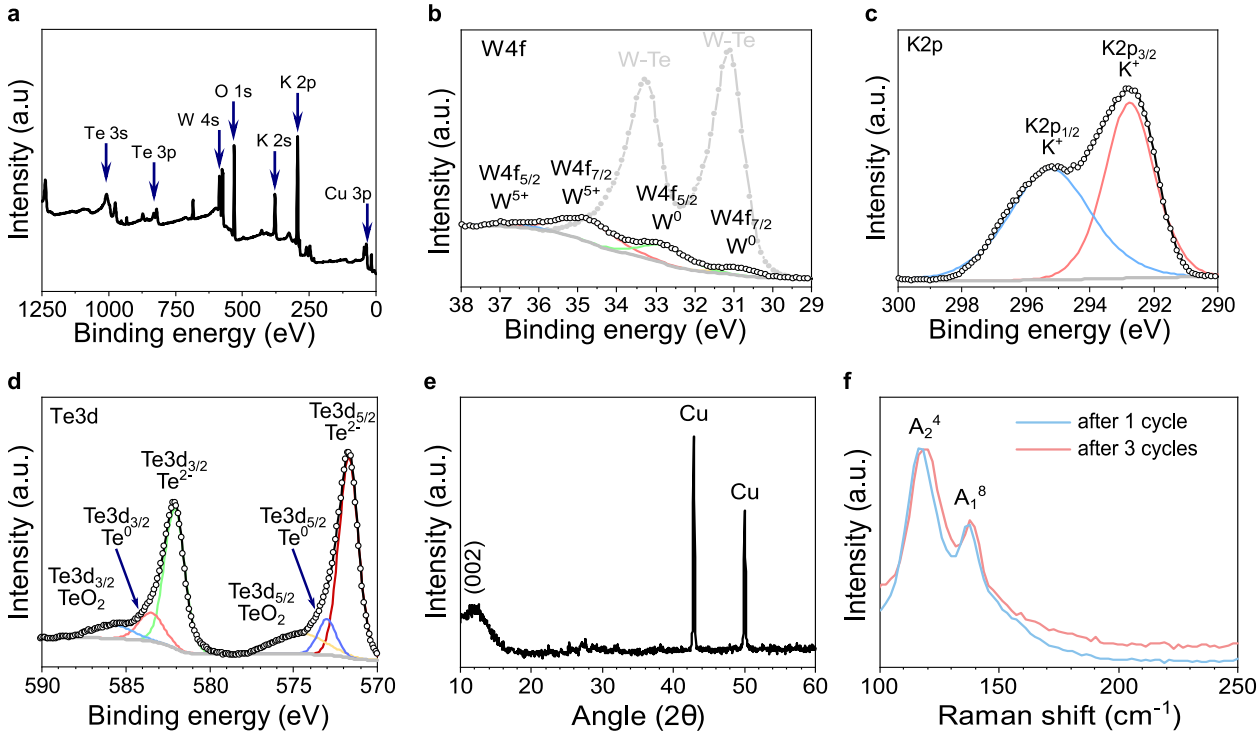

Figure 4.13: *Post-cycling characterizations of WTe_2 anode. (a) XPS survey of potassiated. (b) XPS of W4f first cycle and as-assembled WTe_2 electrode in the background (grey curve) upon potassiation. Potassiated Td-WTe_2 electrode after 1 cycle at* $100\,\mathrm{mA\,g^{-1}}$ *high resolution XPS of (c) K2p, and (d) Te3d. Depotassiated WTe_2 electrode characterization (e) XRD, and (f) Raman spectra.*

With respect to XRD of the depotassiated electrode, presented by figure 4.13(e), a broadened peak – assigned to plane (002) – was identified. This modification may indicate some degree of degradation of WTe_2, possibly owing to conversion-type reactions with K^+. Ultimately, from figure 4.13(f) one can see that Raman modes A_1^5 and A_1^2 – previously identified in the material in figure 4.7(b) – are absent after 1 and 3 GCD cycles, another evidence that in the post-cycling analysis that the W$-$Te bonds are modified.

4.6 Conclusion

We have reported Td-WTe_2 as a counter electrode in potassium-ion battery half-cell. Having its most stable thermodynamically phase as semimetallic in nature (Td), electrochemical studies demonstrated the high reversibility of this TMD, without the need to have onerous conducting agents, such as reduced graphene oxide (rGO), in the electrode formulation. The reversibility is evidenced by the differential capacity analysis and rate capability test. Moreover, the high specific capacity and reasonable stability on cycling are remarkable attributes of this TMD. Evaluated on its pristine bulk form, WTe_2 stored up to 3.3 K^+ per molecule according to our studies – the highest value among the commonly reported sulphide-based TMDs tested and graphite. Further, the calculated and observed larger interlayer spacing offers adequate distance and a shorter path for K^+ intercalation. Nonetheless, the initial irreversible capacity and possible (poly)telluride dissolution are topics that require further elucidation towards a better understanding of this material. About electrochemical characterization, a relevant discussion regarding the EIS fitting is presented to emphasize that models published in the literature should be primarily analyzed for the system under consideration before performing any fitting. As a result, a novel equivalent circuit for KIB is introduced. In conclusion, this initial study aims at bringing attention to telluride semimetal conversion-type TMD species for applications in electrochemical energy storage. Authors hope that this study may contribute to further developments involving layered materials

Chapter 5

A comparative study of Td-WTe_2 as electrode material for sodium-ion and potassium-ion batteries

5.1 Preview

This report includes a comparative study of Td-WTe_2 as an electrode material for sodium-ion and potassium-ion batteries. Results presented herein show that potassium-ion battery (larger radius ion) outperforms the SIB in terms of rate capability and cycling stability. Findings corroborate the potential of semimetal electrode materials and highlight that a battery characterization only based on certain parameters may lead to misleading results. Research opportunities for the next generation of alternative metal-ion technologies are also presented.

5.2 Introduction

Recently, WTe_2 has received considerable attention in the research community due to unique properties, such as large non-saturating magnetoresistance up to 60 T at 0.53 K[260], Weyl

semi-metallicity[261], nonlinear Hall effect[262;263], intriguing electronic properties[264] – which include metallic ferroelectricity at room temperature[265;266] – pressure-dependent superconductivity[267], polymorphism[232], and temperature-driven phase transition from Td to 1T′ phases[268;269]. As with other TMDs, the crystal structure of the TMD has an intrinsic relation with the TMDs' electronic and electrochemical properties. Although LIB report on Td-WTe_2[270], SIB on 1T′-WTe_2[72], and KIB on Td-WTe_2[96] have recently been published, this research is the first work on Td-WTe_2 SIB. To study high-performance cells, this work employed an electrolyte species that yields the highest mobility of Na^+ and K^+ in SIB and KIB, respectively[26]. Here we compared SIB and KIB using the semimetal TMD Td-WTe_2 as electrode material. Results of this work indicate that assumptions based only on ionic radius and sluggish diffusion in solids may be misleading owing to complexity of electrochemical systems.

5.3 Experimental

5.3.1 Material preparation

To prepare the electrodes, 70 wt.% of WTe_2 powder as received (Ossila, 99.9+%), 15 wt.% of carbon black (Alfa Aesar, 99.9+%), and 15 wt.% of poly(vinylidene fluoride) (Alfa Aesar) were mixed with a few drops of 1-methyl-2-pyrrolidinone (Sigma Aldrich) until a homogeneous slurry was obtained. The slurry was then cast onto a copper foil and dried at 80 °C overnight. Half-cells were assembled in an argon-filled glovebox using coin cell (CR2032) in which a WTe_2 electrode was used in one side of the cell, and a sodium- or potassium-metal electrode was placed on the other side of the cell for an SIB or KIB, respectively. A glass separator (Celgard), which was placed in between the electrodes, was soaked in either 1 M KPF_6 for a KIB or 1 M $NaClO_4$ for an SIB in (1:1 v:v) EC:PC (99%, Alfa Aesar). All reported chemicals were used as received without further purification.

5.4 Results and discussion

Figure 5.1(a,b) shows TEM images of the layered morphology of pristine WTe_2, while figure 5.1(c) shows the SAED. This diffraction pattern is characteristic of space group $Pmn2_1$; thus corresponding to Td-WTe_2[227]. A detailed discussion of WTe_2 Td and 1T′ crystal structures is reported elsewhere[96]. Figure 5.1(d-f) show the elemental mapping from EDX corroborating that the material is pristine WTe_2.

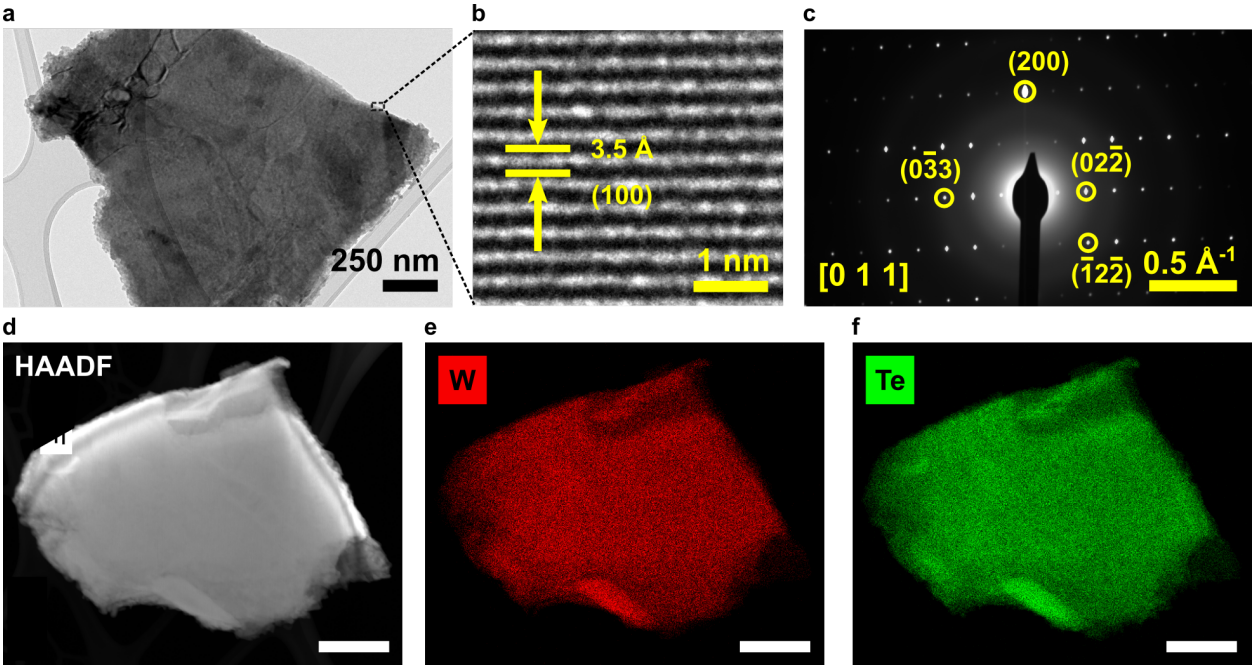

Figure 5.1: *Morphology characterization of Td-WTe_2. TEM images of (a) pristine Td-WTe_2 nanosheets, and (b) WTe_2 lattice fringes assigned to plane (100). (c) SAED image of pristine WTe_2 (ICSD collection code 259467). (d) HAADF. STEM showing (e) W, and (f) Te. Scale bars in d–f,* 300 nm.

Raman spectrum was performed to confirm that the studied WTe_2 had a Td phase, as shown in figure 5.2(a). This Raman spectrum exhibited high intensity peaks at 113, 118, 133, 164, and 213 cm^{-1}, which were assigned to vibrational modes A_2^4, A_1^3, A_1^4 A_1^7, , and A_1^9, respectively, and are ascribed to the Td phase[271]. Likewise, the XRD data shown in figure 5.2(b) corroborated the Td phase of WTe_2[228]. The Td-WTe_2 differed from the commonly reported semiconducting TMDs (e.g., 2H-MoS_2, 2H-$MoTe_2$, and 2H-WS_2) because the Td phase is semi-metallic[97;232;261]. Therefore, the higher electronic conductivity of the Td phase

makes Td-WTe_2 a promising active material for battery electrodes. The SIB and KIB reported herein were tested in half-cell configuration.

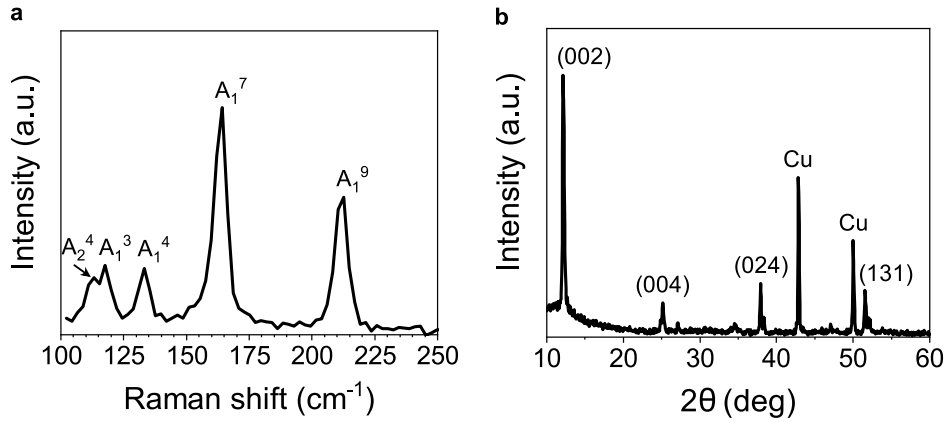

Figure 5.2: *Characterization of Td-WTe_2 electrode.(a) Raman spectrum. (b) XRD pattern of electrode material cast on copper foil current collector.*

Figure 5.3(a) and 5.3(b) show the SIB and KIB initial charge and discharge cycles, respectively. In the first cycle, the Coulombic efficiencies (CEs) of SIB and KIB were lower than 70%, which was attributed to irreversible SEI formation. The subsequent cycles, however, demonstrated higher efficiency values (i.e., Coulombic efficiency (CE) in the third cycle were 93% and 82% for SIB and KIB, respectively.

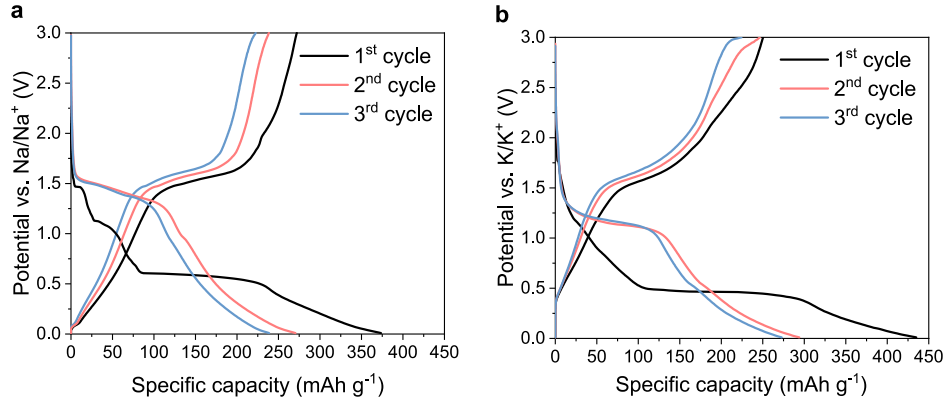

Figure 5.3: *Initial charge and discharge voltage profiles of Td-WTe_2 at* $50\,\mathrm{mA\,g^{-1}}$*: (a) SIB, (b) KIB.*

As shown in figure 5.3(a), although the SIB displayed a higher CE than the KIB, the specific charge capacity of the SIB decayed more rapidly, potentially due to the smaller Stokes' radius of potassium-ion (3.6 Å) in the PC compared to 4.6 Å of sodium-ion[218]. Kubota et al.[26]

concluded that potassium ions in PC have weaker Lewis acidity than Na^+ and Li^+, resulting in increased ionic conductivity and ion mobility of K^+ in the electrolyte. In addition, K^+ shows weaker solvation structure than Na^+ and Li^+ in EC, which led to a rapid diffusion of potassium ions in the electrolyte, indicating that the weaker solvent-ion interaction is more favorable towards enhanced rate capability performance of KIB[111;272].

To corroborate this initial finding, this study also investigated the rate capability performances of SIB and KIB at the current densities shown in figure 5.4(a). KIB exhibited more stable behavior than SIB, confirming that the smaller Stokes' radius of K^+ in PC enhances the carrier mobility of ions in the electrolyte. Overall, KIB also presented higher specific charge capacity than SIB after the initial cycles; this is a notable result owing to the larger Shannon's radius of K^+ (1.38 Å) in comparison with Na^+ (1.02 Å)[111;273]. Similarly, as shown in figure 5.4(b), the long-term cycling confirmed the higher stability of KIB. The potassium-ion cell showed 75% capacity retention from the 5^{th} cycle to the 50^{th} cycle, whereas the SIB showed 45% capacity retention for the same interval. To further understand the superiority of KIB it is necessary to look into the concept of desolvation energy of ions, as it presents direct influence in the insertion processes at the electrode and electrolyte interface[76]. In general, smaller desolvation energy yields high-power density battery electrodes. Sodium-ions show a relative high charge density around themselves in comparison with K^+. The higher charge density is because the smaller sodium-ions are stabilized by sharing or accepting electrons with or from solvated polar solvent molecules. As a result, sodium-ions present larger desolvation energy in PC (158.2 kJ mol^{-1}) versus of 119.2 kJ mol^{-1} of K^+ in PC[274]. In summary, although K^+ presents heavier atomic weight, the lower desolvation energy and higher molar ionic conductivity of K^+ (15.2 $\Omega^{-1}cm^2mol^{-1}$) versus Na^+ (9.1 $\Omega^{-1}cm^2mol^{-1}$)[275] in PC helps to explain why KIB outperforms SIB in rate capability and long-term tests depicted by figure 5.4(a) and figure 5.4(b), respectively.

Reaction kinetics of Td-WTe_2 for SIB and KIB were analyzed via GITT. Figure 5.5(a) and figure 5.5(b) present voltage profiles and reaction resistances of SIB and KIB, respectively. Potential response during GITT measurement of SIB and KIB are presented in figure 5.6(a) and figure 5.6(b), respectively. Initially, in figure 5.5(a), the SIB cell showed lower reaction

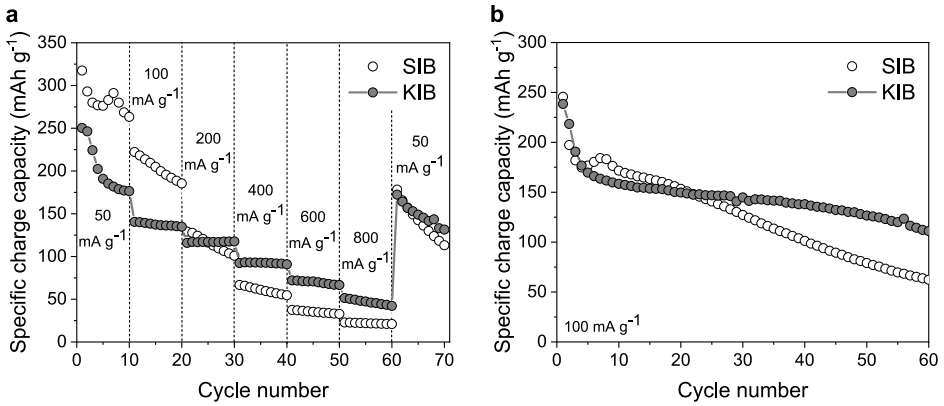

Figure 5.4: *(a) Rate capability test of Td-WTe_2 SIB and KIB, (b) Reversible de-sodiation and de-potassiation for 60 cycles.*

resistance because diffusion of Na^+ in solids was faster than of K^+ – owing to the lower Shannon's radius of Na^+[273]. From figure 5.3(a) one can see the plateau at 0.6 V vs. Na/Na^+ indicates a phase transition[276]. At this point a decrease in reaction resistance, i.e., from $\approx 0.4\,\Omega\,g$ to $0.2\,\Omega\,g$, can be an indicative that this phase transformation facilitated the insertion of Na^+. Nevertheless, as the phase transition continues to take place, the reaction resistance increases possibly due to accumulated stress in the Td-WTe_2 nanosheets arising from the continuous Na^+ insertion. In other words, this increased reaction resistance can be explained by the Na^+ longer diffusion length and repulsive forces among the Na^+ stored in Td-WTe_2 nanosheets[277]. As reported for other TMDs[109], at lower potentials conversion-type reactions are expected in Td-WTe_2 SIB. According to figure 5.4(a), Td-WTe_2 may store up to 5 Na^+ per unit formula; thus, showing evidence of a conversion-type reaction[107]. Moreover, during the conversion-type reaction Td-WTe_2 is reduced to a lower valence state species; thus, improving the electronic conductivity and reducing the overpotential[278]. As a result, this higher electronic conductivity yielded lower values of reaction resistance at a potential below 0.5 V vs. Na/Na^+. It is worth noting that the last data point shows an increase at the last step of Na^+ insertion – behavior similar to graphite insertion reported by C. Wang et al. in[279]; reasons for this latter behavior are presently unknown and could be the focus of future work. In the deintercalation step shown in figure 5.5(a), initially sodium-ions are extracted from the edges of Td-WTe_2; hence, displaying shorter transport path and

facilitated de-intercalation. These aspects altogether are assigned to the drop at reaction resistance observed. However, as the Na^+ extraction continues, the inherent shrinkage from this process results in decreased electronic conductivity of Td-WTe_2 nanosheets and current collector, again similarly to de-potassiation in graphite[74;280].

Concerning the KIB, as shown in figure 5.5(b), the initial slope area presented decrease on reaction resistance. Such initial decrease on reaction resistance can be ascribed to higher electronic conductivity due to volume expansion at lower intercalation levels. Upon volume expansion, Td-WTe_2 particles can be closer to each other; hence, enhancing the transport of electrons in the active material[74]. Further, in the plateau region – at approximately 0.47 V vs. K/K^+ – intercalation takes place as reported by Soares and Singh in[96]. The observed increase in the reaction resistance, i.e., from $\approx 3\,\Omega\,g$ to $\approx 5.1\,\Omega\,g$ was assigned to accumulated stress and strain and higher diffusion pathways for K^+ during the phase transformation. Subsequently, at the slope region the reaction resistance is again reduced due to the higher electronic conductivity achieved in the conversion-type reaction due to reduction of W^{4+} to W^0[278]. Regarding the charging cycle of KIB, similar to graphite[74], upon de-potassiation the reaction resistance is initially lower but increases as K^+ extraction process evolves. The initial low reaction resistance displayed in figure 5.5(b) can be assigned to a shorter transport distance, because initially K^+ are extracted from in the edges of Td-WTe_2 – similar to SIB. Moreover, as the extraction process continues, larger transport distances are expected to yield higher reaction resistance values.

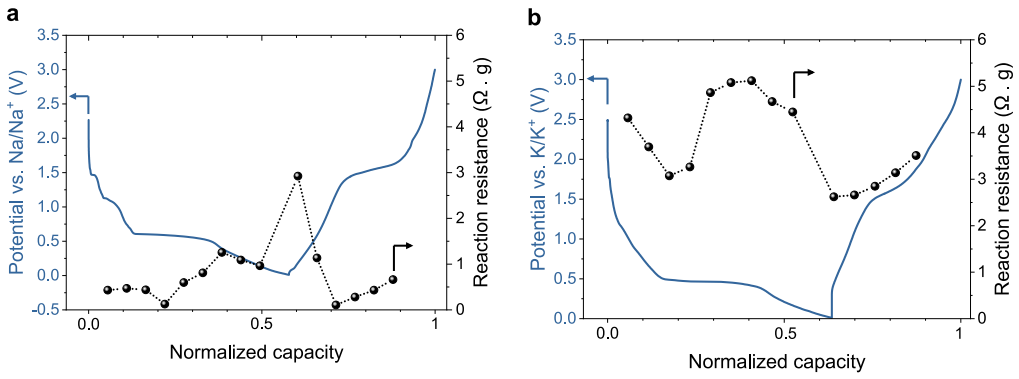

Figure 5.5: *Quasi-thermodynamically equilibrium potential profiles with respective reaction resistance values of Td-WTe_2: (a) SIB, (b) KIB half-cells.*

In summary, the higher values of reaction resistance of KIB observed in figure 5.5(b) are result of the higher overpotential of KIB, exhibited in figure 5.6(b), in comparison with SIB (figure 5.6(a)). The higher overpotential of KIB shows that K^+ diffusion is not as fast as Na^+ in Td-WTe_2[281]. In other words, although potassium ions exhibit high ion mobility in the EC:PC based-electrolyte, they present lower diffusivity in solids, resulting in a limited reaction kinetics. This finding was confirmed by Zhang et al.[218].

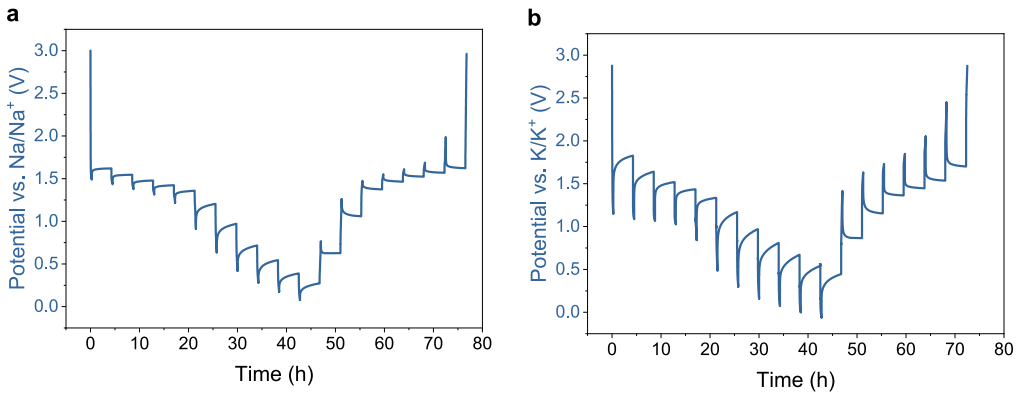

Figure 5.6: *Potential response during GITT measurement conducted at current pulses of* $100\,mA\,g^{-1}$ *for 15 minutes followed by relaxation for 4 hours of Td-*WTe_2*: (a) SIB, and (b) KIB half-cells.*

Another hypothesis that may explain the more prominent capacity fade of Td-WTe_2-SIB is that despite the smaller ionic radius and higher diffusion coefficient of Na^+ in Td-WTe_2, a continuous irreversible conversion-type reaction may lead to loss of active material. This behavior has also been reported for metal sulfides[282]. Furthermore, continuous electrolyte decomposition during cycling may contribute to the capacity fade process at a certain degree. These hypotheses could be the focus of investigation in future work.

5.5 Conclusion

This study reports Td-WTe_2 as active electrode material for SIB and KIB half-cells. As the first report on Na+ storage in Td-WTe_2, this work shows that despite the larger ionic radius of K^+, orthorhombic non-centrosymmetric phase of WTe_2 exhibited higher rate capability and cycling stability in PC-based electrolyte in comparison with SIB. Based on the

electrochemical studies, we found that although KIB showed higher overpotential in GITT measurement, higher reaction resistance, and larger Shannon's ionic radius, K^+ also presented higher mobility in the electrolyte medium owing to the smaller Stokes' radius in PC. Thus, the selection of suitable electrolyte medium is deemed as a crucial factor for the superior electrochemical performance of Td-WTe_2 as active electrode in KIB over SIB. This work is expected to open new avenues for study of TMD materials beyond the ordinary semiconducting species as electrode materials for alternative technologies to LIB.

Chapter 6

Conclusion and future work

6.1 Summary

This thesis presents contributions to development of high capacity KIB and SIB (also known as beyond LIB) electrodes comprising of polymorph layered TMDs. Firstly, it presents a detailed electrochemical property comparison of group VI layered TMDs of the sulfide and telluride types, which revealed two aspects: i. high charge capacity of MoS_2 and ii. capacity decay over long term cycling irrespective of the TMD type. The thesis then addresses the capacity decay issue by synthesizing a new type of composite TMD material. This composite material, named MoS_2-SiOC, was synthesized to address the poor stability of MoS_2 upon Na^+ storage. This stability issue is TMDs an open problem that previously led researchers to abandon research on layered TMDs for energy storage applications decades ago. Additionally, the thesis explores use of TMDs as electrodes for KIBs. Here, telluride-based TMD was found to offer superior charge capacity. WTe_2 showed superior cycling stability with K^+.

Regarding the organization of this thesis, chapter 1 intends to inform researchers, students, and enthusiasts about the direct implication of using fossil fuels in CO_2 emissions and the current challenges of reducing such emissions given the predicted population increase. The desired and environment-friendly approach of increasing participation of renewables in energy matrices to replace fossil fuels is also discussed, along with the challenges it brings.

Then, using a didactic approach, the concept of electrochemical energy storage is explained and its correlation to address challenges of renewables exploitation. Moreover, discussion on LIBs is presented and how the world economy and multi-billion dollar industries can be affected by the scarcity of lithium metal in the forthcoming decades. Lastly, chapter 1 introduces the beyond LIB technologies reported in this thesis and the motivation for studying these technologies.

Chapter 2, using a more technical approach, introduces concepts of alkali-ion battery technologies, i.e., SIB and KIB, and electronic and crystal properties of the sulfide- (MoS_2) and telluride-based (WTe_2) – TMDs studied as battery electrode materials in this thesis. In addition, a discussion of PDC materials is presented, as this material served as mitigation agent of sulfide dissolution of MoS_2 – work discussed in chapter 3. Also, this chapter aims to elucidate the relevant techniques used to characterize the materials presented in chapter 2, and the electrochemical performance of these materials when studied as battery electrodes.

Chapter 3 demonstrated a mechanism that mitigated suppressed regeneration of MoS_2 using silicon oxycarbide (SiOC). A facile functionalization process is introduced, which did not alter the 2H crystal structure of MoS_2 and yielded a uniform distribution of SiOC on the surface of MoS_2 nanosheets – aspect confirmed by microscopy, Raman, and XPS characterizations. Studied as a SIB electrode, electrochemical characterizations showed that the composite material MoS_2-SiOC presented higher stability upon cycling in comparison with pristine MoS_2; hence, MoS_2-SiOC composite electrode fulfilled its role in preventing sulfide dissolution. Further, EIS corroborated that the higher performance upon rate capability test of MoS_2-SiOC was due to enhanced electronic conductivity from sp^2 free-carbon domains of amorphous SiOC molecule. In summary, MoS_2-SiOC presented facile synthesis, stable electrochemical performance – confirmed by capacity retention of 86.5% after 100 cycles in rate capability test – and lower electronic resistance of MoS_2-SiOC electrode – confirmed by R_e 42% lower than pristine MoS_2.

Chapter 4 unveiled the K^+ storage mechanism in layered Td-WTe_2 – a semimetal, and polymorph TMD whose unconventional electronic structure is still under investigation by the academic community. Results showed that WTe_2 presented in the 1^{st} cycle charge capac-

ity 3.3 K^+ stored per molecule. Further, after 10 GCD cycles at 100 $mA\,g^{-1}$, WTe_2 presented stable charge capacity of 143 $mA\,h\,g^{-1}$; thus, outperforming 2H-WS_2 (66 $mA\,h\,g^{-1}$) and graphite (95 $mA\,h\,g^{-1}$) under the same conditions. Results in this work corroborated that the semimetallic phase Td and the larger interlayer spacing (c =14.07 Å) offered low charge transfer resistance and adequate distance to accommodate K^+, respectively. To shed light on K^+ storage process in WTe_2, a predicted storage mechanism is also presented, which was corroborated by the ex-situ post-cycling characterizations. It is also important to highlight that in this chapter a broader electrochemical discussion of EIS as a characterization technique is introduced. This discussion emphasizes that generalized equivalent circuit models published in the literature should be carefully analyzed for the system under consideration; thus, a principle known as Occam's razor should be applied. In a wider spectrum, the work presented in this chapter aims to bring attention to semimetal layered conversion-type TMD species for applications in EES.

Chapter 5 presented a comparative study of Td-WTe_2 as electrode material for SIB and KIB. This chapter demonstrated that although Na^+ radius is smaller than K^+ and WTe_2-SIB charge storage mechanism points towards conversion-type reaction, WTe_2-KIB presented higher rate capability and long-term cycling stability. Firstly, results showed that K^+ presented sluggish diffusion in WTe_2 electrode and limited kinetics – aspects confirmed by the higher overpotential in GITT. Yet this study showed that the concept of Stokes' radius plays a decisive role in the electrochemical performance. In other words, although K^+ presents larger atomic size and poorer diffusion in WTe_2, in PC electrolyte the Stokes' radius of K^+ is 3.6 Å versus 4.6 Å of Na^+. Therefore, in EC electrolyte potassium-ions have faster mobility, indicating that the the weaker solvent-ion interaction is decisive towards enhanced rate capability and stable cycling performance of WTe_2-KIB.

6.2 Future work

Although several findings have been observed during this research work, these results and conclusions comprise an initial report that aimed to evaluate stability during cycling of Na^+

and to assess the charge storage mechanisms of K^+ in layered sulfide- and telluride-based TMDs, respectively. Yet as fascinating materials, several research opportunities still exist. As such, further studies should be conducted in the areas summarized as follows.

1. MoS_2-SiOC showed improved stability upon cycling as SIB electrode. However, a prominent capacity decay still exists in initial cycles. Thus, future studies could be focused on the development of novel synthesis methods of MoS_2-SiOC composite material, or the study of other PDC materials that can be more effective in decreasing the observed initial capacity decay.

2. Likewise, there is room for studies of other PDC materials that may show capacity towards the alkali-ion under consideration. As a result, in addition to providing stability upon cycling, higher energy density materials could be achieved.

3. In-situ works are proven tools towards better understanding processes happening in electrode materials or electrode-electrolyte interface. In-situ XRD can assess how the interlayer spacing of 2H-MoS_2 or Td-WTe_2 is varying during charge and discharge of cells; in-situ Raman can provide information to better understand how SiOC improved the suppressed regeneration of MoS_2 by analyzing the electrolyte; likewise, in-situ Raman can be useful to understand whether a telluride-dissolution mechanism takes place upon cycling WTe_2 electrode; and in-situ TEM can assess whether SiOC acts as a buffer to accommodate expansion in MoS_2 during sodiation process.

4. Results presented in chapter 5 have shown that electrolytes play an important role in electrochemical performance. However, the commonly used salts and solvents may be obsolete due to their restricted variety. Hence, research focused on developing novel electrolytes is strongly encouraged as it may be a stepping-stone to layered TMDs as electrodes for beyond LIB.

5. Lastly, enabling TMDs as battery electrodes will also require innovative and scalable manufacturing methods to produce these electrodes. In this scenario, research on AM techniques is desirable as these techniques may produce electrodes in a scalable

way while addressing re-stacking or agglomeration issues by printing TMD 3D porous current collectors.

Bibliography

[1] Dominique Larcher and Jean-Marie Tarascon. Towards greener and more sustainable batteries for electrical energy storage. *Nature chemistry*, 7(1):19, 2015. ISSN 1755-4349.

[2] Bruce C. Gibb. The rise and rise of lithium. *Nature Chemistry*, 13(2):107–109. ISSN 1755-4349. doi: 10.1038/s41557-021-00638-w. URL https://doi.org/10.1038/s41557-021-00638-w.

[3] John B Goodenough. How we made the li-ion rechargeable battery. *Nature Electronics*, 1(3):204–204, 2018.

[4] Haegyeom Kim, Jae Chul Kim, Matteo Bianchini, Dong-Hwa Seo, Jorge Rodriguez-Garcia, and Gerbrand Ceder. Recent progress and perspective in electrode materials for K-ion batteries. *Advanced Energy Materials*, 8(9):1702384, 2018. ISSN 1614-6832. doi: 10.1002/aenm.201702384. URL https://onlinelibrary.wiley.com/doi/abs/10.1002/aenm.201702384.

[5] Jang Wook Choi and Doron Aurbach. Promise and reality of post-lithium-ion batteries with high energy densities. *Nature Reviews Materials*, 1(4):1 – 16, 2016. ISSN 20588437. doi: 10.1038/natrevmats.2016.13.

[6] Jang-Yeon Hwang, Seung-Taek Myung, and Yang-Kook Sun. Sodium-ion batteries: present and future. *Chemical Society Reviews*, 46(12):3529–3614, 2017.

[7] Bo Wang, Edison Huixiang Ang, Yang Yang, Yufei Zhang, Minghui Ye, Qi Liu, and Cheng Chao Li. Post-lithium-ion battery era: Recent advances in rechargeable potassium-ion batteries. *Chemistry–A European Journal*, 27(2):512–536, 2021.

[8] Christoph Vaalma, Daniel Buchholz, Marcel Weil, and Stefano Passerini. A cost and resource analysis of sodium-ion batteries. *Nature Reviews Materials*, 3(4):18013, 2018. ISSN 2058-8437.

[9] Hayley S Hirsh, Yixuan Li, Darren HS Tan, Minghao Zhang, Enyue Zhao, and Y Shirley Meng. Sodium-ion batteries paving the way for grid energy storage. *Advanced Energy Materials*, 10(32):2001274, 2020.

[10] David Linden and D Linden. *Handbook of batteries and fuel cells*. McGraw-Hill New York et al., 1984. ISBN 0070378746.

[11] J. M. Tarascon and M. Armand. Issues and challenges facing rechargeable lithium batteries. *Materials for Sustainable Energy: A Collection of Peer-Reviewed Research and Review Articles from Nature Publishing Group*, 414(November):171–179, 2010. doi: 10.1142/9789814317665_0024.

[12] Allen J Bard, Larry R Faulkner, et al. Fundamentals and applications. *Electrochemical Methods*, 2(482):580–632, 2001.

[13] Matthew Todd McDowell. *Understanding the electrochemical reaction of lithium with single silicon nanostructures*. Stanford University, 2013.

[14] M.Stanley Whittingham and Fred R. Gamble. The lithium intercalates of the transition metal dichalcogenides. *Materials Research Bulletin*, 10(5):363–371, 1975. ISSN 0025-5408. doi: https://doi.org/10.1016/0025-5408(75)90006-9. URL https://www.sciencedirect.com/science/article/pii/0025540875900069.

[15] Dingchang Lin, Yayuan Liu, and Yi Cui. Reviving the lithium metal anode for high-energy batteries. *Nature nanotechnology*, 12(3):194, 2017.

[16] Nobuyuki Imanishi, Mie Toyoda, Yasuo Takeda, and Osamu Yamamoto. Study on lithium intercalation into MoS_2. *Solid State Ionics*, 58(3):333–338, 1992. ISSN 0167-2738. doi: https://doi.org/10.1016/0167-2738(92)90137-E. URL https://www.sciencedirect.com/science/article/pii/016727389290137E.

[17] K. S. Novoselov, A. K. Geim, S. V. Morozov, D. Jiang, Y. Zhang, S. V. Dubonos, I. V. Grigorieva, and A. A. Firsov. Electric field effect in atomically thin carbon films. *Science*, 306(5696):666–669, 2004. ISSN 0036-8075. doi: 10.1126/science.1102896. URL https://science.sciencemag.org/content/306/5696/666.

[18] Shakir Bin Mujib, Zhongkan Ren, Santanu Mukherjee, Davi Marcelo Soares, and Gurpreet Singh. Design, characterization, and application of elemental 2d materials for electrochemical energy storage, sensing, and catalysis. *Materials Advances*, 1: 2562–2591, 2020. doi: 10.1039/D0MA00428F. URL http://dx.doi.org/10.1039/D0MA00428F.

[19] Ekaterina Pomerantseva and Yury Gogotsi. Two-dimensional heterostructures for energy storage. *Nature Energy*, 2(7):17089, 2017. ISSN 2058-7546. doi: 10.1038/nenergy.2017.89. URL https://doi.org/10.1038/nenergy.2017.89.

[20] M. S. Whittingham. Electrical energy storage and intercalation chemistry. *Science*, 192(4244):1126–1127, 1976. ISSN 0036-8075. doi: 10.1126/science.192.4244.1126. URL https://science.sciencemag.org/content/192/4244/1126.

[21] Matthew Li, Jun Lu, Xiulei Ji, Yanguang Li, Yuyan Shao, Zhongwei Chen, Cheng Zhong, and Khalil Amine. Design strategies for nonaqueous multivalent-ion and monovalent-ion battery anodes. *Nature Reviews Materials*, 5(4):276–294, 2020. ISSN 2058-8437. doi: 10.1038/s41578-019-0166-4. URL https://doi.org/10.1038/s41578-019-0166-4.

[22] Prabeer Barpanda, Gosuke Oyama, Shin-ichi Nishimura, Sai-Cheong Chung, and Atsuo Yamada. A 3.8-V earth-abundant sodium battery electrode. *Nature communications*, 5(1):1–8, 2014.

[23] Yang Wen, Kai He, Yujie Zhu, Fudong Han, Yunhua Xu, Isamu Matsuda, Yoshitaka Ishii, John Cumings, and Chunsheng Wang. Expanded graphite as superior anode for

sodium-ion batteries. 5(1):4033. ISSN 2041-1723. doi: 10.1038/ncomms5033. URL https://doi.org/10.1038/ncomms5033.

[24] Kunihiro Nobuhara, Hideki Nakayama, Masafumi Nose, Shinji Nakanishi, and Hideki Iba. First-principles study of alkali metal-graphite intercalation compounds. *Journal of Power Sources*, 243:585–587, 2013. ISSN 0378-7753. doi: https://doi.org/10.1016/j.jpowsour.2013.06.057. URL https://www.sciencedirect.com/science/article/pii/S0378775313010641.

[25] Zhaohui Wang, Sverre M. Selbach, and Tor Grande. Van der waals density functional study of the energetics of alkali metal intercalation in graphite. *RSC Advances*, 4: 4069–4079, 2014. doi: 10.1039/C3RA47187J. URL http://dx.doi.org/10.1039/C3RA47187J.

[26] Kei Kubota, Mouad Dahbi, Tomooki Hosaka, Shinichi Kumakura, and Shinichi Komaba. Towards K-ion and Na-ion batteries as "beyond li-ion". *The Chemical Record*, 18(4):459–479, 2018. ISSN 1527-8999. doi: https://doi.org/10.1002/tcr.201700057. URL https://doi.org/10.1002/tcr.201700057.

[27] Ziqi Guo, Shuoqing Zhao, Tiexin Li, Dawei Su, Shaojun Guo, and Guoxiu Wang. Recent advances in rechargeable magnesium-based batteries for high-efficiency energy storage. *Advanced Energy Materials*, 10(21):1903591, 2020.

[28] N. S. Gingrich and LeRoy Heaton. Structure of alkali metals in the liquid state. *The Journal of Chemical Physics*, 34(3):873–878, 1961. doi: 10.1063/1.1731688. URL https://doi.org/10.1063/1.1731688.

[29] Yikang Yu, Zhuoyue Wang, Zhen Hou, Wurui Ta, Wenhui Wang, Xixia Zhao, Qian Li, Yusheng Zhao, Qiangqiang Zhang, and Zewei Quan. 3 D printing of hierarchical graphene lattice for advanced Na metal anodes. *ACS Applied Energy Materials*, 2(5): 3869–3877, 2019. doi: 10.1021/acsaem.9b00540. URL https://doi.org/10.1021/acsaem.9b00540.

[30] Hongyan Kang, Yongchang Liu, Kangzhe Cao, Yan Zhao, Lifang Jiao, Yijing Wang, and Huatang Yuan. Update on anode materials for Na-ion batteries. *Journal of Materials Chemistry A*, 3:17899–17913, 2015. doi: 10.1039/C5TA03181H. URL http://dx.doi.org/10.1039/C5TA03181H.

[31] Yongchang Liu, Ning Zhang, Hongyan Kang, Minghui Shang, Lifang Jiao, and Jun Chen. WS_2 nanowires as a high-performance anode for sodium-ion batteries. *Chemistry – A European Journal*, 21(33):11878–11884, 2015. doi: https://doi.org/10.1002/chem.201501759. URL https://chemistry-europe.onlinelibrary.wiley.com/doi/abs/10.1002/chem.201501759.

[32] Takeshi Fujita, Yoshikazu Ito, Yongwen Tan, Hisato Yamaguchi, Daisuke Hojo, Akihiko Hirata, Damien Voiry, Manish Chhowalla, and Mingwei Chen. Chemically exfoliated ReS_2 nanosheets. *Nanoscale*, 6:12458–12462, 2014. doi: 10.1039/C4NR03740E. URL http://dx.doi.org/10.1039/C4NR03740E.

[33] Minglei Mao, Chunyu Cui, Mingguang Wu, Ming Zhang, Tao Gao, Xiulin Fan, Ji Chen, Taihong Wang, Jianmin Ma, and Chunsheng Wang. Flexible ReS_2 nanosheets/N-doped carbon nanofibers-based paper as a universal anode for alkali (Li, Na, K) ion battery. *Nano Energy*, 45:346–352, 2018. ISSN 2211-2855. doi: https://doi.org/10.1016/j.nanoen.2018.01.001. URL https://www.sciencedirect.com/science/article/pii/S2211285518300016.

[34] Biao Chen, Huan Li, Huaxiong Liu, Xinqian Wang, Fangxi Xie, Yida Deng, Wenbin Hu, Kenneth Davey, Naiqin Zhao, and Shi-Zhang Qiao. 1T′-ReS_2 confined in 2 D-honeycombed carbon nanosheets as new anode materials for high-performance sodium-ion batteries. *Advanced Energy Materials*, 9(30):1901146, 2019. doi: https://doi.org/10.1002/aenm.201901146. URL https://onlinelibrary.wiley.com/doi/abs/10.1002/aenm.201901146.

[35] T.B. Kim, J.W. Choi, H.S. Ryu, G.B. Cho, K.W. Kim, J.H. Ahn, K.K. Cho, and H.J. Ahn. Electrochemical properties of sodium/pyrite battery at room tempera-

ture. *Journal of Power Sources*, 174(2):1275–1278, 2007. ISSN 0378-7753. doi: https://doi.org/10.1016/j.jpowsour.2007.06.093. URL https://www.sciencedirect.com/science/article/pii/S0378775307012542. 13th International Meeting on Lithium Batteries.

[36] Davi Marcelo Soares and Gurpreet Singh. SiOC functionalization of MoS_2 as a means to improve stability as sodium-ion battery anode. *Nanotechnology*, 31(14):145403, 2020. ISSN 0957-4484 1361-6528. doi: 10.1088/1361-6528/ab6480. URL http://dx.doi.org/10.1088/1361-6528/ab6480.

[37] Marc Walter, Tanja Zünd, and Maksym V. Kovalenko. Pyrite (FeS_2) nanocrystals as inexpensive high-performance lithium-ion cathode and sodium-ion anode materials. *Nanoscale*, 7:9158–9163, 2015. doi: 10.1039/C5NR00398A. URL http://dx.doi.org/10.1039/C5NR00398A.

[38] Zhe Hu, Zhiqiang Zhu, Fangyi Cheng, Kai Zhang, Jianbin Wang, Chengcheng Chen, and Jun Chen. Pyrite FeS_2 for high-rate and long-life rechargeable sodium batteries. *Energy & Environmental Science*, 8:1309–1316, 2015. doi: 10.1039/C4EE03759F. URL http://dx.doi.org/10.1039/C4EE03759F.

[39] Fengbo Wang, Guangda Li, Xiangeng Meng, Yongxing Li, Qifa Gao, Yaqia Xu, and Wenfeng Cui. FeS_2 nanosheets encapsulated in 3D porous carbon spheres for excellent Na storage in sodium-ion batteries. *Inorganic Chemistry Frontiers*, 5:2462–2471, 2018. doi: 10.1039/C8QI00679B. URL http://dx.doi.org/10.1039/C8QI00679B.

[40] D. W. Murphy, C. Cros, F. J. Di Salvo, and J. V. Waszczak. Preparation and properties of Li_xVS_2 ($0 \leq x \leq 1$). *Inorganic Chemistry*, 16(12):3027–3031, 1977. doi: 10.1021/ic50178a008. URL https://doi.org/10.1021/ic50178a008.

[41] Junhua Zhou, Lu Wang, Mingye Yang, Jinghua Wu, Fengjiao Chen, Wenjing Huang, Na Han, Hualin Ye, Feipeng Zhao, Youyong Li, and Yanguang Li. Hierarchical VS_2 nanosheet assemblies: A universal host material for the reversible storage of alkali

metal ions. *Advanced Materials*, 29(35):1702061, 2017. ISSN 0935-9648. doi: 10.1002/adma.201702061. URL https://doi.org/10.1002/adma.201702061.

[42] Jianbiao Wang, Ningjing Luo, Junxiu Wu, Shuping Huang, Ling Yu, and Mingdeng Wei. Hierarchical spheres constructed by ultrathin VS_2 nanosheets for sodium-ion batteries. *Journal of Materials Chemistry A*, 7:3691–3696, 2019. doi: 10.1039/C8TA11950C. URL http://dx.doi.org/10.1039/C8TA11950C.

[43] Baihua Qu, Chuze Ma, Ge Ji, Chaohe Xu, Jing Xu, Ying Shirley Meng, Taihong Wang, and Jim Yang Lee. Layered SnS_2-reduced graphene oxide composite – a high-capacity, high-rate, and long-cycle life sodium-ion battery anode material. *Advanced Materials*, 26(23):3854–3859, 2014. doi: https://doi.org/10.1002/adma.201306314. URL https://onlinelibrary.wiley.com/doi/abs/10.1002/adma.201306314.

[44] Petr V. Prikhodchenko, Denis Y. W. Yu, Sudip K. Batabyal, Vladimir Uvarov, Jenny Gun, Sergey Sladkevich, Alexey A. Mikhaylov, Alexander G. Medvedev, and Ovadia Lev. Nanocrystalline tin disulfide coating of reduced graphene oxide produced by the peroxostannate deposition route for sodium ion battery anodes. *Journal of Materials Chemistry A*, 2:8431–8437, 2014. doi: 10.1039/C3TA15248K. URL http://dx.doi.org/10.1039/C3TA15248K.

[45] Yuhan Liu, Xin-Yao Yu, Yongjin Fang, Xiaoshu Zhu, Jianchun Bao, Xiaosi Zhou, and Xiong Wen (David) Lou. Confining SnS_2 ultrathin nanosheets in hollow carbon nanostructures for efficient capacitive sodium storage. *Joule*, 2(4):725–735, 2018. ISSN 2542-4351. doi: https://doi.org/10.1016/j.joule.2018.01.004. URL https://www.sciencedirect.com/science/article/pii/S2542435118300047.

[46] Yandong Zhang, Peiyi Zhu, Liliang Huang, Jian Xie, Shichao Zhang, Gaoshao Cao, and Xinbing Zhao. Few-layered SnS_2 on few-layered reduced graphene oxide as na-ion battery anode with ultralong cycle life and superior rate capability. *Advanced Functional Materials*, 25(3):481–489, 2015. doi: https://doi.org/10.1002/adfm.201402833. URL https://onlinelibrary.wiley.com/doi/abs/10.1002/adfm.201402833.

[47] Emery Brown, Pengli Yan, Halil Tekik, Ayyappan Elangovan, Jian Wang, Dong Lin, and Jun Li. 3 D printing of hybrid MoS_2-graphene aerogels as highly porous electrode materials for sodium ion battery anodes. *Materials & Design*, 170:107689, 2019. ISSN 0264-1275. doi: https://doi.org/10.1016/j.matdes.2019.107689. URL https://www.sciencedirect.com/science/article/pii/S0264127519301261.

[48] Patrice Simon and Yury Gogotsi. Perspectives for electrochemical capacitors and related devices. *Nature Materials*, 19(11):1151 – 1163. ISSN 1476-4660. doi: 10.1038/s41563-020-0747-z. URL https://doi.org/10.1038/s41563-020-0747-z.

[49] Michael P. Down, Emiliano Martínez-Perinan, Christopher W. Foster, Encarnacion Lorenzo, G. C. Smith, and Craig E. Banks. Next-generation additive manufacturing of complete standalone sodium-ion energy storage architectures. *Advanced Energy Materials*, 9(11):1803019, 2019. doi: https://doi.org/10.1002/aenm.201803019. URL https://onlinelibrary.wiley.com/doi/abs/10.1002/aenm.201803019.

[50] Marzieh Barghamadi, Ajay Kapoor, and Cuie Wen. A review on Li-S batteries as a high efficiency rechargeable lithium battery. *Journal of The Electrochemical Society*, 160(8):A1256–A1263, 2013. doi: 10.1149/2.096308jes. URL https://doi.org/10.1149/2.096308jes.

[51] Y. N. Ko, S. H. Choi, S. B. Park, and Y. C. Kang. Hierarchical $MoSe_2$ yolk–shell microspheres with superior Na-ion storage properties. *Nanoscale*, 6:10511–10515, 2014. doi: 10.1039/C4NR02538E. URL http://dx.doi.org/10.1039/C4NR02538E.

[52] Hui Wang, Xinzheng Lan, Danlu Jiang, Yan Zhang, Honghai Zhong, Zhongping Zhang, and Yang Jiang. Sodium storage and transport properties in pyrolysis synthesized $MoSe_2$ nanoplates for high performance sodium-ion batteries. *Journal of Power Sources*, 283:187–194, 2015. ISSN 0378-7753. doi: https://doi.org/10.1016/j.jpowsour.2015.02.096. URL https://www.sciencedirect.com/science/article/pii/S0378775315003304.

[53] Xu Zhao, Wei Cai, Ying Yang, Xuedan Song, Zachary Neale, Hong-En Wang, Jiehe Sui, and Guozhong Cao. $MoSe_2$ nanosheets perpendicularly grown on graphene with Mo-C bonding for sodium-ion capacitors. *Nano Energy*, 47:224–234, 2018. ISSN 2211-2855. doi: https://doi.org/10.1016/j.nanoen.2018.03.002. URL https://www.sciencedirect.com/science/article/pii/S2211285518301319.

[54] Fan Zhang, Chuan Xia, Jiajie Zhu, Bilal Ahmed, Hanfeng Liang, Dhinesh Babu Velusamy, Udo Schwingenschlögl, and Husam N. Alshareef. $SnSe_2$ 2 D anodes for advanced sodium ion batteries. *Advanced Energy Materials*, 6(22):1601188, 2016. doi: https://doi.org/10.1002/aenm.201601188. URL https://onlinelibrary.wiley.com/doi/abs/10.1002/aenm.201601188.

[55] Fen Zhang, Yu Shen, Meng Shao, Yongcai Zhang, Bing Zheng, Jiansheng Wu, Weina Zhang, Aiping Zhu, Fengwei Huo, and Sheng Li. $SnSe_2$ nanoparticles chemically embedded in a carbon shell for high-rate sodium-ion storage. *ACS Applied Materials & Interfaces*, 12(2):2346–2353, 2020. doi: 10.1021/acsami.9b16659. URL https://doi.org/10.1021/acsami.9b16659. PMID: 31877012.

[56] Keith Share, John Lewis, Landon Oakes, Rachel E. Carter, Adam P. Cohn, and Cary L. Pint. Tungsten diselenide (WSe_2) as a high capacity, low overpotential conversion electrode for sodium ion batteries. *RSC Advances*, 5:101262–101267, 2015. doi: 10.1039/C5RA19717A. URL http://dx.doi.org/10.1039/C5RA19717A.

[57] Zhian Zhang, Xing Yang, and Yun Fu. Nanostructured WSe_2/C composites as anode materials for sodium-ion batteries. *RSC Advances*, 6:12726–12729, 2016. doi: 10.1039/C5RA25645C. URL http://dx.doi.org/10.1039/C5RA25645C.

[58] Tiefeng Liu, Yaping Zhang, Zhanguo Jiang, Xianqing Zeng, Jiapeng Ji, Zeheng Li, Xuehui Gao, Minghao Sun, Zhan Lin, Min Ling, Junchao Zheng, and Chengdu Liang. Exploring competitive features of stationary sodium ion batteries for electrochemical energy storage. *Energy Environ. Sci.*, 12:1512–1533, 2019. doi: 10.1039/C8EE03727B. URL http://dx.doi.org/10.1039/C8EE03727B.

[59] Oleg V. Yazyev and Andras Kis. MoS_2 and semiconductors in the flatland. *Materials Today*, 18(1):20–30, 2015. ISSN 1369-7021. doi: https://doi.org/10.1016/j.mattod.2014.07.005. URL https://www.sciencedirect.com/science/article/pii/S1369702114002557.

[60] Haegyeom Kim, Jihyun Hong, Young-Uk Park, Jinsoo Kim, Insang Hwang, and Kisuk Kang. Sodium storage behavior in natural graphite using ether-based electrolyte systems. *Advanced Functional Materials*, 25(4):534–541, 2015. doi: https://doi.org/10.1002/adfm.201402984. URL https://onlinelibrary.wiley.com/doi/abs/10.1002/adfm.201402984.

[61] Adam P. Cohn, Keith Share, Rachel Carter, Landon Oakes, and Cary L. Pint. Ultrafast solvent-assisted sodium ion intercalation into highly crystalline few-layered graphene. *Nano Letters*, 16(1):543–548, 2016. doi: 10.1021/acs.nanolett.5b04187. URL https://doi.org/10.1021/acs.nanolett.5b04187. PMID: 26618985.

[62] Yaochen Song, Jiaxuan Liao, Cheng Chen, Jian Yang, Jinchen Chen, Feng Gong, Sizhe Wang, Ziqiang Xu, and Mengqiang Wu. Controllable morphologies and electrochemical performances of self-assembled nano-honeycomb WS_2 anodes modified by graphene doping for lithium and sodium ion batteries. *Carbon*, 142:697–706, 2019. ISSN 0008-6223. doi: https://doi.org/10.1016/j.carbon.2018.07.060. URL https://www.sciencedirect.com/science/article/pii/S0008622318307103.

[63] Anna Douglas, Rachel Carter, Landon Oakes, Keith Share, Adam P. Cohn, and Cary L. Pint. Ultrafine iron pyrite (FeS_2) nanocrystals improve sodium–sulfur and lithium–sulfur conversion reactions for efficient batteries. *ACS Nano*, 9(11):11156–11165, 2015. doi: 10.1021/acsnano.5b04700. URL https://doi.org/10.1021/acsnano.5b04700. PMID: 26529682.

[64] Yiben Shao, Jili Yue, Shuo Sun, and Hui Xia. Facile synthesis of FeS_2 quantum-dots/functionalized graphene-sheet composites as advanced anode material for sodium-ion batteries. *Chinese Journal of Chemistry*, 35(1):73–78, 2017. doi: https://doi.

org/10.1002/cjoc.201600637. URL https://onlinelibrary.wiley.com/doi/abs/10.1002/cjoc.201600637.

[65] Shiwen Wang, Yaping Jing, Lifeng Han, Heng Wang, Shide Wu, Yong Zhang, Lizhen Wang, Kai Zhang, Yong-Mook Kang, and Fangyi Cheng. Ultrathin carbon-coated FeS_2 nanooctahedra for sodium storage with long cycling stability. *Inorganic Chemistry Frontiers*, 6:459–464, 2019. doi: 10.1039/C8QI01144C. URL http://dx.doi.org/10.1039/C8QI01144C.

[66] Yongchang Liu, Hongyan Kang, Lifang Jiao, Chengcheng Chen, Kangzhe Cao, Yijing Wang, and Huatang Yuan. Exfoliated-SnS_2 restacked on graphene as a high-capacity, high-rate, and long-cycle life anode for sodium ion batteries. *Nanoscale*, 7:1325–1332, 2015. doi: 10.1039/C4NR05106H. URL http://dx.doi.org/10.1039/C4NR05106H.

[67] Wenping Sun, Xianhong Rui, Dan Yang, Ziqi Sun, Bing Li, Wenyu Zhang, Yun Zong, Srinivasan Madhavi, Shixue Dou, and Qingyu Yan. Two-dimensional tin disulfide nanosheets for enhanced sodium storage. *ACS Nano*, 9(11):11371–11381, 2015. doi: 10.1021/acsnano.5b05229. URL https://doi.org/10.1021/acsnano.5b05229. PMID: 26487194.

[68] Shi Tao, Dajun Wu, Shuangming Chen, Bin Qian, Wangsheng Chu, and Li Song. A versatile strategy for ultrathin SnS_2 nanosheets confined in a n-doped graphene sheet composite for high performance lithium and sodium-ion batteries. *Chemical Communications*, 54:8379–8382, 2018. doi: 10.1039/C8CC04255A. URL http://dx.doi.org/10.1039/C8CC04255A.

[69] Hongwei Tao, Min Zhou, Ruxing Wang, Kangli Wang, Shijie Cheng, and Kai Jiang. TiS_2 as an advanced conversion electrode for sodium-ion batteries with ultra-high capacity and long-cycle life. *Advanced Science*, 5(11):1801021, 2018. doi: https://doi.org/10.1002/advs.201801021. URL https://onlinelibrary.wiley.com/doi/abs/10.1002/advs.201801021.

[70] Zhian Zhang, Xing Yang, Yun Fu, and Ke Du. Ultrathin molybdenum diselenide nanosheets anchored on multi-walled carbon nanotubes as anode composites for high performance sodium-ion batteries. *Journal of Power Sources*, 296:2–9, 2015. ISSN 0378-7753. doi: https://doi.org/10.1016/j.jpowsour.2015.07.008. URL https://www.sciencedirect.com/science/article/pii/S0378775315300562.

[71] Manas Ranjan Panda, Anish Raj K, Arnab Ghosh, Ajit Kumar, Divyamahalakshmi Muthuraj, Supriya Sau, Wenzhi Yu, Yupeng Zhang, A.K. Sinha, Matthew Weyland, Qiaoliang Bao, and Sagar Mitra. Blocks of molybdenum ditelluride: A high rate anode for sodium-ion battery and full cell prototype study. *Nano Energy*, 64:103951, 2019. ISSN 2211-2855. doi: https://doi.org/10.1016/j.nanoen.2019.103951. URL https://www.sciencedirect.com/science/article/pii/S2211285519306585.

[72] Meiling Hong, Jie Li, Wenfeng Zhang, Shantang Liu, and Haixin Chang. Semimetallic 1T′ WTe_2 nanorods as anode material for the sodium ion battery. *Energy & Fuels*, 32(5):6371–6377, 2018. ISSN 0887-0624. doi: 10.1021/acs.energyfuels.8b00454. URL https://doi.org/10.1021/acs.energyfuels.8b00454.

[73] Tomooki Hosaka, Kei Kubota, A. Shahul Hameed, and Shinichi Komaba. Research development on K-ion batteries. *Chemical Reviews*, 120(14):6358–6466, 2020. doi: 10.1021/acs.chemrev.9b00463. URL https://doi.org/10.1021/acs.chemrev.9b00463. PMID: 31939297.

[74] Jin Zhao, Xiaoxi Zou, Yujie Zhu, Yunhua Xu, and Chunsheng Wang. Electrochemical intercalation of potassium into graphite. *Advanced Functional Materials*, 26(44):8103–8110, 2016. doi: 10.1002/adfm.201602248.

[75] Masaki Okoshi, Yuki Yamada, Shinichi Komaba, Atsuo Yamada, and Hiromi Nakai. Theoretical analysis of interactions between potassium ions and organic electrolyte solvents: a comparison with lithium, sodium, and magnesium ions. *Journal of The Electrochemical Society*, 164(2):A54, 2016.

[76] Naoaki Yabuuchi, Kei Kubota, Mouad Dahbi, and Shinichi Komaba. Research development on sodium-ion batteries. *Chemical Reviews*, 114(23):11636–11682, 2014. doi: 10.1021/cr500192f. URL https://doi.org/10.1021/cr500192f. PMID: 25390643.

[77] Shinichi Komaba, Tatsuya Hasegawa, Mouad Dahbi, and Kei Kubota. Potassium intercalation into graphite to realize high-voltage/high-power potassium-ion batteries and potassium-ion capacitors. *Electrochemistry Communications*, 60:172–175, 2015. ISSN 1388-2481. doi: https://doi.org/10.1016/j.elecom.2015.09.002. URL https://www.sciencedirect.com/science/article/pii/S1388248115002465.

[78] Y Marcus. Thermodynamic functions of transfer of single ions from water to nonaqueous and mixed solvents: Part 3-standard potentials of selected electrodes. *Pure and applied chemistry*, 57(8):1129–1132, 1985.

[79] Jang-Yeon Hwang, Seung-Taek Myung, and Yang-Kook Sun. Recent progress in rechargeable potassium batteries. *Advanced Functional Materials*, 28(43):1802938, 2018. doi: https://doi.org/10.1002/adfm.201802938. URL https://onlinelibrary.wiley.com/doi/abs/10.1002/adfm.201802938.

[80] V. Lakshmi, Ying Chen, Alexey A. Mikhaylov, Alexander G. Medvedev, Irin Sultana, Md Mokhlesur Rahman, Ovadia Lev, Petr V. Prikhodchenko, and Alexey M. Glushenkov. Nanocrystalline SnS_2 coated onto reduced graphene oxide: demonstrating the feasibility of a non-graphitic anode with sulfide chemistry for potassium-ion batteries. *Chemical Communications*, 53(59):8272–8275, 2017. ISSN 1359-7345. doi: 10.1039/C7CC03998K. URL http://dx.doi.org/10.1039/C7CC03998K.

[81] Xiaofei Bie, Kei Kubota, Tomooki Hosaka, Kuniko Chihara, and Shinichi Komaba. A novel K-ion battery: hexacyanoferrate(ii)/graphite cell. *Journal of Materials Chemistry A*, 5:4325–4330, 2017. doi: 10.1039/C7TA00220C. URL http://dx.doi.org/10.1039/C7TA00220C.

[82] Michael Thackeray. Lithium-ion batteries: An unexpected conductor. *Nature ma-*

terials, 1(2):81–82, 2002. ISSN 1476-4660. doi: 10.1038/nmat736. URL https://doi.org/10.1038/nmat736.

[83] Wei Wang, Bo Jiang, Chang Qian, Fan Lv, Jianrui Feng, Jinhui Zhou, Kai Wang, Chao Yang, Yong Yang, and Shaojun Guo. Pistachio-shuck-like $MoSe_2$/C core/shell nanostructures for high-performance potassium-ion storage. *Advanced Materials*, 30 (30):1801812, 2018. ISSN 0935-9648. doi: 10.1002/adma.201801812. URL https://onlinelibrary.wiley.com/doi/abs/10.1002/adma.201801812.

[84] JunMin Ge, Ling Fan, Jue Wang, Qingfeng Zhang, Zhaomeng Liu, Erjin Zhang, Qian Liu, Xinzhi Yu, and Bingan Lu. $MoSe_2$/N-doped carbon as anodes for potassium-ion batteries. *Advanced Energy Materials*, 8(29):1801477, 2018. ISSN 1614-6832. doi: 10.1002/aenm.201801477. URL https://onlinelibrary.wiley.com/doi/abs/10.1002/aenm.201801477.

[85] Yupeng Shen, Jie Liu, Xiaoyin Li, and Qian Wang. Two-dimensional T-$NiSe_2$ as a promising anode material for potassium-ion batteries with low average voltage, high ionic conductivity, and superior carrier mobility. *ACS Applied Materials & Interfaces*, 11(39):35661–35666, 2019. doi: 10.1021/acsami.9b09223. URL https://doi.org/10.1021/acsami.9b09223. PMID: 31532605.

[86] Chao Yang, Jianrui Feng, Fan Lv, Jinhui Zhou, Chunfu Lin, Kai Wang, Yelong Zhang, Yong Yang, Wei Wang, Jianbao Li, and Shaojun Guo. Metallic graphene-like VSe_2 ultrathin nanosheets: Superior potassium-ion storage and their working mechanism. *Advanced Materials*, 30(27):1800036, 2018. doi: https://doi.org/10.1002/adma.201800036. URL https://onlinelibrary.wiley.com/doi/abs/10.1002/adma.201800036.

[87] Jongwook W Heo, Munseok S Chae, Jooeun Hyoung, and Seung-Tae Hong. Rhombohedral potassium–zinc hexacyanoferrate as a cathode material for nonaqueous potassium-ion batteries. *Inorganic chemistry*, 58(5):3065–3072, 2019.

[88] Angel Kirchev. Battery management and battery diagnostics. In *Electrochemical Energy Storage for Renewable Sources and Grid Balancing*, pages 411–435. Elsevier, 2015.

[89] Leonardo M. Da Silva, Reinaldo Cesar, Cássio M. R. Moreira, Jéferson H. M. Santos, Lindomar G. De Souza, Bruno Morandi Pires, Rafael Vicentini, Willian Nunes, and Hudson Zanin. Reviewing the fundamentals of supercapacitors and the difficulties involving the analysis of the electrochemical findings obtained for porous electrode materials. *Energy Storage Materials*, 27:555–590, 2020. ISSN 2405-8297. doi: https://doi.org/10.1016/j.ensm.2019.12.015. URL http://www.sciencedirect.com/science/article/pii/S2405829719310931.

[90] Shangshang Wang, Jianbo Zhang, Oumaïma Gharbi, Vincent Vivier, Ming Gao, and Mark E. Orazem. Electrochemical impedance spectroscopy. *Nature Reviews Methods Primers*, 1(1):41. ISSN 2662-8449. doi: 10.1038/s43586-021-00039-w. URL https://doi.org/10.1038/s43586-021-00039-w.

[91] Andrzej Lasia. *Electrochemical impedance spectroscopy and its applications*, pages 143–248. Springer, 2002.

[92] Ruding Zhang, Jingze Bao, Yilong Pan, and Chuan-Fu Sun. Highly reversible potassium-ion intercalation in tungsten disulfide. *Chemical Science*, 10(9):2604–2612, 2019. ISSN 2041-6520. doi: 10.1039/C8SC04350G. URL http://dx.doi.org/10.1039/C8SC04350G.

[93] E. Deiss. Spurious chemical diffusion coefficients of Li^+ in electrode materials evaluated with GITT. *Electrochimica Acta*, 50(14):2927–2932, 2005. ISSN 0013-4686. doi: https://doi.org/10.1016/j.electacta.2004.11.042. URL https://www.sciencedirect.com/science/article/pii/S0013468604011600.

[94] Sajedeh Manzeli, Dmitry Ovchinnikov, Diego Pasquier, Oleg V. Yazyev, and Andras Kis. 2 D transition metal dichalcogenides. *Nature Reviews Materials*, 2(8):17033, 2017.

ISSN 2058-8437. doi: 10.1038/natrevmats.2017.33. URL https://doi.org/10.1038/natrevmats.2017.33.

[95] Davi Marcelo Soares, Santanu Mukherjee, and Gurpreet Singh. TMDs beyond MoS_2 for electrochemical energy storage. *Chemistry – A European Journal*, 26(29):6320–6341, 2020. doi: https://doi.org/10.1002/chem.202000147. URL https://chemistry-europe.onlinelibrary.wiley.com/doi/abs/10.1002/chem.202000147.

[96] Davi Marcelo Soares and Gurpreet Singh. Superior electrochemical performance of layered WTe_2 as potassium-ion battery electrode. *Nanotechnology*, 31(45):455406, 2020. ISSN 0957-4484 1361-6528. doi: 10.1088/1361-6528/ababcc. URL http://dx.doi.org/10.1088/1361-6528/ababcc.

[97] Manish Chhowalla, Hyeon Suk Shin, Goki Eda, Lain-Jong Li, Kian Ping Loh, and Hua Zhang. The chemistry of two-dimensional layered transition metal dichalcogenide nanosheets. *Nature chemistry*, 5(4):263, 2013. ISSN 1755-4349.

[98] Martin Pumera, Zdeněk Sofer, and Adriano Ambrosi. Layered transition metal dichalcogenides for electrochemical energy generation and storage. *Journal of Materials Chemistry A*, 2:8981–8987, 2014. doi: 10.1039/C4TA00652F. URL http://dx.doi.org/10.1039/C4TA00652F.

[99] Chintamani Nagesa Ramachandra Rao and Waghmare Umesh Vasudeo. *2D inorganic materials beyond graphene*. World Scientific, 2017. ISBN 1786342715.

[100] Damien Voiry, Aditya Mohite, and Manish Chhowalla. Phase engineering of transition metal dichalcogenides. *Chemical Society Reviews*, 44(9):2702–2712, 2015. ISSN 0306-0012. doi: 10.1039/C5CS00151J. URL http://dx.doi.org/10.1039/C5CS00151J.

[101] M. Acerce, D. Voiry, and M. Chhowalla. Metallic 1 T phase MoS_2 nanosheets as supercapacitor electrode materials. *Nature Nanotechnology*, 10(4):313–8, 2015. ISSN

1748-3395 (Electronic) 1748-3387 (Linking). doi: 10.1038/nnano.2015.40. URL https://www.ncbi.nlm.nih.gov/pubmed/25799518.

[102] Simone Bertolazzi, Jacopo Brivio, and Andras Kis. Stretching and breaking of ultrathin mos2. *ACS Nano*, 5(12):9703–9709, 2011. ISSN 1936-0851. doi: 10.1021/nn203879f. URL https://doi.org/10.1021/nn203879f.

[103] Tao Dong, Joao Simoes, and Zhaochu Yang. Flexible photodetector based on 2 D materials: Processing, architectures, and applications. *Advanced Materials Interfaces*, 7(4):1901657, 2020. ISSN 2196-7350. doi: 10.1002/admi.201901657. URL https://doi.org/10.1002/admi.201901657.

[104] D. A. Stevens and J. R. Dahn. The mechanisms of lithium and sodium insertion in carbon materials. *Journal of The Electrochemical Society*, 148(8):A803, 2001. doi: 10.1149/1.1379565. URL https://doi.org/10.1149/1.1379565.

[105] H. Shi, J. Barker, M.Y. Saïdi, R. Koksbang, and L. Morris. Graphite structure and lithium intercalation. *Journal of Power Sources*, 68(2):291–295, 1997. ISSN 0378-7753. doi: https://doi.org/10.1016/S0378-7753(96)02562-1. URL https://www.sciencedirect.com/science/article/pii/S0378775396025621. Proceedings of the Eighth International Meeting on Lithium Batteries.

[106] R. Yazami and Ph. Touzain. A reversible graphite-lithium negative electrode for electrochemical generators. *Journal of Power Sources*, 9(3):365–371, 1983. ISSN 0378-7753. doi: https://doi.org/10.1016/0378-7753(83)87040-2. URL https://www.sciencedirect.com/science/article/pii/0378775383870402.

[107] M. Armand and J. M. Tarascon. Building better batteries. *Nature*, 451(7179):652–657, 2008. ISSN 1476-4687. doi: 10.1038/451652a. URL https://doi.org/10.1038/451652a.

[108] M. Rosa Palacín. Recent advances in rechargeable battery materials: a chemist's

perspective. *Chemical Society Reviews*, 38(9):2565–2575, 2009. ISSN 0306-0012. doi: 10.1039/B820555H. URL http://dx.doi.org/10.1039/B820555H.

[109] Ramkrishna Sahoo, Monika Singh, and Tata Narasinga Rao. A review on the current progress and challenges of 2 D layered transition metal dichalcogenides (TMDs) as Li/Na-ion battery anode. *ChemElectroChem*, n/a(n/a). doi: https://doi.org/10.1002/celc.202100197. URL https://chemistry-europe.onlinelibrary.wiley.com/doi/abs/10.1002/celc.202100197.

[110] Zhongtao Ma, Zhenpeng Yao, Yingchun Cheng, Xuyang Zhang, Bingkun Guo, Yingchun Lyu, Peng Wang, Qianqian Li, Hongtao Wang, Anmin Nie, and Alán Aspuru-Guzik. All roads lead to rome: Sodiation of different-stacked SnS_2. *Nano Energy*, 67:104276, 2020. ISSN 2211-2855. doi: https://doi.org/10.1016/j.nanoen.2019.104276. URL https://www.sciencedirect.com/science/article/pii/S2211285519309838.

[111] Yuqi Li, Yaxiang Lu, Philipp Adelhelm, Maria-Magdalena Titirici, and Yong-Sheng Hu. Intercalation chemistry of graphite: alkali metal ions and beyond. *Chemical Society Reviews*, 48(17):4655–4687, 2019. ISSN 0306-0012. doi: 10.1039/C9CS00162J. URL http://dx.doi.org/10.1039/C9CS00162J.

[112] Martin Winter, Jürgen O. Besenhard, Michael E. Spahr, and Petr Novák. Insertion electrode materials for rechargeable lithium batteries. *Advanced Materials*, 10(10):725–763, 1998. doi: https://doi.org/10.1002/(SICI)1521-4095(199807)10:10⟨725::AID-ADMA725⟩3.0.CO;2-Z. URL https://onlinelibrary.wiley.com/doi/abs/10.1002/%28SICI%291521-4095%28199807%2910%3A10%3C725%3A%3AAID-ADMA725%3E3.0.CO%3B2-Z.

[113] Jiajie Pei, Jiong Yang, Tanju Yildirim, Han Zhang, and Yuerui Lu. Many-body complexes in 2 D semiconductors. *Advanced Materials*, 31(2):1706945, 2019. doi: https://doi.org/10.1002/adma.201706945. URL https://onlinelibrary.wiley.com/doi/abs/10.1002/adma.201706945.

[114] J.A. Wilson and A.D. Yoffe. The transition metal dichalcogenides discussion and interpretation of the observed optical, electrical and structural properties. *Advances in Physics*, 18(73):193–335, 1969. doi: 10.1080/00018736900101307. URL https://doi.org/10.1080/00018736900101307.

[115] Biplab Rajbanshi, Sunandan Sarkar, and Pranab Sarkar. The electronic and optical properties of $MoS_{2(1-x)}Se_{2x}$ and $MoS_{2(1-x)}Te_{2x}$ monolayers. *Physical Chemistry Chemical Physics*, 17:26166–26174, 2015. doi: 10.1039/C5CP04653J. URL http://dx.doi.org/10.1039/C5CP04653J.

[116] Edbert J. Sie, Clara M. Nyby, C. D. Pemmaraju, Su Ji Park, Xiaozhe Shen, Jie Yang, Matthias C. Hoffmann, B. K. Ofori-Okai, Renkai Li, Alexander H. Reid, Stephen Weathersby, Ehren Mannebach, Nathan Finney, Daniel Rhodes, Daniel Chenet, Abhinandan Antony, Luis Balicas, James Hone, Thomas P. Devereaux, Tony F. Heinz, Xijie Wang, and Aaron M. Lindenberg. An ultrafast symmetry switch in a weyl semimetal. *Nature*, 565(7737):61–66, 2019. ISSN 1476-4687. doi: 10.1038/s41586-018-0809-4. URL https://doi.org/10.1038/s41586-018-0809-4.

[117] Pierre Villars and Karin Cenzual, editors. *C Crystal Structure: Datasheet from " PAULING FILE Multinaries Edition – 2012 in SpringerMaterials*. Springer-Verlag Berlin Heidelberg & Material Phases Data System (MPDS), Switzerland & National Institute for Materials Science (NIMS), Japan. URL https://materials.springer.com/isp/crystallographic/docs/sd_0553644. Part of Springer Materials.

[118] Santanu Mukherjee, Zhongkan Ren, and Gurpreet Singh. Beyond graphene anode materials for emerging metal ion batteries and supercapacitors. *Nano-micro letters*, 10 (4):70, 2018.

[119] Zongyou Yin, Hai Li, Hong Li, Lin Jiang, Yumeng Shi, Yinghui Sun, Gang Lu, Qing Zhang, Xiaodong Chen, and Hua Zhang. Single-layer MoS_2 phototransistors. *ACS Nano*, 6(1):74–80, 2012. doi: 10.1021/nn2024557. URL https://doi.org/10.1021/nn2024557. PMID: 22165908.

[120] Valeria Nicolosi, Manish Chhowalla, Mercouri G Kanatzidis, Michael S Strano, and Jonathan N Coleman. Liquid exfoliation of layered materials. *Science*, 340(6139), 2013.

[121] Adriano Ambrosi, Zdeněk Sofer, and Martin Pumera. Lithium intercalation compound dramatically influences the electrochemical properties of exfoliated MoS_2. *Small*, 11(5):605–612, 2015. doi: https://doi.org/10.1002/smll.201400401. URL https://onlinelibrary.wiley.com/doi/abs/10.1002/smll.201400401.

[122] Jie Xiao, Daiwon Choi, Lelia Cosimbescu, Phillip Koech, Jun Liu, and John P. Lemmon. Exfoliated MoS_2 nanocomposite as an anode material for lithium ion batteries. *Chemistry of Materials*, 22(16):4522–4524, 2010. doi: 10.1021/cm101254j. URL https://doi.org/10.1021/cm101254j.

[123] Gyeong Sook Bang, Kwan Woo Nam, Jong Yun Kim, Jongwoo Shin, Jang Wook Choi, and Sung-Yool Choi. Effective liquid-phase exfoliation and sodium ion battery application of MoS_2 nanosheets. *ACS Applied Materials & Interfaces*, 6(10):7084–7089, 2014. doi: 10.1021/am4060222. URL https://doi.org/10.1021/am4060222. PMID: 24773226.

[124] L. David, R. Bhandavat, and G. Singh. MoS_2/graphene composite paper for sodium-ion battery electrodes. *ACS Nano*, 8(2):1759–70, 2014. ISSN 1936-086X (Electronic) 1936-0851 (Linking). doi: 10.1021/nn406156b. URL https://www.ncbi.nlm.nih.gov/pubmed/24446875.

[125] Thomas A. Empante, Yao Zhou, Velveth Klee, Ariana E. Nguyen, I-Hsi Lu, Michael D. Valentin, Sepedeh A. Naghibi Alvillar, Edwin Preciado, Adam J. Berges, Cindy S. Merida, Michael Gomez, Sarah Bobek, Miguel Isarraraz, Evan J. Reed, and Ludwig Bartels. Chemical vapor deposition growth of few-layer $MoTe_2$ in the 2 H, 1T′, and 1 T phases: Tunable properties of $MoTe_2$ films. *ACS Nano*, 11(1):900–905, 2017. doi: 10.1021/acsnano.6b07499. URL https://doi.org/10.1021/acsnano.6b07499. PMID: 27992719.

[126] Shusheng Xu, Xiaoming Gao, Yong Hua, Anne Neville, Yanan Wang, and Kan Zhang. Rapid deposition of WS_2 platelet thin films as additive-free anode for sodium ion batteries with superior volumetric capacity. *Energy Storage Materials*, 26:534–542, 2020. ISSN 2405-8297. doi: https://doi.org/10.1016/j.ensm.2019.11.026. URL https://www.sciencedirect.com/science/article/pii/S2405829719310736.

[127] Andrew J Mannix, Brian Kiraly, Mark C Hersam, and Nathan P Guisinger. Synthesis and chemistry of elemental 2 D materials. *Nature Reviews Chemistry*, 1(2):1–14, 2017.

[128] Qinbai Yun, Liuxiao Li, Zhaoning Hu, Qipeng Lu, Bo Chen, and Hua Zhang. Layered transition metal dichalcogenide-based nanomaterials for electrochemical energy storage. *Advanced Materials*, 32(1):1903826, 2020. doi: https://doi.org/10.1002/adma.201903826. URL https://onlinelibrary.wiley.com/doi/abs/10.1002/adma.201903826.

[129] Pratteek Das, Qiang Fu, Xinhe Bao, and Zhong-Shuai Wu. Recent advances in the preparation, characterization, and applications of two-dimensional heterostructures for energy storage and conversion. *Journal of Materials Chemistry A*, 6:21747–21784, 2018. doi: 10.1039/C8TA04618B. URL http://dx.doi.org/10.1039/C8TA04618B.

[130] Manish Chhowalla, Zhongfan Liu, and Hua Zhang. Two-dimensional transition metal dichalcogenide (TMD) nanosheets. *Chemical Society Reviews*, 44:2584–2586, 2015. doi: 10.1039/C5CS90037A. URL http://dx.doi.org/10.1039/C5CS90037A.

[131] Paolo Colombo, Gabriela Mera, Ralf Riedel, and Gian Domenico Soraru. Polymer-derived ceramics: 40 years of research and innovation in advanced ceramics. *Journal of the American Ceramic Society*, 93(7):1805 – 1837, 2010. doi: https://doi.org/10.1111/j.1551-2916.2010.03876.x. URL https://ceramics.onlinelibrary.wiley.com/doi/abs/10.1111/j.1551-2916.2010.03876.x.

[132] Gabriela Mera, Alexandra Navrotsky, Sabyasachi Sen, Hans-Joachim Kleebe, and Ralf Riedel. Polymer-derived SiCN and SiOC ceramics – structure and energetics at the

nanoscale. *Journal of Materials Chemistry A*, 1(12), 2013. ISSN 2050-7488 2050-7496. doi: 10.1039/c2ta00727d.

[133] FW Ainger and JM Herbert. The preparation of phosphorus-nitrogen compounds as non-porous solids. *Special Ceramics*, pages 168–182, 1960.

[134] W Verbeek. German patent 2.218, 960, 1973. In *Chem. Abstr*, volume 80, page 98019, 1974.

[135] W Verbeek and G Winter. German patent 2,236,078, 1974. In *Chem. Abstr*, volume 81, page 50911, 1974.

[136] Seishi Yajima, Josaburo Hayashi, and Mamoru Omori. Continuous silicon carbide fiber of high tensile strength. *Chemistry Letters*, 4(9):931–934, 1975.

[137] S Yajima, Y Hasegawa, K Okamura, and T Matsuzawa. Development of high tensile strength silicon carbide fibre using an organosilicon polymer precursor. *Nature*, 273 (5663):525, 1978.

[138] Erika Zanchetta, Marco Cattaldo, Giorgia Franchin, Martin Schwentenwein, Johannes Homa, Giovanna Brusatin, and Paolo Colombo. Stereolithography of SiOC ceramic microcomponents. *Advanced Materials*, 28(2):370–376, 2016.

[139] Emanuel Ionescu, Hans-Joachim Kleebe, and Ralf Riedel. Silicon-containing polymer-derived ceramic nanocomposites (PDC-NCs): Preparative approaches and properties. *Chemical Society Reviews*, 41(15):5032–5052, 2012.

[140] Gilvan Barroso, Quan Li, Rajendra K. Bordia, and Günter Motz. Polymeric and ceramic silicon-based coatings – a review. *Journal of Materials Chemistry A*, 7: 1936–1963, 2019. doi: 10.1039/C8TA09054H. URL http://dx.doi.org/10.1039/C8TA09054H.

[141] Dongjoon Ahn and Rishi Raj. Thermodynamic measurements pertaining to the hysteretic intercalation of lithium in polymer-derived silicon oxycarbide. *Journal of Power Sources*, 195(12):3900–3906, 2010. ISSN 0378-7753.

[142] Chaoyi Yan, Chuanhui Gong, Peihua Wangyang, Junwei Chu, Kai Hu, Chaobo Li, Xuepeng Wang, Xinchuan Du, Tianyou Zhai, Yanrong Li, and Jie Xiong. 2 D group IVB transition metal dichalcogenides. *Advanced Functional Materials*, 28(39):1803305, 2018. doi: https://doi.org/10.1002/adfm.201803305. URL https://onlinelibrary.wiley.com/doi/abs/10.1002/adfm.201803305.

[143] Shujie Tang, Chaofan Zhang, Dillon Wong, Zahra Pedramrazi, Hsin-Zon Tsai, Chunjing Jia, Brian Moritz, Martin Claassen, Hyejin Ryu, Salman Kahn, Juan Jiang, Hao Yan, Makoto Hashimoto, Donghui Lu, Robert G. Moore, Chan-Cuk Hwang, Choongyu Hwang, Zahid Hussain, Yulin Chen, Miguel M. Ugeda, Zhi Liu, Xiaoming Xie, Thomas P. Devereaux, Michael F. Crommie, Sung-Kwan Mo, and Zhi-Xun Shen. Quantum spin hall state in monolayer 1T′-WTe_2. *Nature Physics*, 13(7):683–687, 2017. ISSN 1745-2481. doi: 10.1038/nphys4174. URL https://doi.org/10.1038/nphys4174.

[144] Yifu Yu, Gwang-Hyeon Nam, Qiyuan He, Xue-Jun Wu, Kang Zhang, Zhenzhong Yang, Junze Chen, Qinglang Ma, Meiting Zhao, Zhengqing Liu, Fei-Rong Ran, Xingzhi Wang, Hai Li, Xiao Huang, Bing Li, Qihua Xiong, Qing Zhang, Zheng Liu, Lin Gu, Yonghua Du, Wei Huang, and Hua Zhang. High phase-purity 1T′-MoS_2- and 1T′-$MoSe_2$-layered crystals. *Nature Chemistry*, 10(6):638–643. ISSN 1755-4349. doi: 10.1038/s41557-018-0035-6. URL https://doi.org/10.1038/s41557-018-0035-6.

[145] Jung Sang Cho, Hyeon Seok Ju, Jung-Kul Lee, and Yun Chan Kang. Carbon/two-dimensional $MoTe_2$ core/shell-structured microspheres as an anode material for na-ion batteries. *Nanoscale*, 9(5):1942–1950, 2017.

[146] Eunjeong Yang, Hyunjun Ji, and Yousung Jung. Two-dimensional transition metal

dichalcogenide monolayers as promising sodium ion battery anodes. *The Journal of Physical Chemistry C*, 119(47):26374–26380, 2015. ISSN 1932-7447.

[147] Santanu Mukherjee, Jonathan Turnley, Elisabeth Mansfield, Jason Holm, Davi Soares, Lamuel David, and Gurpreet Singh. Exfoliated transition metal dichalcogenide nanosheets for supercapacitor and sodium ion battery applications. *Royal Society Open Science*, 6(8), 2019. ISSN 2054-5703 2054-5703. doi: 10.1098/rsos.190437.

[148] R Bhandavat, L David, and G Singh. Synthesis of surface-functionalized WS_2 nanosheets and performance as li-ion battery anodes. *The journal of physical chemistry letters*, 3(11):1523–1530, 2012. ISSN 1948-7185.

[149] Xiuqiang Xie, Taron Makaryan, Mengqiang Zhao, Katherine L. Van Aken, Yury Gogotsi, and Guoxiu Wang. MoS_2 nanosheets vertically aligned on carbon paper: A freestanding electrode for highly reversible sodium-ion batteries. *Advanced Energy Materials*, 6(5), 2016. ISSN 16146832. doi: 10.1002/aenm.201502161.

[150] Xiaomin Li, Zhenxing Feng, Jiantao Zai, Zi-Feng Ma, and Xuefeng Qian. Incorporation of Co into MoS_2/graphene nanocomposites: One effective way to enhance the cycling stability of li/na storage. *Journal of Power Sources*, 373:103–109, 2018. ISSN 0378-7753. doi: https://doi.org/10.1016/j.jpowsour.2017.10.094. URL http://www.sciencedirect.com/science/article/pii/S0378775317314568.

[151] Kowsalya Devi Rasamani, Farbod Alimohammadi, and Yugang Sun. Interlayer-expanded MoS_2. *Materials Today*, 20(2):83–91, 2017. ISSN 13697021. doi: 10.1016/j.mattod.2016.10.004.

[152] Santanu Mukherjee, Zhongkan Ren, and Gurpreet Singh. Molecular polymer-derived ceramics for applications in electrochemical energy storage devices. *Journal of Physics D: Applied Physics*, 51(46), 2018. ISSN 0022-3727 1361-6463. doi: 10.1088/1361-6463/aadb18.

[153] Xiuqiang Xie, Zhimin Ao, Dawei Su, Jinqiang Zhang, and Guoxiu Wang. MoS_2/graphene composite anodes with enhanced performance for sodium-ion batteries: The role of the two-dimensional heterointerface. *Advanced Functional Materials*, 25(9):1393–1403, 2015. ISSN 1616-301X.

[154] Weizhai Bao, Christopher E. Shuck, Wenxue Zhang, Xin Guo, Yury Gogotsi, and Guoxiu Wang. Boosting performance of Na–S batteries using sulfur-doped $Ti_3C_2T_x$ MXene nanosheets with a strong affinity to sodium polysulfides. *ACS Nano*, 13(10): 11500–11509, 2019. ISSN 1936-0851. doi: 10.1021/acsnano.9b04977. URL https://doi.org/10.1021/acsnano.9b04977.

[155] Tamas Varga, Alexandra Navrotsky, Julianna L. Moats, R. Michelle Morcos, Fabrizia Poli, Klaus Müller, Atanu Saha, and Rishi Raj. Thermodynamically stable $Si_xO_yC_z$ polymer-like amorphous ceramics. *Journal of the American Ceramic Society*, 90(10):3213–3219, 2007. ISSN 0002-7820. doi: 10.1111/j.1551-2916.2007.01874.x. URL https://doi.org/10.1111/j.1551-2916.2007.01874.x.

[156] Lamuel David, Romil Bhandavat, Uriel Barrera, and G. Singh. Silicon oxycarbide glass-graphene composite paper electrode for long-cycle lithium-ion batteries. *Nature Communications*, 7:10998, 2016. ISSN 2041-1723 (Electronic) 2041-1723 (Linking). doi: 10.1038/ncomms10998. URL https://www.ncbi.nlm.nih.gov/pubmed/27025781.

[157] Lamuel David, Romil Bhandavat, Uriel Barrera, and Gurpreet Singh. Polymer-derived ceramic functionalized MoS_2 composite paper as a stable lithium-ion battery electrode. *Scientific reports*, 5:9792, 2015. ISSN 2045-2322.

[158] VS Pradeep, DG Ayana, M Graczyk-Zajac, GD Soraru, and R Riedel. High rate capability of SiOC ceramic aerogels with tailored porosity as anode materials for Li-ion batteries. *Electrochimica Acta*, 157:41–45, 2015. ISSN 0013-4686.

[159] T. Le Mogne, C. Donnet, J. M. Martin, A. Tonck, N. Millard-Pinard, S. Fayeulle, and N. Moncoffre. Nature of super-lubricating MoS_2 physical vapor deposition coatings.

Journal of Vacuum Science & Technology A: Vacuum, Surfaces, and Films, 12(4): 1998–2004, 1994. ISSN 0734-2101 1520-8559. doi: 10.1116/1.578996.

[160] William A Brainard and Donald R Wheeler. An XPS study of the adherence of refractory carbide silicide and boride rf-sputtered wear-resistant coatings. *Journal of Vacuum Science and Technology*, 15(6):1800–1805, 1978. ISSN 0022-5355.

[161] I. Alstrup. A combined x-ray photoelectron and mössbauer emission spectroscopy study of the state of cobalt in sulfided, supported, and unsupported Co-Mo catalysts. *Journal of Catalysis*, 77(2):397–409, 1982. ISSN 00219517. doi: 10.1016/0021-9517(82)90181-6.

[162] B. Brox and I. Olefjord. Esca studies of MoO_2 and MoO_3. *Surface and Interface Analysis*, 13(1):3–6, 1988. ISSN 0142-2421 1096-9918. doi: 10.1002/sia.740130103.

[163] Santanu Bag, Amy F Gaudette, Mark E Bussell, and Mercouri G Kanatzidis. Spongy chalcogels of non-platinum metals act as effective hydrodesulfurization catalysts. *Nature chemistry*, 1(3):217, 2009. ISSN 1755-4349.

[164] Jianxin Mao, Peng Liu, Cuicui Du, Dongxue Liang, Jianyue Yan, and Wenbo Song. Tailoring 2 D MoS_2 heterointerfaces for promising oxygen reduction reaction electrocatalysis. *Journal of Materials Chemistry A*, 7(15):8785–8789, 2019. ISSN 2050-7488 2050-7496. doi: 10.1039/c9ta01321k.

[165] D. S. Zingg, Leo E. Makovsky, R. E. Tischer, Fred R. Brown, and David M. Hercules. A surface spectroscopic study of molybdenum-alumina catalysts using x-ray photoelectron, ion-scattering, and raman spectroscopies. *The Journal of Physical Chemistry*, 84 (22):2898–2906, 1980. ISSN 0022-3654 1541-5740. doi: 10.1021/j100459a015.

[166] GC Stevens and T Edmonds. Catalytic activity of the basal and edge planes of molybdenum disulphide. *Journal of the Less Common Metals*, 54(2):321–330, 1977. ISSN 0022-5088.

[167] C. Ma, H. Zhu, J. Zhou, Z. Cui, T. Liu, Y. Wang, Y. Wang, and Z. Zou. Confinement effect of monolayer mos2 quantum dots on conjugated polyimide and promotion

of solar-driven photocatalytic hydrogen generation. *Dalton Trans*, 46(12):3877–3886, 2017. ISSN 1477-9234 (Electronic) 1477-9226 (Linking). doi: 10.1039/c6dt04916h. URL https://www.ncbi.nlm.nih.gov/pubmed/28262867.

[168] Xiang Li, Junhao Li, Qingsheng Gao, Xiang Yu, Renzong Hu, Jun Liu, Lichun Yang, and Min Zhu. MoS_2 nanosheets with conformal carbon coating as stable anode materials for sodium-ion batteries. *Electrochimica Acta*, 254:172–180, 2017. ISSN 00134686. doi: 10.1016/j.electacta.2017.09.128.

[169] Catarina Pereira-Nabais, Jolanta Swiatowska, Alexandre Chagnes, Francois Ozanam, Aurelien Gohier, Pierre Tran-Van, Costel-Sorin Cojocaru, Michel Cassir, and Philippe Marcus. Interphase chemistry of Si electrodes used as anodes in Li-ion batteries. *Applied Surface Science*, 266:5–16, 2013. ISSN 0169-4332.

[170] Lorenzo Di Mario, Stefano Turchini, Nicola Zema, Roberto Cimino, and Faustino Martelli. Electronic properties of Si hollow nanowires. *Journal of Applied Physics*, 116 (17):174310, 2014. ISSN 0021-8979.

[171] Yafang Han. *Physics and Techniques of Ceramic and Polymeric Materials: Proceedings of Chinese Materials Conference 2018*, volume 216. Springer, 2019. ISBN 9811359474.

[172] R Alfonsetti, Luca Lozzi, Maurizio Passacantando, P Picozzi, and Sandro Santucci. XPS studies on SiO_x thin films. *Applied Surface Science*, 70:222–225, 1993. ISSN 0169-4332.

[173] RP Socha and J Väyrynen. The influence of fluoride anions on the silicon carbide surface oxidation in aqueous solutions. *Applied surface science*, 212:636–643, 2003. ISSN 0169-4332.

[174] Seong-Cheol Noh, Seoung Young Lee, Yong Gun Shul, and Kwang-Deog Jung. Sulfuric acid decomposition on the Pt/n-SiC catalyst for SI cycle to produce hydrogen. *International Journal of Hydrogen Energy*, 39(9):4181–4188, 2014. ISSN 0360-3199.

[175] Dingjun Wang, Jack H Lunsford, and Michael P Rosynek. Characterization of a Mo/ZSM-5 catalyst for the conversion of methane to benzene. *Journal of Catalysis*, 169(1):347–358, 1997. ISSN 0021-9517.

[176] L Muehlhoff, WJ Choyke, MJ Bozack, and John T Yates Jr. Comparative electron spectroscopic studies of surface segregation on SiC (0001) and SiC (0001). *Journal of Applied Physics*, 60(8):2842–2853, 1986. ISSN 0021-8979.

[177] Arindam Saha, SK Basiruddin, Sekhar Chandra Ray, SS Roy, and Nikhil R Jana. Functionalized graphene and graphene oxide solution via polyacrylate coating. *Nanoscale*, 2(12):2777–2782, 2010.

[178] Joanna Duch, Michał Mazur, M Golda-Cepa, Jerzy Podobiński, Witold Piskorz, and Andrzej Kotarba. Insight into the modification of electrodonor properties of multi-walled carbon nanotubes via oxygen plasma: Surface functionalization versus amorphization. *Carbon*, 137:425–432, 2018. ISSN 0008-6223.

[179] Muhammad Idrees, Saima Batool, Jie Kong, Qiang Zhuang, Hu Liu, Qian Shao, Na Lu, Yining Feng, Evan K Wujcik, and Qiang Gao. Polyborosilazane derived ceramics-nitrogen sulfur dual doped graphene nanocomposite anode for enhanced lithium ion batteries. *Electrochimica Acta*, 296:925–937, 2019. ISSN 0013-4686.

[180] J Ashley Taylor, Gerald M Lancaster, A Ignatiev, and J Wayne Rabalais. Interactions of ion beams with surfaces. reactions of nitrogen with silicon and its oxides. *The Journal of Chemical Physics*, 68(4):1776–1784, 1978. ISSN 0021-9606.

[181] C. Lee, H. Yan, L. E. Brus, T. F. Heinz, J. Hone, and S. Ryu. Anomalous lattice vibrations of single- and few-layer MoS_2. *ACS Nano*, 4(5):2695–700, 2010. ISSN 1936-086X (Electronic) 1936-0851 (Linking). doi: 10.1021/nn1003937. URL https://www.ncbi.nlm.nih.gov/pubmed/20392077.

[182] M. Naz, T. Hallam, N. C. Berner, N. McEvoy, R. Gatensby, J. B. McManus, Z. Akhter, and G. S. Duesberg. A new 2h-2H′/1t cophase in polycrystalline MoS_2 and $MoSe_2$

thin films. *ACS Applied Materials & Interfaces*, 8(45):31442–31448, 2016. ISSN 1944-8252 (Electronic) 1944-8244 (Linking). doi: 10.1021/acsami.6b10972. URL https://www.ncbi.nlm.nih.gov/pubmed/27775313.

[183] Matteo Calandra. Chemically exfoliated single-layer MoS_2: Stability, lattice dynamics, and catalytic adsorption from first principles. *Physical Review B*, 88(24), 2013. ISSN 1098-0121 1550-235X. doi: 10.1103/PhysRevB.88.245428.

[184] Hong Li, Qing Zhang, Chin Chong Ray Yap, Beng Kang Tay, Teo Hang Tong Edwin, Aurelien Olivier, and Dominique Baillargeat. From bulk to monolayer MoS_2: Evolution of raman scattering. *Advanced Functional Materials*, 22(7):1385–1390, 2012. ISSN 1616301X. doi: 10.1002/adfm.201102111.

[185] Edmond Payen, Slavik Kasztelan, Sabine Houssenbay, Raymond Szymanski, and Jean Grimblot. Genesis and characterization by laser raman spectroscopy and high-resolution electron microscopy of supported molybdenum disulfide crystallites. *The Journal of Physical Chemistry*, 93(17):6501–6506, 1989. ISSN 0022-3654. doi: 10.1021/j100354a043. URL https://doi.org/10.1021/j100354a043.

[186] Christina Stabler, Andreas Reitz, Peter Stein, Barbara Albert, Ralf Riedel, and Emanuel Ionescu. Thermal properties of SiOC glasses and glass ceramics at elevated temperatures. *Materials*, 11(2):279, 2018. ISSN 1996-1944. URL https://www.mdpi.com/1996-1944/11/2/279.

[187] M. A. Pimenta, G. Dresselhaus, M. S. Dresselhaus, L. G. Cançado, A. Jorio, and R. Saito. Studying disorder in graphite-based systems by raman spectroscopy. *Physical Chemistry Chemical Physics*, 9(11):1276–1290, 2007. ISSN 1463-9076. doi: 10.1039/B613962K. URL http://dx.doi.org/10.1039/B613962K.

[188] J Wolfenstine, U Lee, and JL Allen. Electrical conductivity and rate-capability of $Li_4Ti_5O_{12}$ as a function of heat-treatment atmosphere. *Journal of Power Sources*, 154: 287–289, 2006. ISSN 0378-7753.

[189] Shahua Huang, Zhaoyin Wen, Xiujian Zhu, and Xuelin Yang. Research on $Li_4Ti_5O_{12}/Cu_xO$ composite anode materials for lithium-ion batteries. *Journal of the Electrochemical Society*, 152(7):A1301–A1305, 2005. ISSN 0013-4651.

[190] Maria R Lukatskaya, Bruce Dunn, and Yury Gogotsi. Multidimensional materials and device architectures for future hybrid energy storage. *Nature communications*, 7:12647, 2016. ISSN 2041-1723.

[191] Elodie Blanco, Pavel Afanasiev, Gilles Berhault, Denis Uzio, and Stephane Loridant. Resonance raman spectroscopy as a probe of the crystallite size of MoS_2 nanoparticles. *Comptes Rendus Chimie*, 19(10):1310–1314, 2016. ISSN 1631-0748. doi: https://doi.org/10.1016/j.crci.2015.08.014. URL http://www.sciencedirect.com/science/article/pii/S1631074816000254.

[192] Juliana Sánchez, Andrés Moreno, Fanor Mondragón, and Kevin J. Smith. Morphological and structural properties of MoS_2 and MoS_2-amorphous silica-alumina dispersed catalysts for slurry-phase hydroconversion. *Energy & Fuels*, 32(6):7066–7077, 2018. ISSN 0887-0624. doi: 10.1021/acs.energyfuels.8b01081. URL https://doi.org/10.1021/acs.energyfuels.8b01081.

[193] Alexander V Kolobov and Junji Tominaga. *Two-Dimensional Transition-Metal Dichalcogenides*, volume 239. Springer, 2016. ISBN 3319314505.

[194] Roscoe G Dickinson and Linus Pauling. The crystal structure of molybdenite. *Journal of the American Chemical Society*, 45(6):1466–1471, 1923. ISSN 0002-7863.

[195] V Petkov, SJL Billinge, P Larson, SD Mahanti, T Vogt, KK Rangan, and Mercouri G Kanatzidis. Structure of nanocrystalline materials using atomic pair distribution function analysis: Study of $LiMoS_2$. *Physical Review B*, 65(9):092105, 2002.

[196] L. Ries, E. Petit, T. Michel, C. C. Diogo, C. Gervais, C. Salameh, M. Bechelany, S. Balme, P. Miele, N. Onofrio, and D. Voiry. Enhanced sieving from exfoliated MoS_2 membranes via covalent functionalization. *Nature Materials*, 18(10):1112–1117, 2019.

ISSN 1476-1122 (Print) 1476-1122 (Linking). doi: 10.1038/s41563-019-0464-7. URL https://www.ncbi.nlm.nih.gov/pubmed/31451779.

[197] K.S. Liang, R.R. Chianelli, F.Z. Chien, and S.C. Moss. Structure of poorly crystalline MoS_2 — a modeling study. *Journal of Non-Crystalline Solids*, 79(3):251–273, 1986. ISSN 0022-3093. doi: https://doi.org/10.1016/0022-3093(86)90226-7. URL https://www.sciencedirect.com/science/article/pii/0022309386902267.

[198] W. H. Ryu, J. W. Jung, K. Park, S. J. Kim, and I. D. Kim. Vine-like MoS_2 anode materials self-assembled from 1-d nanofibers for high capacity sodium rechargeable batteries. *Nanoscale*, 6(19):10975–81, 2014. ISSN 2040-3372 (Electronic) 2040-3364 (Linking). doi: 10.1039/c4nr02044h. URL https://www.ncbi.nlm.nih.gov/pubmed/24958669.

[199] S. Zhang, X. Yu, H. Yu, Y. Chen, P. Gao, C. Li, and C. Zhu. Growth of ultra-thin MoS_2 nanosheets with expanded spacing of (002) plane on carbon nanotubes for high-performance sodium-ion battery anodes. *ACS Applied Materials & Interfaces*, 6(24):21880–5, 2014. ISSN 1944-8252 (Electronic) 1944-8244 (Linking). doi: 10.1021/am5061036. URL https://www.ncbi.nlm.nih.gov/pubmed/25479568.

[200] Ge Li, Dan Luo, Xiaolei Wang, Min Ho Seo, Sahar Hemmati, Aiping Yu, and Zhongwei Chen. Enhanced reversible sodium-ion intercalation by synergistic coupling of few-layered MoS_2 and S-doped graphene. *Advanced Functional Materials*, 27(40), 2017. ISSN 1616301X. doi: 10.1002/adfm.201702562.

[201] Guobao Xu, Liwen Yang, Xiaolin Wei, Jianwen Ding, Jianxin Zhong, and Paul K. Chu. MoS_2-quantum-dot-interspersed $Li_4Ti_5O_{12}$ nanosheets with enhanced performance for Li- and Na-ion batteries. *Advanced Functional Materials*, 26(19):3349–3358, 2016. ISSN 1616301X. doi: 10.1002/adfm.201505435.

[202] Z. Chen, D. Yin, and M. Zhang. Sandwich-like MoS_2@SnO_2@C with high capacity and stability for sodium/potassium ion batteries. *Small*, 14(17):e1703818, 2018. ISSN 1613-

6829 (Electronic) 1613-6810 (Linking). doi: 10.1002/smll.201703818. URL https://www.ncbi.nlm.nih.gov/pubmed/29542256.

[203] M Bik, M Stygar, P Jelen, J Dabrowa, M Lesniak, T Brylewski, and M Sitarz. Protective-conducting coatings based on black glasses (SiOC) for application in solid oxide fuel cells. *International Journal of Hydrogen Energy*, 42(44):27298–27307, 2017. ISSN 0360-3199.

[204] Z. Hu, L. Wang, K. Zhang, J. Wang, F. Cheng, Z. Tao, and J. Chen. MoS_2 nanoflowers with expanded interlayers as high-performance anodes for sodium-ion batteries. *Angewandte Chemie International Edition in English*, 53(47):12794–8, 2014. ISSN 1521-3773 (Electronic) 1433-7851 (Linking). doi: 10.1002/anie.201407898. URL https://www.ncbi.nlm.nih.gov/pubmed/25251780.

[205] Yongho Lee, Kwan Young Lee, and Wonchang Choi. One-pot synthesis of antimony-embedded silicon oxycarbide materials for high-performance sodium-ion batteries. *Advanced Functional Materials*, 27(43), 2017. ISSN 1616301X. doi: 10.1002/adfm.201702607.

[206] Jan Kaspar, Caglar Terzioglu, Emanuel Ionescu, Magdalena Graczyk-Zajac, Stefania Hapis, Hans-Joachim Kleebe, and Ralf Riedel. Stable SiOC/Sn nanocomposite anodes for lithium-ion batteries with outstanding cycling stability. *Advanced Functional Materials*, 24(26):4097–4104, 2014. ISSN 1616301X. doi: 10.1002/adfm.201303828.

[207] Jinsoo Park, Jong-Seon Kim, Jin-Woo Park, Tae-Hyun Nam, Ki-Won Kim, Jou-Hyeon Ahn, Guoxiu Wang, and Hyo-Jun Ahn. Discharge mechanism of MoS_2 for sodium ion battery: Electrochemical measurements and characterization. *Electrochimica Acta*, 92:427–432, 2013. ISSN 0013-4686. doi: https://doi.org/10.1016/j.electacta.2013.01.057. URL https://www.sciencedirect.com/science/article/pii/S0013468613000893.

[208] Dawei Su, Shixue Dou, and Guoxiu Wang. Ultrathin MoS_2 nanosheets as anode ma-

terials for sodium-ion batteries with superior performance. *Advanced Energy Materials*, 5(6):1401205, 2015. doi: https://doi.org/10.1002/aenm.201401205. URL https://onlinelibrary.wiley.com/doi/abs/10.1002/aenm.201401205.

[209] John Wang, Julien Polleux, James Lim, and Bruce Dunn. Pseudocapacitive contributions to electrochemical energy storage in TiO_2 (anatase) nanoparticles. *The Journal of Physical Chemistry C*, 111(40):14925–14931, 2007. ISSN 1932-7447. doi: 10.1021/jp074464w. URL https://doi.org/10.1021/jp074464w.

[210] Yutao Dong, Dan Li, Chengwei Gao, Yushan Liu, and Jianmin Zhang. A self-assembled 3 D urchin-like $Ti_{0.08}Sn_{0.2}O_2$-rGO hybrid nanostructure as an anode material for high-rate and long cycle life li-ion batteries. *Journal of Materials Chemistry A*, 5(17): 8087–8094, 2017.

[211] Lei Huang, Qiulong Wei, Xiaoming Xu, Changwei Shi, Xue Liu, Liang Zhou, and Liqiang Mai. Methyl-functionalized MoS_2 nanosheets with reduced lattice breathing for enhanced pseudocapacitive sodium storage. *Physical Chemistry Chemical Physics*, 19(21):13696–13702, 2017.

[212] Max Lu. *Supercapacitors: materials, systems, and applications*. John Wiley & Sons, 2013. ISBN 352764668X.

[213] Ping-Chun Tsai, Bohua Wen, Mark Wolfman, Min-Ju Choe, Menghsuan Sam Pan, Liang Su, Katsuyo Thornton, Jordi Cabana, and Yet-Ming Chiang. Single-particle measurements of electrochemical kinetics in nmc and nca cathodes for li-ion batteries. *Energy & Environmental Science*, 11(4):860–871, 2018. ISSN 1754-5692. doi: 10.1039/C8EE00001H. URL http://dx.doi.org/10.1039/C8EE00001H.

[214] Tushar Swamy and Yet-Ming Chiang. Electrochemical charge transfer reaction kinetics at the silicon-liquid electrolyte interface. *Journal of The Electrochemical Society*, 162 (13):A7129–A7134, 2015. ISSN 0013-4651.

[215] Mingkai Liu, Peng Zhang, Zehua Qu, Yan Yan, Chao Lai, Tianxi Liu, and Shanqing Zhang. Conductive carbon nanofiber interpenetrated graphene architecture for ultrastable sodium ion battery. *Nature communications*, 10(1):1–11, 2019. ISSN 2041-1723.

[216] Chenrayan Senthil, Subramani Amutha, Ramasamy Gnanamuthu, Kumaran Vediappan, and Chang Woo Lee. Metallic 1T-MoS_2 overlapped nitrogen-doped carbon superstructures for enhanced sodium-ion storage. *Applied Surface Science*, 2019. ISSN 0169-4332.

[217] Yang Wang, Yinlong Zhu, Sepideh Afshar, Meng Wai Woo, Jing Tang, Timothy Williams, Biao Kong, Dongyuan Zhao, Huanting Wang, and Cordelia Selomulya. One-dimensional CoS_2-MoS_2 nano-flakes decorated MoO_2 sub-micro-wires for synergistically enhanced hydrogen evolution. *Nanoscale*, 11(8):3500–3505, 2019.

[218] Wenchao Zhang, Yajie Liu, and Zaiping Guo. Approaching high-performance potassium-ion batteries via advanced design strategies and engineering. *Science Advances*, 5(5):eaav7412, 2019. doi: 10.1126/sciadv.aav7412. URL http://advances.sciencemag.org/content/5/5/eaav7412.abstract.

[219] Xi Wang, Qunhong Weng, Yijun Yang, Yoshio Bando, and Dmitri Golberg. Hybrid two-dimensional materials in rechargeable battery applications and their microscopic mechanisms. *Chemical Society Reviews*, 45(15):4042–4073, 2016. ISSN 0306-0012. doi: 10.1039/C5CS00937E. URL http://dx.doi.org/10.1039/C5CS00937E.

[220] Yingxi Zhang, Liao Zhang, Tuan Lv, Paul K. Chu, and Kaifu Huo. Two-dimensional transition metal chalcogenides for alkali metal ions storage. *ChemSusChem*, 13(6): 1114 – 1154, 2020. ISSN 1864 – 5631. doi: 10.1002/cssc.201903245. URL https://doi.org/10.1002/cssc.201903245.

[221] Jie Sun, Hyun-Wook Lee, Mauro Pasta, Hongtao Yuan, Guangyuan Zheng, Yongming Sun, Yuzhang Li, and Yi Cui. A phosphorene–graphene hybrid material as a high-capacity anode for sodium-ion batteries. *Nature Nanotechnology*, 10(11):980–985, 2015.

ISSN 1748-3395. doi: 10.1038/nnano.2015.194. URL https://doi.org/10.1038/nnano.2015.194.

[222] Xiaodi Ren, Qiang Zhao, William D. McCulloch, and Yiying Wu. MoS_2 as a long-life host material for potassium ion intercalation. *Nano Research*, 10(4):1313–1321, 2017. ISSN 1998-0000. doi: 10.1007/s12274-016-1419-9. URL https://doi.org/10.1007/s12274-016-1419-9.

[223] Keyu Xie, Kai Yuan, Xin Li, Wei Lu, Chao Shen, Chenglu Liang, Robert Vajtai, Pulickel Ajayan, and Bingqing Wei. Superior potassium ion storage via vertical MoS_2 "nano-rose" with expanded interlayers on graphene. *Small*, 13(42):1701471, 2017. ISSN 1613-6810. doi: 10.1002/smll.201701471. URL https://onlinelibrary.wiley.com/doi/abs/10.1002/smll.201701471.

[224] Liping Wang, Jian Zou, Shulin Chen, Ge Zhou, Jianming Bai, Peng Gao, Yuesheng Wang, Xiqian Yu, Jingze Li, Yong-Sheng Hu, and Hong Li. TiS_2 as a high performance potassium ion battery cathode in ether-based electrolyte. *Energy Storage Materials*, 12:216–222, 2018. ISSN 2405-8297. doi: https://doi.org/10.1016/j.ensm.2017.12.018. URL http://www.sciencedirect.com/science/article/pii/S240582971730630X.

[225] Yuhan Wu, Yang Xu, Yueliang Li, Pengbo Lyu, Jin Wen, Chenglin Zhang, Min Zhou, Yaoguo Fang, Huaping Zhao, Ute Kaiser, and Yong Lei. Unexpected intercalation-dominated potassium storage in WS_2 as a potassium-ion battery anode. *Nano Research*, 12(12):2997–3002, 2019. ISSN 1998-0000. doi: 10.1007/s12274-019-2543-0. URL https://doi.org/10.1007/s12274-019-2543-0.

[226] Biyu Kang, Xiaochuan Chen, Lingxing Zeng, Fenqiang Luo, Xinye Li, Lihong Xu, Min-Quan Yang, Qinghua Chen, Mingdeng Wei, and Qingrong Qian. In situ fabrication of ultrathin few-layered WSe_2 anchored on N, P dual-doped carbon by bioreactor for half/full sodium/potassium-ion batteries with ultralong cycling lifespan. *Journal of Colloid and Interface Science*, 574:217–228, 2020. ISSN 0021-9797. doi: https://

doi.org/10.1016/j.jcis.2020.04.055. URL http://www.sciencedirect.com/science/article/pii/S0021979720305038.

[227] Bruce E Brown. The crystal structures of WTe_2 and high-temperature $MoTe_2$. *Acta Crystallographica*, 20(2):268–274, 1966. ISSN 0365-110X.

[228] Arthur Mar, Stephane Jobic, and James A. Ibers. Metal-metal vs tellurium-tellurium bonding in WTe_2 and its ternary variants $TaIrTe_4$ and $NbIrTe_4$. *Journal of the American Chemical Society*, 114(23):8963–8971, 1992. ISSN 0002-7863. doi: 10.1021/ja00049a029. URL https://doi.org/10.1021/ja00049a029.

[229] Chi Chen, Xiuqiang Xie, Babak Anasori, Asya Sarycheva, Taron Makaryan, Mengqiang Zhao, Patrick Urbankowski, Ling Miao, Jianjun Jiang, and Yury Gogotsi. MoS_2-on-MXene heterostructures as highly reversible anode materials for lithium-ion batteries. *Angewandte Chemie International Edition*, 57(7):1846–1850, 2018. ISSN 1433-7851. doi: 10.1002/anie.201710616. URL https://doi.org/10.1002/anie.201710616.

[230] Challapalli Suryanarayana and M Grant Norton. *X-ray diffraction: a practical approach*. Springer Science & Business Media, 2013. ISBN 1489901485.

[231] Li Zhu, Qi-Yuan Li, Yang-Yang Lv, Shichao Li, Xin-Yang Zhu, Zhen-Yu Jia, Y. B. Chen, Jinsheng Wen, and Shao-Chun Li. Superconductivity in potassium-intercalated Td-WTe_2. *Nano Letters*, 18(10):6585–6590, 2018. ISSN 1530-6984. doi: 10.1021/acs.nanolett.8b03180. URL https://doi.org/10.1021/acs.nanolett.8b03180.

[232] W G Dawson and D W Bullett. Electronic structure and crystallography of $MoTe_2$ and WTe_2. *Journal of Physics C: Solid State Physics*, 20(36):6159–6174, dec 1987. doi: 10.1088/0022-3719/20/36/017. URL https://doi.org/10.1088/0022-3719/20/36/017.

[233] Liang-Ying Feng, Rovi Angelo B. Villaos, Zhi-Quan Huang, Chia-Hsiu Hsu, and Feng-Chuan Chuang. Layer-dependent band engineering of Pd dichalcogenides: a first-

principles study. *New Journal of Physics*, 22(5):053010, may 2020. doi: 10.1088/1367-2630/ab7d7a. URL https://doi.org/10.1088/1367-2630/ab7d7a.

[234] J. Augustin, V. Eyert, Th. Böker, W. Frentrup, H. Dwelk, C. Janowitz, and R. Manzke. Electronic band structure of the layered compound Td−WTe_2. *Phys. Rev. B*, 62: 10812–10823, Oct 2000. doi: 10.1103/PhysRevB.62.10812. URL https://link.aps.org/doi/10.1103/PhysRevB.62.10812.

[235] Enze Zhang, Rui Chen, Ce Huang, Jihai Yu, Kaitai Zhang, Weiyi Wang, Shanshan Liu, Jiwei Ling, Xiangang Wan, Hai-Zhou Lu, and Faxian Xiu. Tunable positive to negative magnetoresistance in atomically thin WTe_2. *Nano Letters*, 17(2):878–885, 2017. ISSN 1530-6984. doi: 10.1021/acs.nanolett.6b04194. URL https://doi.org/10.1021/acs.nanolett.6b04194.

[236] Jiadong Zhou, Fucai Liu, Junhao Lin, Xiangwei Huang, Juan Xia, Bowei Zhang, Qingsheng Zeng, Hong Wang, Chao Zhu, Lin Niu, Xuewen Wang, Wei Fu, Peng Yu, Tay-Rong Chang, Chuang-Han Hsu, Di Wu, Horng-Tay Jeng, Yizhong Huang, Hsin Lin, Zexiang Shen, Changli Yang, Li Lu, Kazu Suenaga, Wu Zhou, Sokrates T. Pantelides, Guangtong Liu, and Zheng Liu. Large-area and high-quality 2 D transition metal telluride. *Advanced Materials*, 29(3):1603471, 2017. ISSN 0935-9648. doi: 10.1002/adma.201603471. URL https://doi.org/10.1002/adma.201603471.

[237] Younghee Kim, Young In Jhon, June Park, Jae Hun Kim, Seok Lee, and Young Min Jhon. Anomalous raman scattering and lattice dynamics in mono- and few-layer WTe_2. *Nanoscale*, 8(4):2309–2316, 2016. ISSN 2040-3364. doi: 10.1039/C5NR06098B. URL http://dx.doi.org/10.1039/C5NR06098B.

[238] Michal J. Mleczko, Runjie Lily Xu, Kye Okabe, Hsueh-Hui Kuo, Ian R. Fisher, H. S. Philip Wong, Yoshio Nishi, and Eric Pop. High current density and low thermal conductivity of atomically thin semimetallic WTe_2. *ACS Nano*, 10(8):7507–7514, 2016. ISSN 1936-0851. doi: 10.1021/acsnano.6b02368. URL https://doi.org/10.1021/acsnano.6b02368.

[239] W.-D. Kong, S.-F. Wu, P. Richard, C.-S. Lian, J.-T. Wang, C.-L. Yang, Y.-G. Shi, and H. Ding. Raman scattering investigation of large positive magnetoresistance material WTe_2. *Applied Physics Letters*, 106(8):081906, 2015. doi: 10.1063/1.4913680. URL https://aip.scitation.org/doi/abs/10.1063/1.4913680.

[240] Kun Chen, Zefeng Chen, Xi Wan, Zebo Zheng, Fangyan Xie, Wenjun Chen, Xuchun Gui, Huanjun Chen, Weiguang Xie, and Jianbin Xu. A simple method for synthesis of high-quality millimeter-scale 1T′ transition-metal telluride and near-field nanooptical properties. *Advanced Materials*, 29(38):1700704, 2017. ISSN 0935-9648. doi: 10.1002/adma.201700704. URL https://doi.org/10.1002/adma.201700704.

[241] Abhay Shivayogimath, Joachim Dahl Thomsen, David M. A. Mackenzie, Mathias Geisler, Raluca-Maria Stan, Ann Julie Holt, Marco Bianchi, Andrea Crovetto, Patrick R. Whelan, Alexandra Carvalho, Antonio H. Castro Neto, Philip Hofmann, Nicolas Stenger, Peter Bøggild, and Timothy J. Booth. A universal approach for the synthesis of two-dimensional binary compounds. *Nature Communications*, 10 (1):2957, 2019. ISSN 2041-1723. doi: 10.1038/s41467-019-11075-2. URL https://doi.org/10.1038/s41467-019-11075-2.

[242] Yufan Zhou, Mao Su, Xiaofei Yu, Yanyan Zhang, Jun-Gang Wang, Xiaodi Ren, Ruiguo Cao, Wu Xu, Donald R. Baer, Yingge Du, Oleg Borodin, Yanting Wang, Xue-Lin Wang, Kang Xu, Zhijie Xu, Chongmin Wang, and Zihua Zhu. Real-time mass spectrometric characterization of the solid–electrolyte interphase of a lithium-ion battery. *Nature Nanotechnology*, 15(3):224–230, 2020. ISSN 1748-3395. doi: 10.1038/s41565-019-0618-4. URL https://doi.org/10.1038/s41565-019-0618-4.

[243] Magali Gauthier, Thomas J. Carney, Alexis Grimaud, Livia Giordano, Nir Pour, Hao-Hsun Chang, David P. Fenning, Simon F. Lux, Odysseas Paschos, Christoph Bauer, Filippo Maglia, Saskia Lupart, Peter Lamp, and Yang Shao-Horn. Electrode–electrolyte interface in li-ion batteries: Current understanding and new insights.

The Journal of Physical Chemistry Letters, 6(22):4653–4672, 2015. doi: 10.1021/acs.jpclett.5b01727. URL https://doi.org/10.1021/acs.jpclett.5b01727.

[244] Tao Deng, Xiulin Fan, Chao Luo, Ji Chen, Long Chen, Singyuk Hou, Nico Eidson, Xiuquan Zhou, and Chunsheng Wang. Self-templated formation of P_2-type $K_{0.6}CoO_2$ microspheres for high reversible potassium-ion batteries. *Nano Letters*, 18(2):1522–1529, 2018. ISSN 1530-6984. doi: 10.1021/acs.nanolett.7b05324. URL https://doi.org/10.1021/acs.nanolett.7b05324.

[245] Cai-ling Liu, Shao-hua Luo, Hong-bo Huang, Yu-chun Zhai, and Zhao-wen Wang. Layered potassium-deficient P2- and P3-type cathode materials K_xMnO_2 for k-ion batteries. *Chemical Engineering Journal*, 356:53–59, 2019. ISSN 1385-8947. doi: https://doi.org/10.1016/j.cej.2018.09.012. URL http://www.sciencedirect.com/science/article/pii/S1385894718317224.

[246] Shao-hua Luo, Dong-bei Hu, Huan Liu, Jun-zhe Li, and Ting-Feng Yi. Hydrothermal synthesis and characterization of α-Fe_2O_3/C using acid-pickled iron oxide red for Li-ion batteries. *Journal of Hazardous Materials*, 368:714–721, 2019. ISSN 0304-3894. doi: https://doi.org/10.1016/j.jhazmat.2019.01.106. URL http://www.sciencedirect.com/science/article/pii/S030438941930113X.

[247] R. Mark Wightman. Methods to improve electrochemical reversibility at carbon electrodes. *Journal of The Electrochemical Society*, 131(7):1578, 1984. ISSN 0013-4651. doi: 10.1149/1.2115913. URL http://dx.doi.org/10.1149/1.2115913.

[248] Stephen Fletcher, Victoria Jane Black, and Iain Kirkpatrick. A universal equivalent circuit for carbon-based supercapacitors. *Journal of Solid State Electrochemistry*, 18 (5):1377–1387, 2014. ISSN 1433-0768. doi: 10.1007/s10008-013-2328-4. URL https://doi.org/10.1007/s10008-013-2328-4.

[249] Evgenij Barsoukov and J Ross Macdonald. Impedance spectroscopy theory, experiment, and. *Applications, 2nd ed.(Hoboken, NJ: John Wiley &Sons, Inc., 2005)*, 2005.

[250] Zsolt Kerner and Tamás Pajkossy. On the origin of capacitance dispersion of rough electrodes. *Electrochimica Acta*, 46(2):207–211, 2000. ISSN 0013-4686. doi: https://doi.org/10.1016/S0013-4686(00)00574-0. URL http://www.sciencedirect.com/science/article/pii/S0013468600005740.

[251] Tamás Pajkossy. Impedance of rough capacitive electrodes. *Journal of Electroanalytical Chemistry*, 364(1):111–125, 1994. ISSN 1572-6657. doi: https://doi.org/10.1016/0022-0728(93)02949-I. URL http://www.sciencedirect.com/science/article/pii/002207289302949I.

[252] B. V. Tilak, C. P. Chen, and S. K. Rangarajan. A model to characterize the impedance of electrochemical capacitors arising from reactions of the type $O_{ad} + ne^- <= R_{ad}$. *Journal of Electroanalytical Chemistry*, 324(1):405–414, 1992. ISSN 1572-6657. doi: https://doi.org/10.1016/0022-0728(92)80060-H. URL http://www.sciencedirect.com/science/article/pii/002207289280060H.

[253] T. C. Liu. Behavior of molybdenum nitrides as materials for electrochemical capacitors. *Journal of The Electrochemical Society*, 145(6):1882, 1998. ISSN 0013-4651. doi: 10.1149/1.1838571. URL http://dx.doi.org/10.1149/1.1838571.

[254] G. P. Halada and C. R. Clayton. Comparison of Mo-N and W-N synergism during passivation of stainless steel through x-ray photoelectron spectroscopy and electrochemical analysis. *Journal of Vacuum Science & Technology A*, 11(4):2342–2347, 1993. ISSN 0734-2101. doi: 10.1116/1.578373. URL https://doi.org/10.1116/1.578373.

[255] G. Leftheriotis, S. Papaefthimiou, P. Yianoulis, and A. Siokou. Effect of the tungsten oxidation states in the thermal coloration and bleaching of amorphous WO_3 films. *Thin Solid Films*, 384(2):298–306, 2001. ISSN 0040-6090. doi: https://doi.org/10.1016/S0040-6090(00)01828-9. URL http://www.sciencedirect.com/science/article/pii/S0040609000018289.

[256] Sungjin Park, Jinho An, Richard D. Piner, Inhwa Jung, Dongxing Yang, Aruna Ve-

lamakanni, SonBinh T. Nguyen, and Rodney S. Ruoff. Aqueous suspension and characterization of chemically modified graphene sheets. *Chemistry of Materials*, 20(21):6592–6594, 2008. ISSN 0897-4756. doi: 10.1021/cm801932u. URL https://doi.org/10.1021/cm801932u.

[257] John F Moulder, William F Stickle, Peter E Sobol, and Kenneth D Bomben. *Handbook of X-ray photoelectron spectroscopy: a reference book of standard spectra for identification and interpretation of XPS data*. Perkin-Elmer Corporation, Eden Prairie, Minnesota, 1992.

[258] Diego Bisero, Alessandro di Bona, Paola Paradisi, and Sergio Valeri. K_2Te photocathode growth: A photoemission study. *Journal of Applied Physics*, 87(1):543–548, 1999. ISSN 0021-8979. doi: 10.1063/1.371897. URL https://doi.org/10.1063/1.371897.

[259] Linda D. Schultz. Synthesis and characterization of potassium polytellurides in liquid ammonia solution. *Inorganica Chimica Acta*, 176(2):271–275, 1990. ISSN 0020-1693. doi: https://doi.org/10.1016/S0020-1693(00)84855-0. URL http://www.sciencedirect.com/science/article/pii/S0020169300848550.

[260] Mazhar N. Ali, Jun Xiong, Steven Flynn, Jing Tao, Quinn D. Gibson, Leslie M. Schoop, Tian Liang, Neel Haldolaarachchige, Max Hirschberger, N. P. Ong, and R. J. Cava. Large, non-saturating magnetoresistance in WTe_2. *Nature*, 514(7521):205–208, 2014. ISSN 1476-4687. doi: 10.1038/nature13763. URL https://doi.org/10.1038/nature13763.

[261] Alexey A. Soluyanov, Dominik Gresch, Zhijun Wang, QuanSheng Wu, Matthias Troyer, Xi Dai, and B. Andrei Bernevig. Type-II Weyl semimetals. *Nature*, 527 (7579):495–498, 2015. ISSN 1476-4687. doi: 10.1038/nature15768. URL https://doi.org/10.1038/nature15768.

[262] Kaifei Kang, Tingxin Li, Egon Sohn, Jie Shan, and Kin Fai Mak. Nonlinear anomalous

hall effect in few-layer WTe_2. *Nature Materials*, 18(4):324–328, . ISSN 1476-4660. doi: 10.1038/s41563-019-0294-7. URL https://doi.org/10.1038/s41563-019-0294-7.

[263] Qiong Ma, Su-Yang Xu, Huitao Shen, David MacNeill, Valla Fatemi, Tay-Rong Chang, Andrés M. Mier Valdivia, Sanfeng Wu, Zongzheng Du, Chuang-Han Hsu, Shiang Fang, Quinn D. Gibson, Kenji Watanabe, Takashi Taniguchi, Robert J. Cava, Efthimios Kaxiras, Hai-Zhou Lu, Hsin Lin, Liang Fu, Nuh Gedik, and Pablo Jarillo-Herrero. Observation of the nonlinear hall effect under time-reversal-symmetric conditions. *Nature*, 565(7739):337–342. ISSN 1476-4687. doi: 10.1038/s41586-018-0807-6. URL https://doi.org/10.1038/s41586-018-0807-6.

[264] Seunguk Song, Se-Yang Kim, Jinsung Kwak, Yongsu Jo, Jung Hwa Kim, Jong Hwa Lee, Jae-Ung Lee, Jong Uk Kim, Hyung Duk Yun, Yeoseon Sim, Jaewon Wang, Do Hee Lee, Shi-Hyun Seok, Tae-il Kim, Hyeonsik Cheong, Zonghoon Lee, and Soon-Yong Kwon. Electrically robust single-crystalline WTe_2 nanobelts for nanoscale electrical interconnects. *Advanced Science*, 6(3):1801370, 2019. ISSN 2198-3844. doi: https://doi.org/10.1002/advs.201801370. URL https://doi.org/10.1002/advs.201801370.

[265] Zaiyao Fei, Wenjin Zhao, Tauno A. Palomaki, Bosong Sun, Moira K. Miller, Zhiying Zhao, Jiaqiang Yan, Xiaodong Xu, and David H. Cobden. Ferroelectric switching of a two-dimensional metal. *Nature*, 560(7718):336–339. ISSN 1476-4687. doi: 10.1038/s41586-018-0336-3. URL https://doi.org/10.1038/s41586-018-0336-3.

[266] Pankaj Sharma, Fei-Xiang Xiang, Ding-Fu Shao, Dawei Zhang, Evgeny Y. Tsymbal, Alex R. Hamilton, and Jan Seidel. A room-temperature ferroelectric semimetal. *Science Advances*, 5(7), 2019. doi: 10.1126/sciadv.aax5080. URL https://advances.sciencemag.org/content/5/7/eaax5080.

[267] Defen Kang, Yazhou Zhou, Wei Yi, Chongli Yang, Jing Guo, Youguo Shi, Shan Zhang, Zhe Wang, Chao Zhang, Sheng Jiang, Aiguo Li, Ke Yang, Qi Wu, Guangming Zhang, Liling Sun, and Zhongxian Zhao. Superconductivity emerging from a suppressed large magnetoresistant state in tungsten ditelluride. *Nature Communications*, 6(1):7804,

. ISSN 2041-1723. doi: 10.1038/ncomms8804. URL https://doi.org/10.1038/ncomms8804.

[268] Yu Tao, John A. Schneeloch, Adam A. Aczel, and Despina Louca. T_d to $1T'$ structural phase transition in the wte_2 weyl semimetal. *Phys. Rev. B*, 102:060103, Aug 2020. doi: 10.1103/PhysRevB.102.060103. URL https://link.aps.org/doi/10.1103/PhysRevB.102.060103.

[269] R. Dahal, L. Z. Deng, N. Poudel, M. Gooch, Z. Wu, H. C. Wu, H. D. Yang, C. K. Chang, and C. W. Chu. Tunable structural phase transition and superconductivity in the weyl semimetal $mo_{1-x}w_xte_2$. *Phys. Rev. B*, 101:140505, Apr 2020. doi: 10.1103/PhysRevB.101.140505. URL https://link.aps.org/doi/10.1103/PhysRevB.101.140505.

[270] Masimukku Srinivaas, Cheng-Yu Wu, Jenq-Gong Duh, Yu-Chen Hu, and Jyh Ming Wu. Multi-walled carbon-nanotube-decorated tungsten ditelluride nanostars as anode material for lithium-ion batteries. *Nanotechnology*, 31(3):035406, 2019. ISSN 0957-4484 1361-6528. doi: 10.1088/1361-6528/ab48b2. URL http://dx.doi.org/10.1088/1361-6528/ab48b2.

[271] Mengji Chen, Kyusup Lee, Jie Li, Liang Cheng, Qisheng Wang, Kaiming Cai, Elbert E. M. Chia, Haixin Chang, and Hyunsoo Yang. Anisotropic picosecond spin-photocurrent from weyl semimetal WTe_2. *ACS Nano*, 14(3):3539–3545, 2020. ISSN 1936-0851. doi: 10.1021/acsnano.9b09828. URL https://doi.org/10.1021/acsnano.9b09828.

[272] Tuan Anh Pham, Kyoung E. Kweon, Amit Samanta, Vincenzo Lordi, and John E. Pask. Solvation and dynamics of sodium and potassium in ethylene carbonate from ab initio molecular dynamics simulations. *The Journal of Physical Chemistry C*, 121 (40):21913–21920, 2017. ISSN 1932-7447. doi: 10.1021/acs.jpcc.7b06457. URL https://doi.org/10.1021/acs.jpcc.7b06457.

[273] R. Shannon. Revised effective ionic radii and systematic studies of interatomic dis-

tances in halides and chalcogenides. *Acta Crystallographica Section A*, 32(5):751–767, 1976. ISSN 0567-7394. doi: doi:10.1107/S0567739476001551. URL https://doi.org/10.1107/S0567739476001551.

[274] Masaki Okoshi, Yuki Yamada, Shinichi Komaba, Atsuo Yamada, and Hiromi Nakai. Theoretical analysis of interactions between potassium ions and organic electrolyte solvents: A comparison with lithium, sodium, and magnesium ions. *Journal of The Electrochemical Society*, 164(2):A54–A60, dec 2016. doi: 10.1149/2.0211702jes. URL https://doi.org/10.1149/2.0211702jes.

[275] Yoshiharu Matsuda, Hitoshi Nakashima, Masayuki Morita, and Yoshio Takasu. Behavior of some ions in mixed organic electrolytes of high energy density batteries. *Journal of The Electrochemical Society*, 128(12):2552–2556, dec 1981. doi: 10.1149/1.2127289. URL https://doi.org/10.1149/1.2127289.

[276] De Li and Haoshen Zhou. Two-phase transition of li-intercalation compounds in Li-ion batteries. *Materials Today*, 17(9):451–463, 2014. ISSN 1369-7021. doi: https://doi.org/10.1016/j.mattod.2014.06.002. URL https://www.sciencedirect.com/science/article/pii/S1369702114002156.

[277] Matsuhiko Nishizawa, Hiromichi Koshika, Ryuichi Hashitani, Takashi Itoh, Takayuki Abe, and Isamu Uchida. Ion- and electron-transport properties of a single particle of disordered carbon during the lithium insertion reaction. *The Journal of Physical Chemistry B*, 103(24):4933–4936, 1999. doi: 10.1021/jp990604t. URL https://doi.org/10.1021/jp990604t.

[278] Shitong Wang, Yanhao Dong, Fangjun Cao, Yutong Li, Zhongtai Zhang, and Zilong Tang. Conversion-type MnO nanorods as a surprisingly stable anode framework for sodium-ion batteries. *Advanced Functional Materials*, 30(19):2001026, 2020. doi: https://doi.org/10.1002/adfm.202001026. URL https://onlinelibrary.wiley.com/doi/abs/10.1002/adfm.202001026.

[279] Chunsheng Wang, Imran Kakwan, A.John Appleby, and Frank E Little. In situ investigation of electrochemical lithium intercalation into graphite powder. *Journal of Electroanalytical Chemistry*, 489(1):55–67, 2000. ISSN 1572-6657. doi: https://doi.org/10.1016/S0022-0728(00)00197-2. URL https://www.sciencedirect.com/science/article/pii/S0022072800001972.

[280] Chunsheng Wang, A.John Appleby, and Frank E Little. Charge–discharge stability of graphite anodes for lithium-ion batteries. *Journal of Electroanalytical Chemistry*, 497(1):33–46, 2001. ISSN 1572-6657. doi: https://doi.org/10.1016/S0022-0728(00)00447-2. URL https://www.sciencedirect.com/science/article/pii/S0022072800004472.

[281] Yang Xu, Chenglin Zhang, Min Zhou, Qun Fu, Chengxi Zhao, Minghong Wu, and Yong Lei. Highly nitrogen doped carbon nanofibers with superior rate capability and cyclability for potassium ion batteries. *Nature Communications*, 9(1):1720, 2018. ISSN 2041-1723. doi: 10.1038/s41467-018-04190-z. URL https://doi.org/10.1038/s41467-018-04190-z.

[282] Sanghyeon Kim, Jaewon Choi, Seong-Min Bak, Lingzi Sang, Qun Li, Arghya Patra, and Paul V. Braun. Reversible conversion reactions and small first cycle irreversible capacity loss in metal sulfide-based electrodes enabled by solid electrolytes. *Advanced Functional Materials*, 29(27):1901719, 2019. ISSN 1616-301X. doi: https://doi.org/10.1002/adfm.201901719. URL https://doi.org/10.1002/adfm.201901719.